Article

Neuron

The Epigenetic State of PRDM16-Regulated Enhancers in Radial Glia Controls Cortical Neuron Position

Graphical Abstract

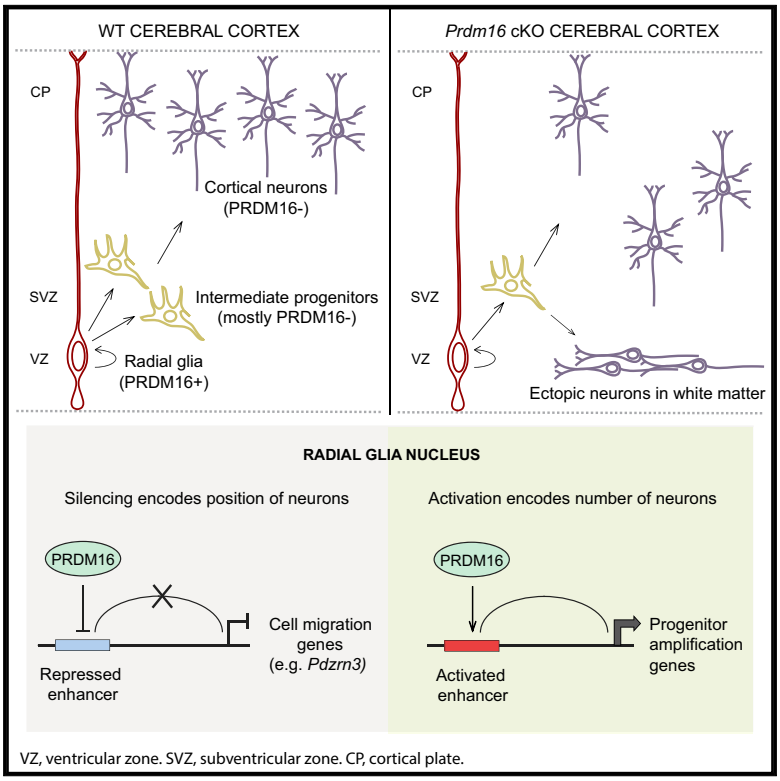

VZ, ventricular zone. SVZ, subventricular zone. CP, cortical plate.

Authors

José-Manuel Baizabal, Meeta Mistry, Miguel Turrero García, ..., Matthew B. Johnson, Christopher A. Walsh, Corey C. Harwell

Correspondence

manuelbaizabal2018@gmail.com (J.-M.B.), corey_harwell@hms.harvard.edu (C.C.H.)

In Brief

Baizabal et al. uncover an epigenetic mechanism that encodes the number and position of upper layer cortical neurons in the activity of transcriptional enhancers in neural stem cells.

Highlights

- PRDM16 activity in radial glia encodes the number and position of cortical neurons
- Enhancer regulation by PRDM16 represses neuronal migration genes in radial glia
- PRDM16 controls neuron position by silencing the ubiquitin E3 ligase PDZRN3
- The PR domain of PRDM16 promotes neuronal migration through gene silencing

Baizabal et al., 2018, Neuron *98*, 945–962
June 6, 2018
https://doi.org/10.1016/j.neuron.2018.04.033

CellPress

Neuron
Article

The Epigenetic State of PRDM16-Regulated Enhancers in Radial Glia Controls Cortical Neuron Position

José-Manuel Baizabal,[1,*] Meeta Mistry,[2] Miguel Turrero García,[1] Nicolás Gómez,[1] Olubusola Olukoya,[1] Diana Tran,[1] Matthew B. Johnson,[3] Christopher A. Walsh,[3] and Corey C. Harwell[1,4,*]
[1]Department of Neurobiology, Harvard Medical School, Boston, MA 02115, USA
[2]Bioinformatics Core, Department of Biostatistics, Harvard T.H. Chan School of Public Health, Harvard Medical School, Boston, MA 02115, USA
[3]Division of Genetics and Genomics, Manton Center for Orphan Disease and Howard Hughes Medical Institute, Boston Children's Hospital, Boston, MA 02115, USA
[4]Lead Contact
*Correspondence: manuelbaizabal2018@gmail.com (J.-M.B.), corey_harwell@hms.harvard.edu (C.C.H.)
https://doi.org/10.1016/j.neuron.2018.04.033

SUMMARY

The epigenetic landscape is dynamically remodeled during neurogenesis. However, it is not understood how chromatin modifications in neural stem cells instruct the formation of complex structures in the brain. We report that the histone methyltransferase PRDM16 is required in radial glia to regulate lineage-autonomous and stage-specific gene expression programs that control number and position of upper layer cortical projection neurons. PRDM16 regulates the epigenetic state of transcriptional enhancers to activate genes involved in intermediate progenitor cell production and repress genes involved in cell migration. The histone methyltransferase domain of PRDM16 is necessary in radial glia to promote cortical neuron migration through transcriptional silencing. We show that repression of the gene encoding the E3 ubiquitin ligase PDZRN3 by PRDM16 determines the position of upper layer neurons. These findings provide insights into how epigenetic control of transcriptional enhancers in radial glial determines the organization of the mammalian cerebral cortex.

INTRODUCTION

The mammalian cerebral cortex is composed of a vast diversity of neuronal cell types, which form the complex circuits necessary for high-level cognition. The cerebral cortex is organized into six layers of excitatory projection neurons that originate during embryonic development from a relatively simple neuroepithelium. All cortical neurons derive from a population of highly specialized neural stem cells known as radial glia (RG). During early neurogenesis, RG self-renew and give rise to neurons destined for deep layers of the cortex. As neurogenesis proceeds, RG give rise to intermediate progenitor (IP) cells that will go through one or two rounds of cell division before producing pairs of neurons destined for upper layers of the cortex (Kwan et al., 2012; Noctor et al., 2004). Newly generated neurons reach their final position by migrating along the basal processes of RG, which span the thickness of the developing cortex (Noctor et al., 2004). Assembly of the complex circuitry of the cerebral cortex requires precisely timed transcriptional programs that define the position, connectivity, and function of specific neuronal subtypes.

Chromatin-modifying enzymes are transcriptional regulators that control gene expression through covalent modification of DNA or histones. Modifications of chromatin structure by histone methylation and acetylation are thought to play a key role in regulating the cell type and stage-specific context in which transcriptional complexes can act by modifying the availability of *cis*-regulatory elements (Nashun et al., 2015; Tuoc et al., 2013). Genome-wide epigenetic profiling experiments have shown that, as cells progress toward their ultimate fates, they acquire a more restrictive chromatin state that promotes cell-specific transcriptional programs (Zhu et al., 2013). However, it is not understood how chromatin-modifying enzymes function in RG to establish the epigenetic landscape that determines cell type and stage-specific gene expression. The importance of chromatin remodeling for brain development is underscored by recent studies showing a critical role of chromatin-modifying factors in neurodevelopmental disorders (Mastrototaro et al., 2017).

The transcriptional regulator PRDM16 is a chromatin-modifying enzyme that belongs to the larger PRDM (Positive Regulatory Domain) protein family, that is structurally defined by the presence of a conserved N-terminal histone methyltransferase PR domain (Hohenauer and Moore, 2012). PRDM16 has been shown to function *in vitro* as a histone 3 lysine 9 (H3K9) and histone 3 lysine 4 (H3K4) mono-methyltransferase (Pinheiro et al., 2012; Zhou et al., 2016). PRDM16 also regulates gene expression by forming complexes with transcriptional co-factors and other histone-modifying proteins (Chi and Cohen, 2016). PRDM16 was previously shown to control embryonic and post-natal neural stem cell maintenance and differentiation in the brain (Chuikov et al., 2010; Inoue et al., 2017; Shimada et al., 2017). How PRDM16 functions to regulate transcriptional programs in the developing cerebral cortex remains largely unknown.

Here we show that PRDM16 regulates the sequential activation of stage-specific gene expression programs to establish

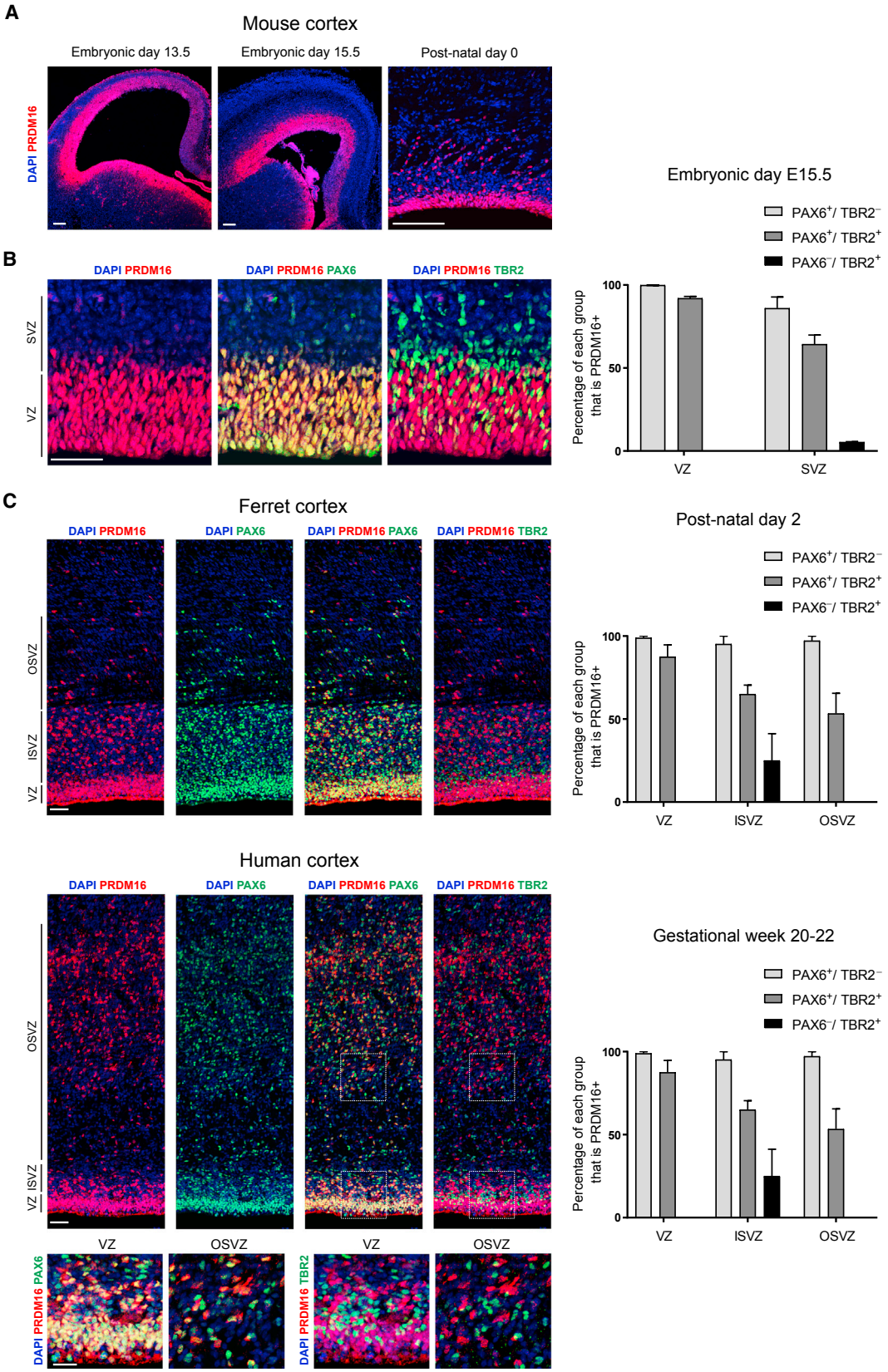

(legend on next page)

the organization of the cortex. This function is executed by (1) transcriptional activation of genes that control the production of IP cells and the number of upper layer neurons, and (2) transcriptional repression of genes that control migration of upper layer neurons. PRDM16 controls gene expression primarily by regulating the activity of transcriptional enhancers. The histone methyltransferase domain of PRDM16 participates in transcriptional repression in RG and influences gene expression during early stages of neuronal differentiation. Together, our findings suggest that PRDM16 regulates the epigenetic state of transcriptional enhancers in RG to instruct neurogenesis and migration of late-born cortical neurons.

RESULTS

Expression of *Prdm16* in RG Is Conserved in Different Mammalian Species

Prdm16 is expressed in the dorsal telencephalon throughout the neurogenic period (Figure S1A). At middle and late stages of cortical neurogenesis (embryonic day [E]13.5 and E15.5) and early post-natal development, *Prdm16* was predominantly expressed in the cortical ventricular zone (VZ), overlapping with the RG marker PAX6 (Figures 1A, 1B, and S1A) (Chuikov et al., 2010; Inoue et al., 2017). In the rodent, *Pax6* and *Tbr2* are transiently co-expressed in RG transitioning into IP cells (Arai et al., 2011; Englund et al., 2005). PAX6$^+$-TBR2$^+$ cells in the VZ and subventricular zone (SVZ) expressed *Prdm16* (Figure 1B). In contrast, PRDM16 was almost completely absent from PAX6$^-$-TBR2$^+$ IP cells in the SVZ (Figure 1B). We did not detect PRDM16 in mature post-mitotic neurons in the cortical plate (Figure 1SB), though it was detected in cortical astrocytes (Figure S1C). Hence, *Prdm16* is selectively expressed in mouse RG and silenced upon differentiation into IP cells.

Previous studies have suggested that *Prdm16* is part of a core set of genes specifically expressed in mouse and human RG (Lui et al., 2014). Unlike the lissencephalic mouse cortex, gyrencephalic species display an expanded outer SVZ (OSVZ) that contains a basal population of outer RG (Lui et al., 2011). To determine if *PRDM16* is expressed in both VZ and OSVZ, we examined ferret cortex at post-natal day (P)2 and human cortex at gestational weeks 20–22 (Figure 1C). *PRDM16* is expressed in PAX6$^+$ RG in the VZ, inner SVZ, and OSVZ, while most PAX6$^-$-TBR2$^+$ IP cells within the ferret and human SVZ did not express *PRDM16* (Figure 1C). Thus, specific *PRDM16* expression in RG is conserved in gyrencephalic species.

PRDM16 Activity in RG Controls Cortical Neuron Position

To determine the function of PRDM16 during cerebral cortex development, we crossed a mouse line carrying a conditional allele of *Prdm16* (*Prdm16*$^{flox/flox}$) with *Emx1*$^{Ires\text{-}Cre}$ mice (animals carrying both mutant alleles are referred to as *Prdm16* conditional knockout [cKO]) (Cohen et al., 2014; Gorski et al., 2002). *Prdm16* cKO mice displayed a specific loss of PRDM16 in the developing cerebral cortex, but not in the ganglionic eminences or the choroid plexus (Figure S2A). In contrast to *Prdm16*-null KO mice, *Prdm16* cKO mice survived into adulthood and the size of the early post-natal brains was not affected (Figure S2B) (Chuikov et al., 2010).

We analyzed the laminar organization of P15 wild-type (WT) and cKO cortex by labeling neurons in upper layers (i.e., layers II–IV) with CUX1 and deep layers (i.e., layers V and VI) with CTIP2. There was a significant decrease in the thickness of cortical upper layers and a slight expansion of deep layers in cKO brains, whereas the overall thickness of the cortex did not change significantly in comparison to controls (Figure 2A). Quantification of CUX1$^+$ cells through entire cortical hemisphere sections confirmed a decrease in layer II–IV projection neurons in cKO brains (Figure 2A). In contrast, the number of CTIP2$^+$ or SATB2$^+$ neurons was not significantly different between WT and cKO cortices (Figures 2A and S2C).

Numerous ectopic CUX1$^+$ neurons were scattered across deep layers of the cKO cortex, as well as within distinctive neuronal heterotopias in layer VI and the white matter (WM) (Figures 2A, 2B, and S2D). RORβ$^+$ layer IV neurons were located close to the pial surface of the cKO cortex at P15, while whisker barrels in layer IV of the somatosensory cortex were small, disorganized, and superficial in cKO brains, compared to controls (Figure S2C). Hence, *Prdm16* cKO brains show cortical lamination defects. Quantification of S100β$^+$ cells in WT and cKO cortices at P15 showed no difference, suggesting that PRDM16 does not affect astrocyte numbers (Figure S2E).

The lamination defects in *Prdm16* cKO cortex indicate that late-born upper layer neuron migration is impaired in mutant brains. To test this possibility, we electroporated control and cKO cortices at E15.5 with a plasmid encoding membrane *tdTomato* and nuclear GFP in order to label cortical RG and their progeny, which were analyzed at P10. Control RG generated upper layer neurons that migrated into layers II and III, projecting axons that branched extensively in layer V before entering the WM (Figure 2C). In contrast, mutant RG generated a large number of cortical neurons that did not reach the upper layers and either remained ectopic in deep cortical layers or formed heterotopias in the WM, resulting in disruption of the laminar organization of the cortex (Figure 2C).

Migration defects in cortical neurons could result from an inability of mutant RG to provide the structural scaffold that guides migration. However, there were no gross structural defects in the basal processes of mutant RG at E16.5 (Figure S3A), a stage when layer II–IV neurons are actively

Figure 1. *Prdm16* Expression in Radial Glia Is Conserved in Mammals

(A) Immunostaining of PRDM16 in coronal sections of the developing mouse brain.

(B) PRDM16 overlaps with PAX6$^+$-TBR2$^-$ and PAX6$^+$-TBR2$^+$ cells in the ventricular zone (VZ) and subventricular zone (SVZ) of mouse cortex and does not overlap with most PAX6$^-$-TBR2$^+$ cells in the SVZ.

(C) PRDM16 is detected in PAX6$^+$-TBR2$^-$ and PAX6$^+$-TBR2$^+$ cells in the VZ, inner SVZ (ISVZ), and outer SVZ (OSVZ) in ferret and human cortex. PRDM16 is present in a minority of PAX6$^-$-TBR2$^+$ cells.

Data represent mean ± SE for mouse (n = 3), ferret (n = 2), and human (n = 2). Scale bars, 100 μm (A) and 50 μm (B and C). See also Figure S1.

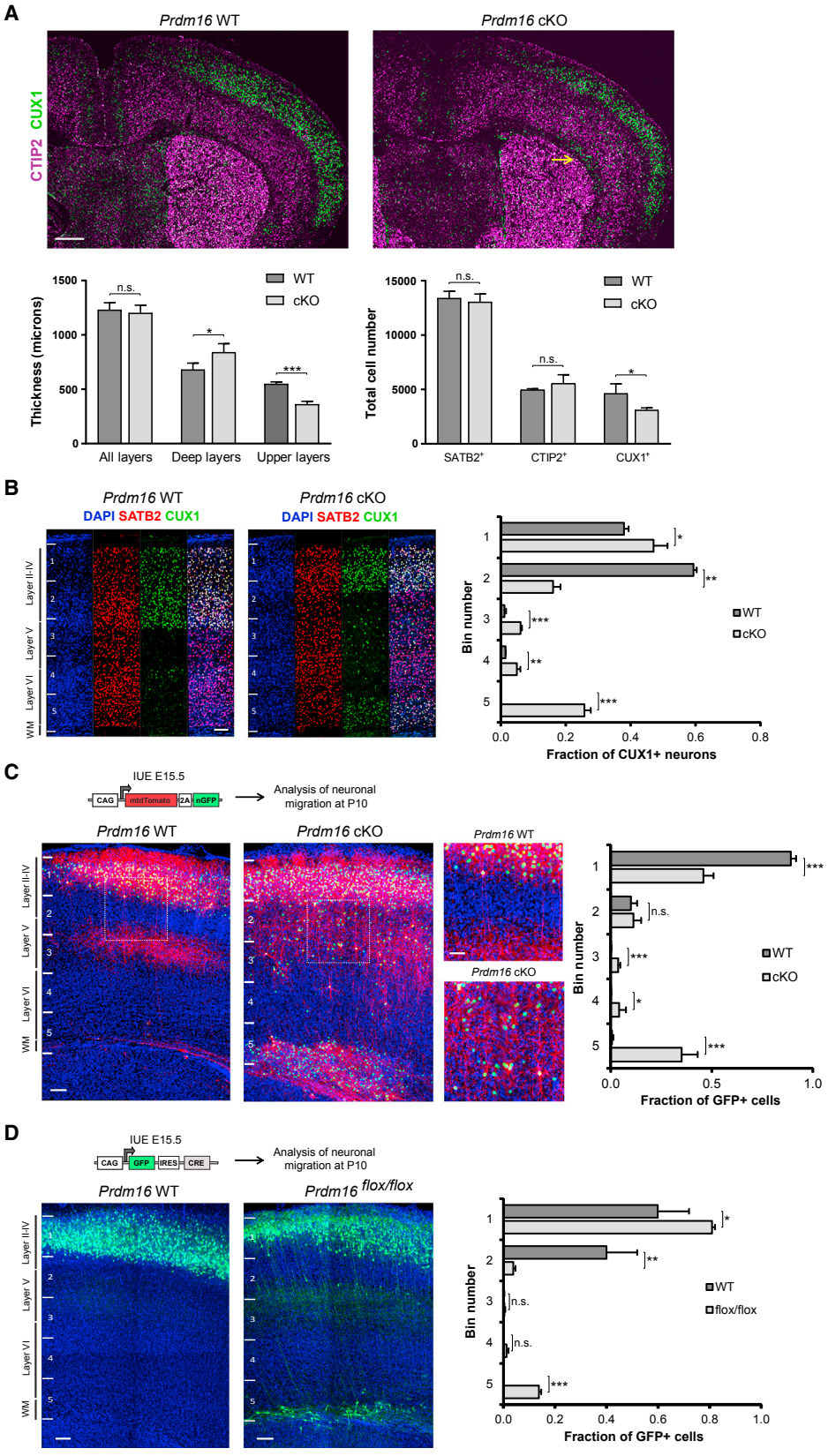

(legend on next page)

migrating to the cortical plate (Kwan et al., 2012). We next mutated *Prdm16* in a subset of cortical RG by electroporating a plasmid encoding Cre and GFP into the ventricles of E15.5 *Prdm16*$^{flox/flox}$ embryos, and we analyzed them at P10. A group of electroporated neurons derived from mutant RG did not migrate into upper layers, remaining ectopic in the WM (Figure 2D). In addition, knockdown (KD) of *Prdm16* by electroporating a short hairpin RNA (shRNA) into WT brains at E14.5 resulted in ectopic GFP$^+$-CUX1$^+$ neurons in deep cortical layers and heterotopias in the WM at P5 (Figures S3B and S3C) (Inoue et al., 2017). Together, our results suggest that PRDM16 activity in RG has a lineage-autonomous role in directing upper layer cortical neuron migration.

To rule out the possibility that low levels of *Prdm16* in newborn cortical neurons might influence migration, we mutated *Prdm16* specifically in newborn cortical neurons using the Nex^{Cre} mouse line, which is active as early as E11.5 (Figure S3D) (Goebbels et al., 2006). *In utero* electroporation of a plasmid expressing nuclear GFP into *Nex*^{Cre} *Prdm16*$^{flox/flox}$ cortex at E15.5 indicated that migration of upper layer neurons was not impaired (Figure S3E). Therefore, *Prdm16* expression in newborn cortical neurons is not necessary for their migration into upper layers.

The presence of ectopic upper layer neurons in *Prdm16* cKO cortex could cause disruptions in the organization of long-range axonal projections connecting different brain areas. To test this, we analyzed cortical neurons electroporated with a plasmid encoding membrane *tdTomato* and nuclear GFP (Figure S4A). In control brains, most callosal axons projected into a single contralateral column that mirrors the ipsilateral electroporation site (Figures S4B and S4C). In contrast, callosal axons in mutant brains were more broadly dispersed along the medial-lateral axis of the contralateral hemisphere (Figures S4B and S4C), and they displayed increased axonal projections into the ipsilateral motor area (Figures S4B and S4C). These observations suggest that *Prdm16* might play a role in determining the pattern of axonal projections in the cortex.

PRDM16 Activity in RG Controls Intermediate Progenitor Cell Production and Proliferation

The fact that *Prdm16* expression is restricted to RG, together with the effect of *Prdm16* loss of function on both the number and organization of upper layer neurons, led us to investigate the role of *Prdm16* in cortical neurogenesis. There was no difference in the total number of dividing cells or the number of PAX6$^+$ RG in the germinal zones (i.e., VZ plus SVZ) in WT and cKO cortex at E15.5 (Figure 3A, S5A, and S5B). In contrast, the number of mitotic and interphase TBR2$^+$ IP cells was decreased in the cKO cortex, suggesting defects in the production and amplification of IP cells (Figure 3A).

Reduced numbers of dividing IP cells in the mutant SVZ could result from changes in the number of progenitors re-entering the cell cycle. To test this hypothesis, we injected 5-ethynyl-2′-deoxyuridine (EdU) at E14.5 to label cycling progenitors, and 24 hr later we analyzed the fraction of EdU-labeled cells that co-stained with Ki67, a marker of cell proliferation. The fraction of cells exiting the cell cycle (i.e., EdU$^+$-Ki67$^-$ fraction of Edu$^+$ cells) was increased in the VZ of the cKO cortex (Figure 3B). An increase in cell cycle exit in the mutant VZ might reduce the number of progeny generated by individual RG. In the developing cerebral cortex, radial clones consist of a single RG and its progeny, which remain in close association to the basal process of the parent cell (Noctor et al., 2001). To label individual RG and their progeny, we injected a retrovirus expressing GFP into the ventricles of E14.5 WT and cKO embryos, and we analyzed the size of cortical radial clones at E16.5. To estimate the number of progeny generated by individual RG, we only took into account radial units, meaning that all one-cell clones consisted of a single RG. Quantification of the number of cells per radial clone indicated that WT RG generated a normal distribution of clonal sizes, with a high percentage of clones composed of three cells (Figure 3C). In contrast, mutant RG produced a larger proportion of clones composed of two cells (Figure 3C). Most IP cells in the SVZ and immature neurons at the intermediate zone (IZ) display a multipolar morphology (Kowalczyk et al., 2009; LoTurco and Bai, 2006). We found that the percentage of clones containing multipolar cells was reduced in cKO radial clones compared to WT clones, further supporting a decrease in IP cell and cortical neuron generation by mutant RG (Figure 3C) (Inoue et al., 2017). Together, our results indicate that PRDM16 decreases cell cycle exit in the VZ, thereby promoting the production of IP cells and upper layer cortical neurons.

Intrinsic Control of Neuronal Migration by PRDM16 Activity in RG

The migration defects observed in *Prdm16* cKO cortex could be the result of changes in the timing of neurogenesis or an intrinsic migration defect in the lineage of mutant RG. To discriminate between these possibilities, we assessed the timing of deep layer and upper layer neurogenesis in WT and cKO cortices. Since the majority of deep layer neurons are generated between E12 and E14 (Molyneaux et al., 2007), we injected EdU at E14.5 to label proliferating progenitors at the final stages of deep layer neurogenesis, and we analyzed the percentage of EdU$^+$-CTIP2$^+$ cells relative to EdU$^+$ cells at E17.5. The relative percentage of

Figure 2. PRDM16 Controls Number and Position of Upper Layer Neurons

(A) Coronal sections of *Prdm16* WT and cKO brains at P15. A CUX1$^+$ heterotopia is shown in the white matter of the cKO cortex (arrow). Left plot shows quantification of deep and upper layer thickness (n = 3). Right plot shows quantification of cortical neuron subtypes (n = 3).

(B) Laminar distribution of CUX1$^+$ neurons in *Prdm16* WT and cKO cortex at P15. Cortical columns were divided into 5 bins. The fraction of CUX1$^+$ neurons in each bin was quantified (n = 3).

(C) E15.5 *in utero* electroporation (IUE) of plasmid encoding membrane tdTomato and nuclear GFP followed by analysis of migration at P10. The fraction of GFP$^+$ nuclei in each bin was quantified (n = 4 WT and n = 7 cKO brains). Insets show lamination defects at higher magnification.

(D) E15.5 IUE of a plasmid encoding GFP and Cre followed by analysis of migration at P10. The fraction of GFP$^+$ cells in each bin was quantified (n = 3).

Data represent mean ± SD; statistical analysis is unpaired Student's t test (*p < 0.05, **p < 0.01, and ***p < 0.001; n.s., not significant). Scale bars, 500 μm (A) and 100 μm (B–D). See also Figures S2–S4.

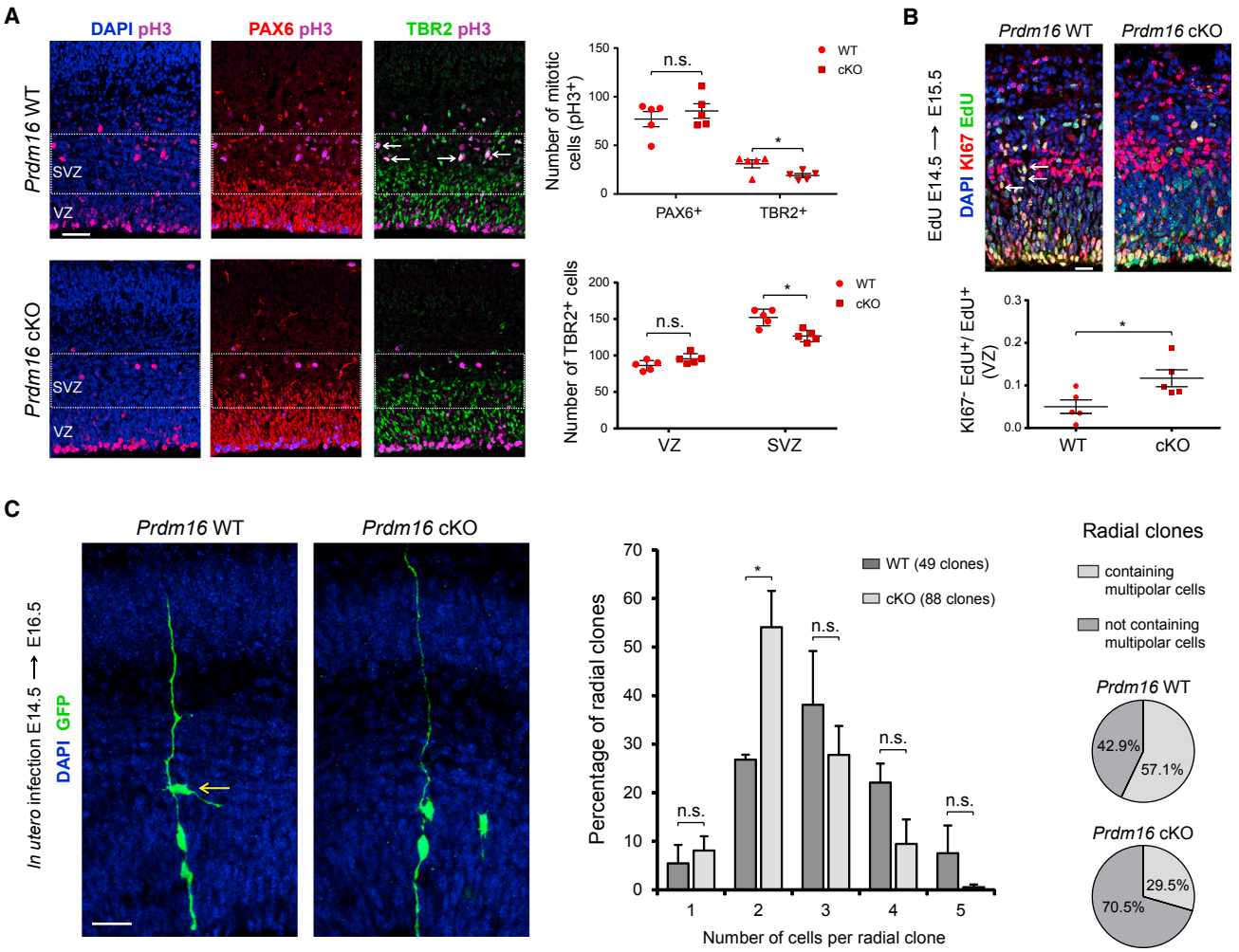

Figure 3. PRDM16 Controls Intermediate Progenitor Generation and Expansion

(A) E15.5 WT and *Prdm16* cKO cortical sections immunostained for PAX6, TBR2, and pH3. The ventricular zone (VZ) and subventricular zone (SVZ) are indicated. Arrows show examples of TBR2$^+$-pH3$^+$ cells in the SVZ of WT cortex. Top plot shows quantification of PAX6$^+$-pH3$^+$ and TBR2$^+$-pH3$^+$ cells (n = 5). Lower plot indicates the number of TBR2$^+$ cells (n = 5).

(B) Cell cycle exit analysis. Arrows indicate examples of KI67$^+$-EdU$^+$ cells. The fraction of KI67$^-$-EdU$^+$ cells relative to EdU$^+$ cells was quantified (n = 5).

(C) Clonal analysis of radial glia. The number of cells per clone was analyzed in 3 WT and 5 cKO brains. Pie charts indicate the percentage of clones containing cells with multipolar morphology (arrow).

Data represent mean ± SE; statistical analysis is unpaired Student's t test (*p < 0.05, **p < 0.01, and ***p < 0.001; n.s., not significant). Scale bars, 50 μm (A) and 20 μm (B and C). See also Figure S5.

EdU$^+$-CTIP2$^+$ cells generated after E14.5 did not change significantly between WT and cKO cortex, indicating that the birthdate of deep layer neurons is not affected in cKO mice (Figure S5C).

We next analyzed if ectopic neurons in the cKO cortex were generated during the normal phase of upper layer neurogenesis between E14 and E17 (Molyneaux et al., 2007). We injected EdU at E17.5 and P0, and we analyzed the distribution of EdU$^+$-CUX1$^+$ cells at P2 (Figure S5D). Most ectopic CUX1$^+$ cells in P2 cKO brains are located in the WM adjacent to the ventricle (Figure S5D). The majority of these ectopic CUX1$^+$ neurons in the WM had not incorporated EdU, suggesting that they were generated before E17.5 and likely produced during the normal period of upper layer neurogenesis (Figure S5D). These observations suggest that a change in the birthdate of upper layer neurons is not the main cause of their impaired migration phenotype and, thus, support an intrinsic migration defect in the progeny of mutant RG.

PRDM16 Regulates Stage-Specific Gene Expression Programs for Progenitor Amplification and Neuronal Migration

Our evidence indicates that PRDM16 regulates the production and migration of late-born projection neurons, possibly by controlling gene expression programs that are critical for these processes. To analyze changes of gene expression during neurogenesis, we used antibody labeling of intracellular markers in single-cell suspensions, followed by cell sorting and transcriptional

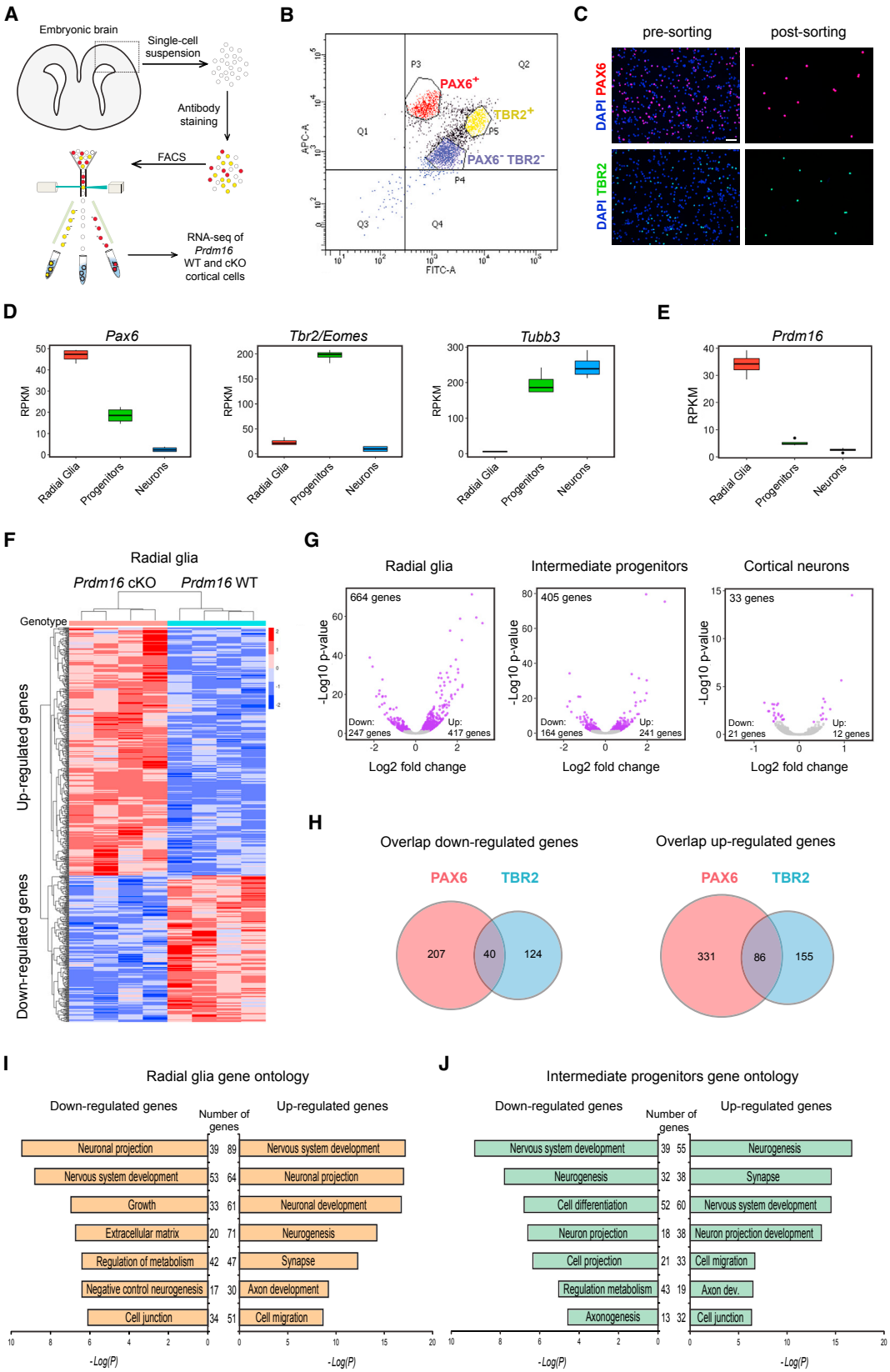

(legend on next page)

profiling using RNA sequencing (RNA-seq) (Figure 4A) (Hrvatin et al., 2014). Sorting gates were adjusted to purify PAX6$^+$ cortical RG and TBR2$^+$ IP cells, whereas sorting of prospective postmitotic neurons was based on the absence of PAX6 and TBR2 (Figure 4B). In comparison to unsorted cell suspensions, sorted cell suspensions showed a high enrichment (i.e., >99%) of the desired cell types (Figure 4C). Quantification of gene expression levels in sorted WT cells confirmed high *Pax6* expression in RG and high *Tbr2* expression in IP cells (Figure 4D). Consistent with previous reports, we found medium-to-high levels of *NeuroD1*, *Dcx*, and *Tubb3* expression in sorted IP cells, indicating that a subset of TBR2$^+$ cells is immature neurons (Figures 4D and S6A) (Arai et al., 2011; Englund et al., 2005). In contrast, PAX6$^-$-TBR2$^-$ sorted cells showed low levels of *NeuroD1* and high levels of *Dcx*, *Tubb3*, and *Map2*, indicating a mixture of immature and mature cortical neurons (Figures 4D and S6A). We confirmed high *Prdm16* expression in sorted PAX6$^+$ cells and low *Prdm16* expression in TBR2$^+$ IP cells and PAX6$^-$-TBR2$^-$ neurons (Figure 4E). Together, these observations demonstrate the isolation of cell types for subsequent transcriptional profiling during cortical neurogenesis.

We next determined the gene expression differences between E15.5 WT and cKO sorted cells. Real-time PCR amplification of *Prdm16* (exon 9) confirmed very low expression in sorted cKO cells (Figure S6B). We sequenced RNA libraries from four biological replicates per genotype, and we evaluated the data by hierarchical clustering and principal-component analysis, which demonstrated that major differences between samples are driven by genotype and not by batch effects (Figure S6C). Differential gene expression analysis revealed consistent changes between WT and cKO RG across all four replicates (Figure 4F). A group of 22 differentially expressed genes was confirmed by real-time PCR analysis (Figure S6D; Tables S1–S4). RNA-seq of the isolated cell types indicated that most gene expression changes occurred in cKO RG and IP cells (Figure 4G). We found 417 upregulated genes and 247 downregulated genes in cKO RG using an adjusted p value < 0.05 (Figure 4G; Table S5). There were 241 upregulated and 164 downregulated genes in sorted cKO IP cells, while in mature cortical neurons only a handful of genes displayed gene expression changes (Figure 4G; Table S5). In general, upregulated genes in all cell types presented larger fold changes in gene expression than downregulated genes (Figure 4G). Most differentially expressed genes in RG and IP cells did not overlap (Figure 4H), indicating that *Prdm16* regulates stage-specific transcriptional programs.

Functional classification of differentially expressed genes in RG and IP cells by gene ontology revealed that upregulated genes in cKO RG have reported roles in neuronal differentiation (i.e., neurogenesis), neuronal maturation (i.e., synapse and axon development), and cell migration (Figure 4I; Table S5). In contrast, downregulated genes in cKO RG are involved in processes related to stem cell self-renewal and progenitor expansion (i.e., growth and negative regulation of neurogenesis) as well as maintenance of the progenitor niche (i.e., extracellular matrix and cell junction) (Figure 4I). Functional classification of differentially expressed genes in IP cells indicated the upregulation of genes involved in cell migration, whereas genes promoting neurogenesis, neuronal projection, and axon development were enriched in both upregulated and downregulated groups (Figure 4J). Thus, PRDM16 regulates developmental programs that control early stages of RG progeny amplification, differentiation, and migration.

Distal Regulation by PRDM16 Sets the Gene Expression Programs for Expansion and Migration of RG Progeny

The absence of *Prdm16* in cortical RG results in the misregulation of over a thousand genes during neurogenesis. To identify the subset of genes that are transcriptional targets of PRDM16 and to understand how these genes are directly regulated, we performed chromatin immunoprecipitation followed by sequencing (ChIP-seq) at E15.5, when upper layer neurons are being generated. In two independent biological replicates, we detected 13,864 and 26,666 ChIP-seq peaks that represent putative PRDM16-binding sites. To identify the most reproducible binding regions, we used irreproducible discovery rate (IDR) analysis using an IDR < 0.05, which resulted in 3,151 highly reproducible PRDM16-binding sites across the entire genome (Figure 5A; Table S6).

To validate the specificity of these binding sites, we performed PRDM16 ChIP-seq in two separate pools of E15.5 *Prdm16* cKO cortices. The majority of PRDM16-binding sites in WT cortex showed a significantly higher read density than equivalent genomic regions in cKO cortex (Figure S7A). Visualization of PRDM16 ChIP-seq peaks within genomic tracks demonstrated the absence of binding sites in cKO samples (Figure S7A). In the embryonic cortex, most PRDM16-binding sites were located either at intergenic regions (1,596 peaks) or introns (1,363 peaks), while few binding sites mapped to transcription start sites (TSSs) and proximal promoter regions (115 peaks) (Figure 5B). Analysis of DNA sequence motifs within high-confidence

Figure 4. Transcriptional Profiling of WT and *Prdm16* cKO Cells at Three Stages of Neurogenesis

(A) Experimental design for transcriptional profiling of E15.5 cortical cells.
(B) Representative plot showing sorting gates for PAX6$^+$ and TBR2$^+$ cells. Double-negative cells (PAX6$^-$-TBR2$^-$) are cortical neurons.
(C) Representative images of cell suspensions stained for DAPI, PAX6, and TBR2. Scale bar, 50 μm.
(D) Expression of *Pax6*, *Tbr2*, and *Tubb3* in sorted cells from E15.5 WT cortex.
(E) Expression of *Prdm16* in sorted cells from E15.5 WT cortex.
(F) Heatmap representing changes of gene expression in *Prdm16* cKO radial glia ($p < 0.05$).
(G) Volcano plots showing fold changes of gene expression in cKO cells. Each plot indicates upregulated and downregulated genes (purple circles).
(H) Venn diagrams showing the overlap of downregulated or upregulated genes between mutant PAX6$^+$ and TBR2$^+$ cells. The number of genes is indicated.
(I) Gene ontology analysis of differentially expressed genes between WT and *Prdm16* cKO radial glia.
(J) Gene ontology analysis of differentially expressed genes between WT and *Prdm16* cKO intermediate progenitors.
All transcriptome analyses used 4 biological replicates per genotype. RPKM, reads per kilobase of transcript per million mapped reads. See also Figure S6.

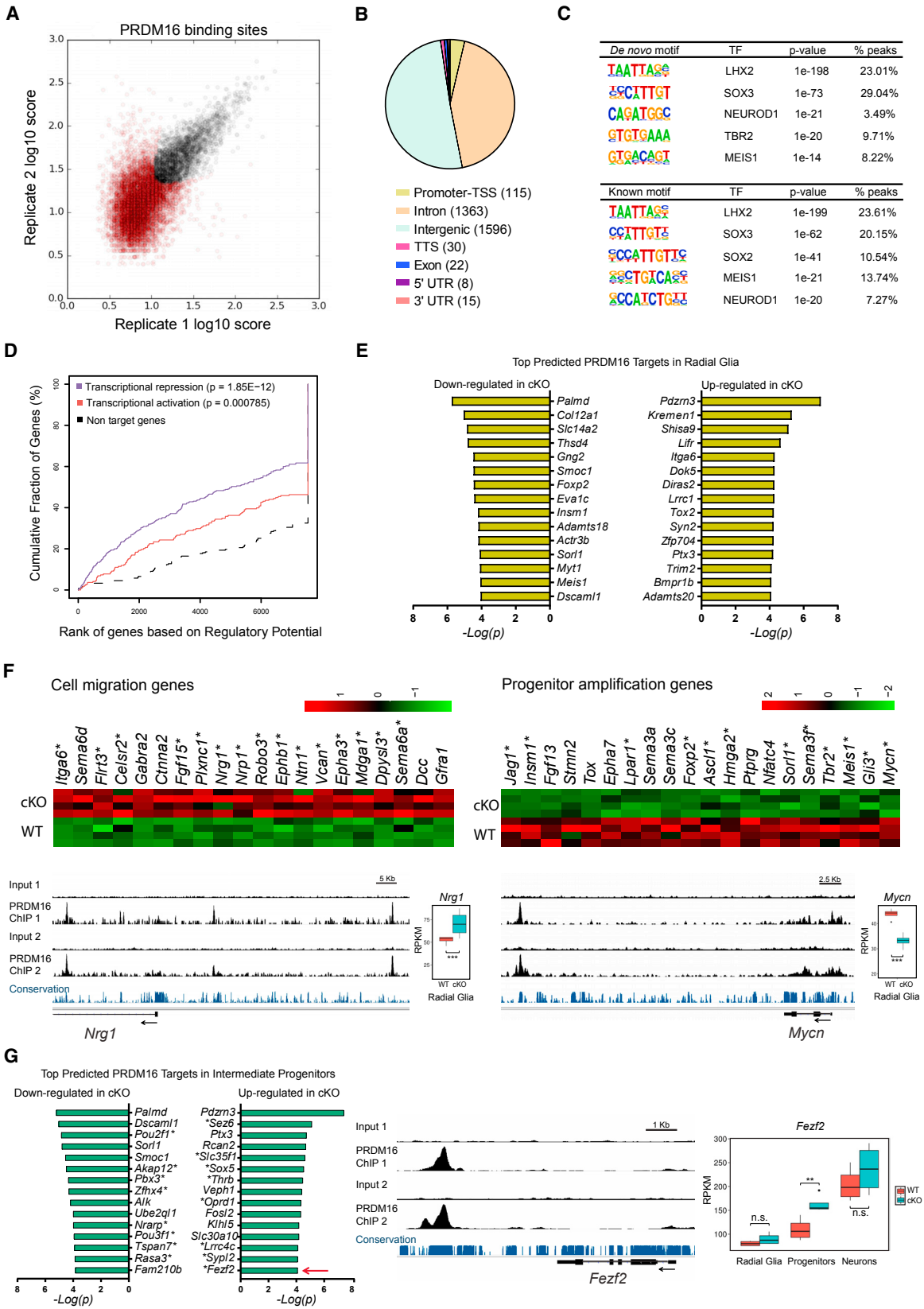

(legend on next page)

PRDM16-binding regions indicated high enrichment of binding motifs for transcriptional regulators known to play a key role in cortical neurogenesis, such as LHX2, SOX2/3, NEUROD1, TBR2, and MEIS1 (Figure 5C) (Guillemot and Hassan, 2017; Hsu et al., 2015; Sessa et al., 2008). Of note, our analysis did not recover a putative DNA-binding motif for PRDM16, which is consistent with previous evidence suggesting that PRDM16 is likely to function as a co-factor with other proteins that directly bind to DNA (Harms et al., 2015).

PRDM16 binding at genomic regions distal from most TSSs precludes an easy identification of direct transcriptional targets among differentially expressed genes between WT and cKO cells. To overcome this limitation, we applied a statistical method that integrates fold changes of gene expression between WT and cKO cells with the number and proximity of PRDM16-binding sites to the TSSs of differentially expressed genes (Wang et al., 2013). This method predicts whether a transcription factor functions as an activator or repressor, and it determines the probability of direct transcriptional regulation on individual genes (Wang et al., 2013). This analysis predicted a robust function of PRDM16 as a transcriptional repressor ($p = 1.85E{-}12$) and a moderate function as a transcriptional activator ($p = 7.85E{-}4$) (Figure 5D). Statistical prediction of individual transcriptional targets in RG defined 221 repressed genes associated with 379 PRDM16-binding regions and 106 activated genes associated with 174 PRDM16-binding regions using a false discovery rate (FDR) < 0.05 (Figure 5E; Table S7). Many cell migration genes are predicted to be directly repressed by PRDM16 activity in RG, while a number of progenitor amplification genes are predicted to be directly activated by PRDM16 in the same cells (Figure 5F). The list of transcriptional targets activated by PRDM16 includes genes that participate in IP cell generation and differentiation, such as *Insm1* and *Tbr2* (*Eomes*) (Figures 5F and S7B) (Arnold et al., 2008; Farkas et al., 2008; Sessa et al., 2008). Together, our results show that PRDM16 activity in RG provides a dichotomy of transcriptional repression and activation of functionally distinct groups of genes to coordinate the production and migration of late-born cortical neurons.

By combining the information on PRDM16-binding sites across the genome of cortical RG with the identification of 279 misregulated genes in mutant IP cells, we determined the subset of direct PRDM16 transcriptional targets for which gene expression is exclusively affected at the IP stage (Figure 5G; Table S7). This analysis indicates that PRDM16 promotes transcriptional activation or silencing of *cis*-regulatory regions during RG differentiation into IP cells (Figure 5G). Hence, PRDM16 activity in RG sets the gene expression program for subsequent stages of IP cell differentiation.

Enhancer Regulation by PRDM16 Controls Gene Expression in the Embryonic Cortex

To understand the transcriptional mechanisms by which PRDM16 controls gene expression during cortical development, we sought to determine the histone methylation pattern within PRDM16-binding regions using the Encyclopedia of DNA Elements (ENCODE) project datasets collected from E14.5 mouse brains (Stamatoyannopoulos et al., 2012). We analyzed the overlap of PRDM16-binding regions with H3K4 tri-methylation (H3K4me3), an epigenetic modification enriched in promoter regions, and histone 3 lysine 4 mono-methylation (H3K4me), a chromatin mark associated with poised and active enhancers (Heintzman et al., 2007). In addition, we analyzed the overlap of PRDM16 binding with histone 3 lysine 27 tri-methylation (H3K27me3), a polycomb modification linked to transcriptional repression during neurogenesis (Hirabayashi and Gotoh, 2010). We found moderate H3K4me3 and H3K4me levels in regions bound by PRDM16, whereas there was little overlap with H3K27me3 (Figure 6A).

The moderate enrichment of H3K4me within PRDM16-binding sites led us to assess the overlap with H3K27 acetylation (H3K27ac), another chromatin modification associated with active enhancer regions (Creyghton et al., 2010; Rada-Iglesias et al., 2011). PRDM16-binding regions overlapped extensively with embryonic H3K27ac (Figure 6B). Given that PRDM16 is mostly associated with distal genomic regions relative to promoters, the enrichment of H3K27ac indicates that PRDM16 primarily binds to active enhancers. PRDM16-binding sites showed much less H3K27ac enrichment in the adult cerebral cortex compared to embryonic stages (Figure 6B). We compared PRDM16 ChIP-seq peaks with embryonic and adult H3K27ac peaks in order to classify this subset of cortical enhancers as developmental (i.e., overlapping only with embryonic H3K27ac) or developmental and adult (i.e., overlapping with embryonic and adult H3K27ac), and we found that around two-thirds of PRDM16-bound genomic regions were active enhancers only during cortical development (Figure S7C).

The gene encoding for the ubiquitin E3 ligase PDZRN3 is the top predicted transcriptional target of PRDM16 in both RG and IP cells (Figures 5E and 5G). We selected a genomic region near the TSS of *Pdzrn3* to illustrate the pattern of histone modifications at PRDM16-binding sites. *Pdzrn3* belongs to a small group of 18

Figure 5. Distal Binding by PRDM16 Regulates Functionally Distinct Groups of Genes

(A) Identification of genome-wide PRDM16-binding sites in the E15.5 cortex by ChIP-seq. The plot represents the irreproducible discovery rate (IDR) analysis of two independent biological replicates. A total of 3,151 high-confidence PRDM16-binding sites was identified over an IDR < 0.05 (black circles).

(B) Distribution of PRDM16-binding sites across the genome. TSS, transcription start site; TTS, transcription termination site.

(C) *De novo* and known motif discovery within PRDM16-binding sites.

(D) Statistical integration of PRDM16-binding sites with differentially expressed genes in the cKO cortex predicts a dual function of PRDM16 as repressor (blue line) and activator (red line), using a set of non-differentially expressed genes as reference (black dashed line). The p value for each function is indicated.

(E) Top predicted PRDM16 transcriptional targets in radial glia.

(F) Heatmaps and ChIP-seq tracks indicate examples of cell migration genes repressed by PRDM16 and progenitor amplification genes activated by PRDM16. Asterisks indicate predicted direct transcriptional targets of PRDM16. *Nrg1* and *Mycn* are shown as examples for each group of genes.

(G) Top predicted PRDM16 transcriptional targets in intermediate progenitor cells. Asterisks indicate genes uniquely misregulated in intermediate progenitors, such as *Fezf2* (arrow), which is shown as an example of this group of genes.

Significant gene expression changes were identified using an FDR < 0.05 (*p < 0.05, **p < 0.01, and ***p < 0.001; n.s., not significant). See also Figure S7.

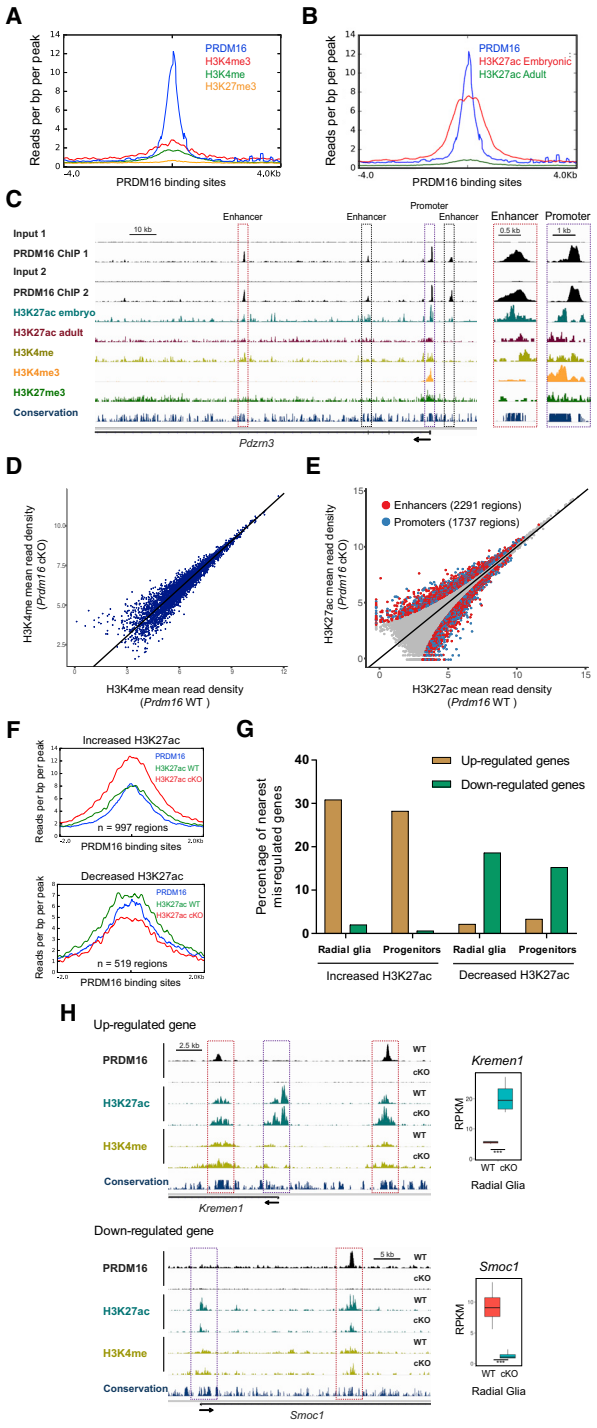

Figure 6. PRDM16 Regulates Transcriptional Enhancers in the Embryonic Cortex

(A) H3K4me3, H3K4me, and H3K27me3 profiles within a genomic window centered on PRDM16-binding sites in the embryonic cortex.

(B) H3K27ac embryonic and adult profiles within a genomic window centered on PRDM16-binding sites in the embryonic cortex.

(C) Profiles of histone modifications and PRDM16 binding near the transcription start site of *Pdzrn3*. Insets show closer views of the *Pdzrn3* promoter (purple box) and one enhancer (red box).

out of 327 predicted transcriptional targets that show PRDM16 binding at the promoter, which is identified by high levels of H3K4me3 (Figure 6C). Near the *Pdzm3* promoter, PRDM16 is bound at multiple enhancers, displaying high levels of H3K4me/H3K27ac and low H3K4me3 (Figure 6C). Hence, our analyses using the ENCODE datasets indicate that PRDM16 is primarily associated with active enhancers in the embryonic cortex.

Next, we performed ChIP-seq to determine genome-wide differences in H3K4me and H3K27ac between E15.5 WT and cKO cortices. We identified 76,807 H3K4me peaks (2 replicates per genotype) and 67,723 H3K27ac peaks (3 replicates per genotype) with high concordance across all samples (Figures 6D and 6E). The overall levels of H3K4me did not change significantly between different genotypes (Figure 6D). In contrast, 4,028 genomic regions exhibited differential H3K27ac enrichment between WT and cKO cortices (Figure 6E; Table S6). These genomic regions corresponded to 2,291 enhancers and 1,737 promoters, and both types of regulatory regions showed either gain or loss of H3K27ac in the cKO cortex (Figure 6E). Given that PRDM16 is mostly associated with enhancers, the large number of promoter regions showing changes in H3K27ac might reflect modifications in the long-range enhancer-promoter interactions in the cKO cortex. PRDM16 bound to 997 regions that showed increased H3K27ac and 519 regions that showed reduced H3K27ac in the cKO cortex (Figure 6F). To evaluate the impact of these epigenetic changes on gene expression, we determined the percentage of misregulated genes that represent the nearest genes to PRDM16-bound regions showing H3K27ac changes in the cKO cortex. In general, upregulated genes in mutant RG and IP cells were associated with genomic regions showing increased H3K27ac, whereas downregulated genes were near regions showing reduced H3K27ac (Figures 6G and 6H). Therefore, our results suggest that PRDM16 represses and activates gene expression by modifying the epigenetic state of transcriptional enhancers.

The Epigenetic State of PRDM16-Regulated Enhancers Correlates with Gene Expression Levels in the Progeny of RG

To further assess the impact of epigenetic changes on gene expression in the cKO cortex, we investigated whether enhancer

(D) Genome-wide comparison of H3K4me in E15.5 WT and *Prdm16* cKO cortex (n = 2).

(E) Genome-wide comparison of H3K27ac in E15.5 WT and *Prdm16* cKO cortex (n = 3). Differential H3K27ac enrichment within enhancers and promoters (FDR < 0.05) is highlighted as red and blue circles, respectively.

(F) Overlap of PRDM16-binding sites with regions showing differential H3K27ac between WT and *Prdm16* cKO cortices.

(G) Percentage of nearest misregulated genes to regions showing differential H3K27ac enrichment in the cKO cortex.

(H) Genome tracks showing regions with differential H3K27ac enrichment near *Kremen1* and *Smoc1*, which are shown as examples of upregulated and downregulated genes, respectively. Significant changes in H3K27ac (FDR < 0.05) are indicated at enhancers (red boxes) and promoters (purple boxes).

Statistically significant gene expression changes were identified using an FDR < 0.05 (***adjusted p value < 0.001). See also Figures S7 and S8.

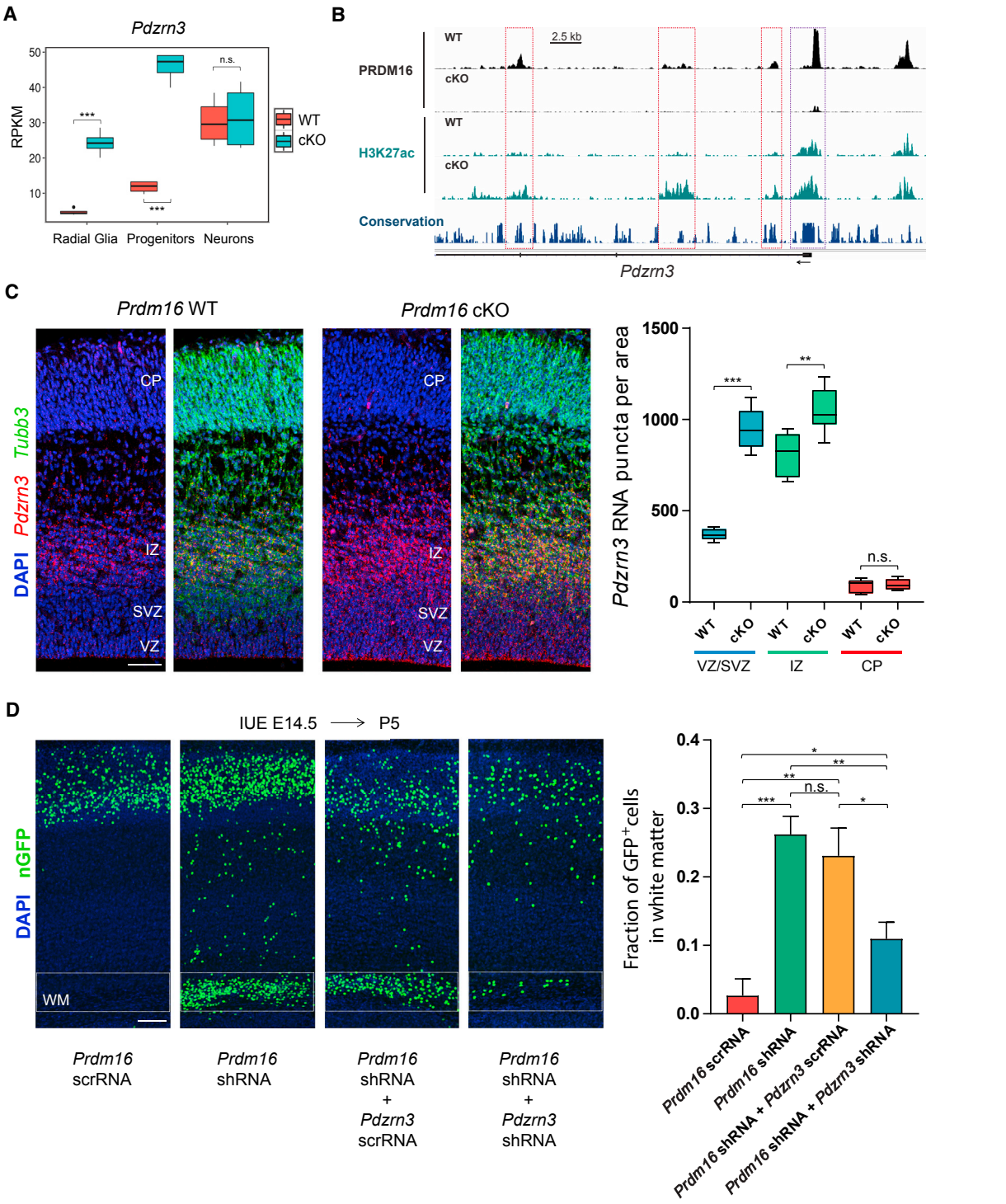

Figure 7. PRDM16 Silencing of *Pdzrn3* Controls Cortical Neuron Position

(A) *Pdzrn3* expression at three stages of differentiation in WT and *Prdm16* cKO cells.

(B) Genome tracks showing regions with differential H3K27ac enrichment near the transcription start site of *Pdzrn3*. Significant changes in H3K27ac (FDR < 0.05) are indicated at enhancers (red boxes) and promoter (purple box).

(C) *Pdzrn3* expression was analyzed by FISH in E15.5 WT and *Prdm16* cKO cortices. The number of *Pdzrn3* RNA puncta per area (10^4 μm^2) was quantified in the ventricular zone (VZ), subventricular zone (SVZ), intermediate zone (IZ), and cortical plate (CP) (n = 3).

(legend continued on next page)

activity is associated with misregulated gene expression in RG progeny (i.e., IP cells and neurons). We selected three of the top genes repressed by PRDM16 activity: *Ptx3*, *Itga6*, and *Gabra2* (Tables S1 and S3). These genes are part of a small group of upregulated genes in the cKO cortex for which expression consistently changes in RG, IP cells, and neurons (Figures S8A–S8C; Table S5). We confirmed increased PTX3 levels in the VZ, SVZ, and IZ of the cKO cortex by immunostaining (Figure S8A). Fluorescent *in situ* hybridization (FISH) of the cKO cortex indicated increased levels of *Itga6* and *Gabra2* in the VZ, SVZ, and IZ (Figures S8B and S8C). Of note, *Itga6* and *Gabra2* transcript levels were increased in the cKO cortex only during early stages of neuronal differentiation in the IZ (Figures S8B and S8C). This observation correlates well with our RNA-seq results showing progressive silencing of upregulated genes as the progeny of mutant RG differentiate into mature cortical neurons (Figures S8A–S8C). We found that *Ptx3*, *Itga6*, and *Gabra2* were the nearest genes to a group of PRDM16-bound enhancers that showed significantly increased H3K27ac in the mutant cortex (Figures S8A–S8C). The promoter regions of these genes also showed an increase in H3K27ac, even in cases where there was a complete absence of PRDM16 binding at the promoter (Figures S8A and S8B). Thus, changes in the epigenetic state of PRDM16-regulated enhancers may influence gene expression at early stages of neuronal differentiation.

Silencing of *Pdzrn3* Expression by PRDM16 Promotes Upper Layer Neuron Migration

The function of PDZRN3 in cortical development is currently unknown, although previous research has shown that it regulates endothelial cell migration *in vitro* (Sewduth et al., 2014). The probability that *Pdzrn3* is a direct transcriptional target of PRDM16 is two orders of magnitude higher than the second predicted target in both RG and IP cells (Figures 5E and 5G; Table S7). Transcriptional profiling of cortical cells indicates that PRDM16 activity strongly represses *Pdzrn3* expression in RG and IP cells (Figure 7A). PRDM16-binding sites at the promoter of *Pdzrn3* and nearby enhancer regions showed a significant increase of H3K27ac in the cKO cortex, suggesting that these regulatory regions were more active in the absence of PRDM16 (Figure 7B). In the E15.5 WT cortex, *Pdzrn3* expression was relatively low in the VZ and SVZ and high at the apical region of the IZ, as shown by FISH (Figure 7C). In the cKO cortex, *Pdzrn3* was upregulated in the VZ, SVZ, and IZ (Figure 7C). *Pdzrn3* was downregulated in fully differentiated neurons in the cortical plate (CP), and there was no difference in *Pdzrn3* expression between WT and cKO cortices in this region (Figure 7C). Thus, PRDM16 silences *Pdzrn3* in RG and during subsequent stages of differentiation by directly repressing the activity of multiple regulatory regions of this gene.

To investigate the role of PDZRN3 in the migration defects observed in the *Prdm16* cKO cortex, we used a previously described shRNA that efficiently depletes PDZRN3 (Figure S9A) (Honda et al., 2010). We simultaneously reduced *Prdm16* and *Pdzrn3* expression by *in utero* electroporation of shRNAs into WT mice at E14.5, followed by analysis of cell migration at P5. The fraction of ectopic GFP$^+$ cells in the cortical WM was not different between brains electroporated with *Prdm16* shRNA alone or in combination with *Pdzrn3* scrambled RNA (Figure 7D). In contrast, co-electroporation of *Prdm16* shRNA and *Pdzrn3* shRNA resulted in a significant reduction in the fraction of ectopic GFP$^+$ cells in the WM (Figure 7D). In all electroporations, double KD of *Prdm16* and *Pdzrn3* resulted in the absence of large heterotopias and only few scattered GFP$^+$ cells were observed in the WM (Figures 7D and S9B). Quantification of GFP$^+$ cells across 4 bins encompassing the entire cortex confirmed the reduction of the GFP$^+$ fraction close to the WM in the double KD (Figures S9B and S9C). Thus, PRDM16 silencing of *Pdzrn3* expression is necessary to establish the position of upper layer neurons.

We tested the ability of overexpressed *Pdzrn3* to disrupt migration by electroporating full-length *Pdzrn3* into E14.5 WT cortex and analyzing the position of electroporated neurons at P5 (Figure S9D). Ectopic GFP$^+$-CUX1$^+$ neurons in layers V and VI and the WM were present in brains electroporated with *Pdzrn3* compared to an empty vector (Figure S9D). We confirmed high levels of PDZRN3 in cortical neurons electroporated with *Pdzrn3* (Figure S9E). Altogether, our results suggest that *Pdzrn3* is a primary target of PRDM16 in the embryonic cortex and its transcriptional repression during early stages of neurogenesis promotes cortical neuron migration.

The Histone Methyltransferase Domain of PRDM16 Promotes Neuronal Migration through Transcriptional Repression

PRDM16 controls gene expression programs by regulating the epigenetic state of transcriptional enhancers. This function could be mediated by the intrinsic chromatin-modifying activity of the PR domain of PRDM16 (Pinheiro et al., 2012; Zhou et al., 2016). To study the role of this domain in the cortex, we generated vectors driving expression of full-length *Prdm16* (*Prdm16* F.L.) or mutant *Prdm16* lacking the sequence encoding the PR domain (Δ*PRdm16*), under the RG-specific *Hes5* promoter (Figure 8A) (Mizutani et al., 2007). *In utero* electroporation of *Prdm16* F.L. into E13.5 cKO cortex resulted in *Prdm16* expression in the VZ and SVZ and the absence of expression in the IZ and CP at E15.5 (Figure 8B). The majority of PRDM16$^+$ electroporated cells in the mutant VZ and SVZ was also PAX6$^+$ (Figure 8C). Thus, by driving *Prdm16* expression under the *Hes5* promoter *in vivo*, we could recapitulate the endogenous expression pattern of *Prdm16*.

We next tested if electroporation of *Prdm16* F.L. or Δ*PRdm16* rescued the neuronal migration defects in the cKO cortex. As expected, *in utero* electroporation of control vector into E13.5 cKO

(D) Analysis of cell migration after single knockdown (KD) of *Prdm16* or double KD of *Prdm16* and *Pdzrn3*. After E14.5 *in utero* electroporation (IUE), the fraction of GFP$^+$ cells in the white matter (WM) was quantified at P5 (n = 3, *Prdm16* scrRNA; n = 4, *Prdm16* shRNA; n = 5, *Prdm16* shRNA and *Pdzrn3* scrRNA; n = 7, *Prdm16* shRNA and *Pdzrn3* shRNA).

Data represent mean ± SE; statistical analysis is unpaired Student's t test (*$p < 0.05$, **$p < 0.01$, and ***$p < 0.001$; n.s., not significant). Scale bars, 50 μm (C) and 100 μm (D). See also Figure S9.

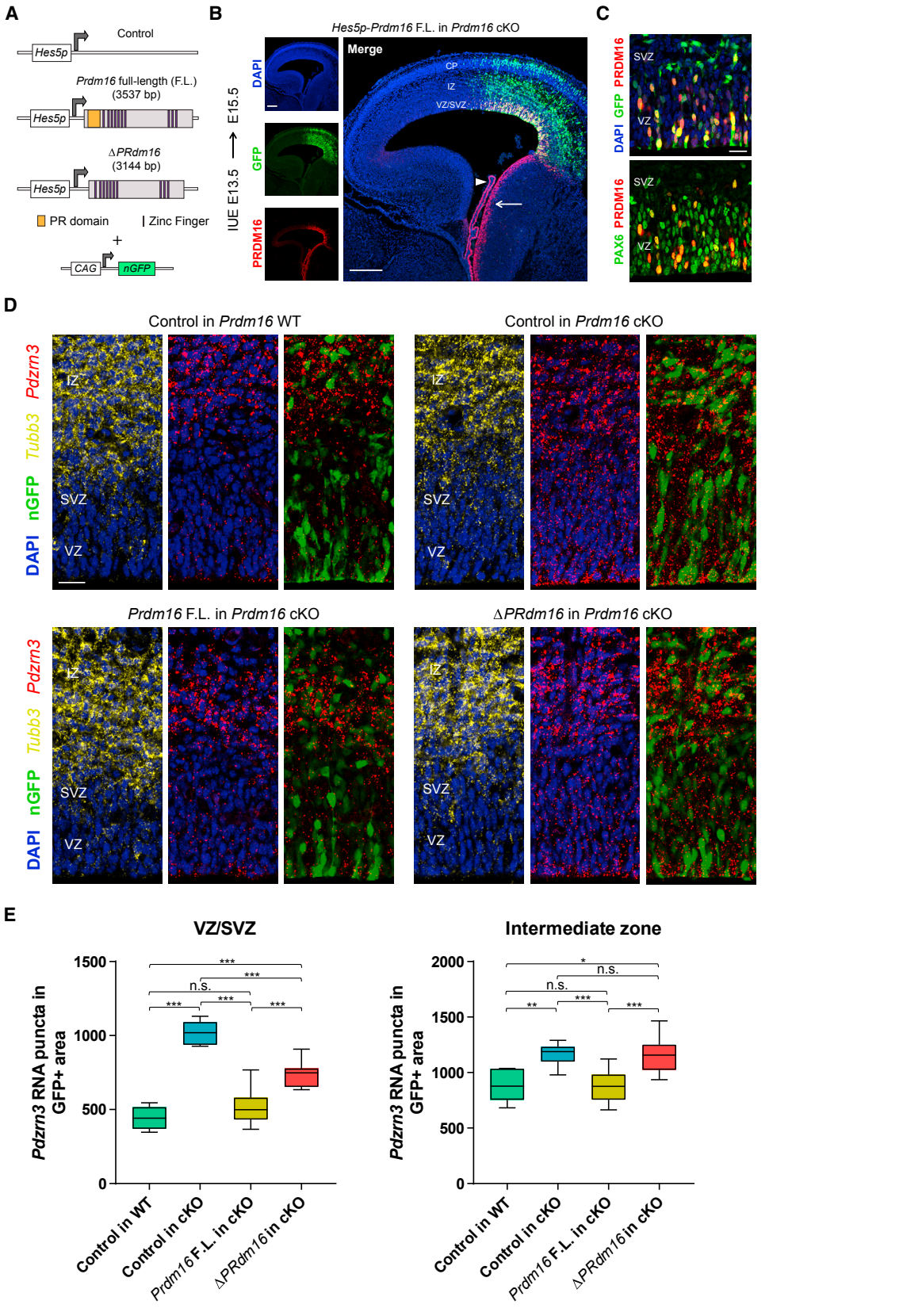

(legend on next page)

cortex resulted in relatively high numbers of ectopic GFP$^+$ cells in the WM and IZ at E18.5 in comparison to WT cortex (Figures S10A and S10B). Electroporation of *Prdm16* F.L. into the cKO cortex rescued the migration defects of GFP$^+$ cells, while electroporation of Δ*PRdm16* did not (Figures S10A and S10B). Hence, the histone methyltransferase domain of PRDM16 promotes cortical neuron migration.

PRDM16 represses the expression of genes involved in migration. Thus, we tested whether the histone methyltransferase domain of PRDM16 was necessary for silencing gene expression. Since *Pdzrn3* silencing has an important role in promoting neuronal migration, we used *Pdzrn3* expression levels in electroporated GFP$^+$ cells as a transcriptional readout of PRDM16 activity *in vivo*. *In utero* electroporation of control vector at E13.5 showed high levels of *Pdzrn3* expression in GFP$^+$ cells in the VZ and SVZ of the cKO cortex at E15.5 in comparison to the WT cortex (Figures 8D and 8E). Electroporation of *Prdm16* F.L. into the cKO cortex reduced *Pdzrn3* expression down to WT levels in GFP$^+$ cells in the VZ and SVZ, whereas Δ*PRdm16* did not restore WT levels of *Pdzrn3* expression (Figures 8D and 8E). Nonetheless, Δ*PRdm16* did repress *Pdzrn3* expression to some degree in the VZ and SVZ (Figures 8D and 8E). Given that some transcriptional targets of PRDM16 are upregulated in immature neurons in the IZ of the cKO cortex, we evaluated the influence of the PR domain on gene expression in cortical neurons. For this assay, we quantified *Pdzrn3* expression in GFP$^+$ cells in the IZ, which was identified by *Tubb3* expression (Figure 8D). Similar to our results in the VZ and SVZ, *Prdm16* F.L. fully restored *Pdzrn3* expression to WT levels in immature cortical neurons in the IZ of the cKO cortex, whereas Δ*PRdm16* did not (Figures 8D and 8E). Together, our findings suggest that epigenetic silencing of gene expression by PRDM16 activity in RG determines the position of upper layer cortical neurons.

DISCUSSION

The complexity of the mammalian cerebral cortex is developmentally encoded by gene expression programs, which orchestrate the production neuronal subtypes and their migration to specific positions in the CP. The dynamics of this process depends on intricate interactions between transcriptional complexes and changes in the permissive or repressive chromatin state of *cis*-regulatory elements across the genome. Our results suggest that PRDM16 modifies the genome-wide pattern of H3K27ac at distal enhancers to regulate gene expression in the embryonic cortex. This process is critical to regulate cortical neurogenesis and neuronal migration.

We found that a group of genes activated by PRDM16, such as *Insm1* and *Tbr2* (*Eomes*), have roles in IP cell generation and/or differentiation (Farkas et al., 2008; Mihalas et al., 2016; Sessa et al., 2008). In addition, almost 10% of PRDM16-regulated regions contain the TBR2 (EOMES)-binding motif. We propose that PRDM16 activates a transcriptional program that promotes indirect neurogenesis, thereby establishing the correct number of upper layer cortical projection neurons.

Late-born cortical upper layer neurons cannot reach their final positions when they originate from RG lacking PRDM16 activity. Loss of *Prdm16* in cortical RG leads to the upregulation of cell migration genes, some of which have reported roles in repressing migration in the cortex, such as *Itga6* and *Gabra2* (Georges-Labouesse et al., 1998; Heck et al., 2007). Thus, PRDM16 might keep a subset of cell migration genes repressed in RG and IP cells, thereby establishing the proper timing for the onset of cortical neuron migration. We established that repression of *Pdzrn3* by PRDM16 activity promotes migration of upper layer neurons. Identifying the substrates of PDZRN3 ubiquitin ligase activity should provide insight into the molecular regulation of neuron migration.

Transcriptional enhancers have been extensively mapped in the developing mouse and human cerebral cortices (de la Torre-Ubieta et al., 2018; Visel et al., 2013). However, much less is known about how genome-wide modifications in enhancer activity control specific cellular behaviors, such as proliferation and migration, to assemble cortical circuits. We identified over 2,000 PRDM16-bound enhancers showing changes in H3K27ac levels in the developing *Prdm16* cKO cortex. Upregulated genes in the cKO cortex are preferentially associated with enhancers showing increased H3K27ac, whereas downregulated genes are near enhancers showing decreased H3K27ac. Therefore, PRDM16 might regulate the permissive or repressive chromatin state of enhancer elements, thereby promoting or antagonizing gene expression. These findings raise the possibility that, during embryonic neurogenesis, the number and position of cortical neurons are encoded in RG by the dynamic patterns of histone methylations and acetylations within enhancer regions.

Chromatin modifications influence gene expression across cell lineages during neurogenesis (Hirabayashi and Gotoh, 2010). We found that loss of PRDM16 activity in cortical RG promotes upregulation of *Ptx3*, *Gabra2*, *Itga6*, and *Pdzrn3*

Figure 8. The Histone Methyltransferase Domain of PRDM16 Promotes Transcriptional Silencing

(A) Vectors driving *Prdm16* full-length (F.L.) and Δ*PRdm16* expression from the *Hes5* proximal promoter. The experimental vectors were co-electroporated with a plasmid driving constitutive expression of nuclear GFP.

(B) *In utero* electroporation (IUE) of *Hes5p-Prdm16* F.L. into *Prdm16* cKO cortex. Endogenous *Prdm16* expression in the choroid plexus (arrowhead) and lateral ganglionic eminence (arrow) is indicated.

(C) IUE of *Hes5p-Prdm16* F.L. into E13.5 *Prdm16* cKO cortex shows that PRDM16 overlaps with PAX6 in most electroporated cells in the ventricular zone (VZ) and few cells in the subventricular zone (SVZ) at E15.5.

(D) *In vivo* transcriptional assay of PRDM16 activity in the embryonic cortex. The indicated vectors were electroporated into E13.5 WT or cKO cortex, and *Pdzrn3* expression in GFP$^+$ cells in the VZ, SVZ, and intermediate zone (IZ) was evaluated at E15.5 by fluorescence *in situ* hybridization. The IZ was identified by *Tubb3* expression.

(E) Quantification of *Pdzrn3* puncta in GFP$^+$ cells in the cortical VZ, SVZ, and IZ of electroporated brains. Results represent number of RNA puncta in 10^4 μm^2 (n = 3). Statistical analysis is unpaired Student's t test (*p < 0.05, **p < 0.01, and ***p < 0.001; n.s., not significant). Scale bars, 200 μm (B) and 20 μm (C and D). See also Figure S10.

expression in IP cells in the SVZ and immature neurons in the IZ. Upregulation of these genes in immature cortical neurons is associated with increased activity of nearby enhancers in the cKO cortex. Thus, a role of PRDM16 as a chromatin-modifying enzyme involved in the inheritance of transient transcriptional states during cortical neurogenesis is an interesting possibility. Additional experiments are needed to assess whether PRDM16-bound enhancers remain misregulated once *Prdm16* is no longer expressed in cortical neurons and whether this is functionally relevant for the migration defects in the cKO cortex. Regardless of the mechanisms involved in this process, our results show that transcriptional changes in RG have a permanent impact on the final laminar position of their neuronal progeny. This evidence highlights how transiently executed transcriptional programs have long-lasting effects in the organization of the cerebral cortex.

Previous *in vitro* studies have shown that PRDM16 methylates H3K9 to promote transcriptional repression or H3K4 to activate transcription (Pinheiro et al., 2012; Zhou et al., 2016). In this study, we did not detect changes in H3K4 methylation in the cKO cortex, suggesting this is not the predominant function of PRDM16 in this context. We also tested the role of the PR domain of PRDM16 in transcriptional regulation and cortical neuron migration. Our data suggest that the activity of the PR domain is critical in RG to repress gene expression and to determine the migration of upper layer neurons. In this scenario, methylation of H3K9 by PRDM16 could mediate transcriptional repression in the embryonic cortex. Isolation of cortical RG will be necessary to increase the sensitivity of ChIP-seq experiments to resolve the role of PRDM16 as an H3K9 or H3K4 mono-methyltransferase *in vivo*.

We found that Δ*PRdm16* retains some gene-silencing activity, suggesting that other repressor domains of PRDM16, such as the CtBP-binding motifs, might also be important to repress gene expression in the embryonic cortex (Kajimura et al., 2008). Together, our findings suggest that the histone methyltransferase activity of PRDM16 regulates chromatin states at enhancer regions in RG and this mechanism encodes the position of their neuronal progeny. Further experiments are necessary to understand how the activity of the PR domain and PRDM16-interacting co-factors operate in conjunction to modify the pattern of histone modifications and chromatin accessibility within cortical enhancer elements.

PRDM16 haploinsufficiency is correlated with brain malformations and intellectual disability in humans with 1p36 deletion syndrome (Jordan et al., 2015). Human-gained enhancers are preferentially associated with genes expressed in outer RG, and they are potentially important for human-specific neural development and disease (de la Torre-Ubieta et al., 2018; Doan et al., 2016; Reilly et al., 2015). Defining the role of PRDM16 and other histone-modifying enzymes at human-specific enhancers and their importance in neurodevelopmental disorders is an outstanding area for future research.

STAR★METHODS

Detailed methods are provided in the online version of this paper and include the following:

SUPPLEMENTAL INFORMATION

Supplemental Information includes ten figures and eight tables and can be found with this article online at https://doi.org/10.1016/j.neuron.2018.04.033.

ACKNOWLEDGMENTS

We are grateful to Bruce Spiegelman (Dana Farber Cancer Institute) and Paul Cohen (The Rockefeller University) for providing the *Prdm16*$^{flox/flox}$ mouse line. We thank Patrick Seale (University of Pennsylvania) and Barbara Bottazzi (Humanitas Research, Italy) for sharing reagents. We thank Lisa Goodrich, Michael Greenberg, and Constance Cepko (Harvard Medical School) for critical reading of the manuscript. J.-M.B. was supported by the Pew Latin American fellow program, an Alice and Joseph Brooks fellowship, and the William Randolph Hearst Fund. M.T.G. was supported by the Ellen and Melvin Gordon fellowship. This work was supported by the Harvard NeuroDiscovery Center and grants from the NIH (R01NS102228) and the Edward R. and Anne G. Lefler Center to C.H.

AUTHOR CONTRIBUTIONS

J.-M.B. and C.C.H. conceived the project, designed the experiments, interpreted the results, and wrote the manuscript. J.-M.B. performed most of the experiments. M.M. performed *in silico* analysis of sequencing data. M.T.G. quantified cortical cell types, progenitor proliferation, and cell cycle exit. N.G., O.O., and D.T. contributed with animal surgeries and immunostainings. O.O. performed real-time PCR analysis. M.B.J. and C.A.W. provided ferret and human samples. All authors read and contributed to the final version of the manuscript.

DECLARATION OF INTERESTS

The authors declare no competing interests.

Received: July 31, 2017
Revised: March 14, 2018
Accepted: April 24, 2018
Published: May 17, 2018; corrected online June 27, 2018

SUPPORTING CITATIONS

The following references appear in the Supplemental Information: Bjork et al. (2010a).

REFERENCES

Arai, Y., Pulvers, J.N., Haffner, C., Schilling, B., Nüsslein, I., Calegari, F., and Huttner, W.B. (2011). Neural stem and progenitor cells shorten S-phase on commitment to neuron production. Nat. Commun. *2*, 154.

Arnold, S.J., Huang, G.J., Cheung, A.F.P., Era, T., Nishikawa, S., Bikoff, E.K., Molnár, Z., Robertson, E.J., and Groszer, M. (2008). The T-box transcription factor Eomes/Tbr2 regulates neurogenesis in the cortical subventricular zone. Genes Dev. *22*, 2479–2484.

Bjork, B.C., Turbe-Doan, A., Prysak, M., Herron, B.J., and Beier, D.R. (2010a). Prdm16 is required for normal palatogenesis in mice. Hum. Mol. Genet. *19*, 774–789.

Bjork, B.C., Fujiwara, Y., Davis, S.W., Qiu, H., Saunders, T.L., Sandy, P., Orkin, S., Camper, S.A., and Beier, D.R. (2010b). A transient transgenic RNAi strategy for rapid characterization of gene function during embryonic development. PLoS ONE *5*, e14375.

Chi, J., and Cohen, P. (2016). The multifaceted roles of PRDM16: Adipose biology and beyond. Trends Endocrinol. Metab. *27*, 11–23.

Chuikov, S., Levi, B.P., Smith, M.L., and Morrison, S.J. (2010). Prdm16 promotes stem cell maintenance in multiple tissues, partly by regulating oxidative stress. Nat. Cell Biol. *12*, 999–1006.

Cohen, P., Levy, J.D., Zhang, Y., Frontini, A., Kolodin, D.P., Svensson, K.J., Lo, J.C., Zeng, X., Ye, L., Khandekar, M.J., et al. (2014). Ablation of PRDM16 and beige adipose causes metabolic dysfunction and a subcutaneous to visceral fat switch. Cell *156*, 304–316.

Creyghton, M.P., Cheng, A.W., Welstead, G.G., Kooistra, T., Carey, B.W., Steine, E.J., Hanna, J., Lodato, M.A., Frampton, G.M., Sharp, P.A., et al. (2010). Histone H3K27ac separates active from poised enhancers and predicts developmental state. Proc. Natl. Acad. Sci. USA *107*, 21931–21936.

de la Torre-Ubieta, L., Stein, J.L., Won, H., Opland, C.K., Liang, D., Lu, D., and Geschwind, D.H. (2018). The dynamic landscape of open chromatin during human cortical neurogenesis. Cell *172*, 289–304.

Doan, R.N., Bae, B.I., Cubelos, B., Chang, C., Hossain, A.A., Al-Saad, S., Mukaddes, N.M., Oner, O., Al-Saffar, M., Balkhy, S., et al.; Homozygosity Mapping Consortium for Autism (2016). Mutations in human accelerated regions disrupt cognition and social behavior. Cell *167*, 341–354.e12.

Dobin, A., Davis, C.A., Schlesinger, F., Drenkow, J., Zaleski, C., Jha, S., Batut, P., Chaisson, M., and Gingeras, T.R. (2013). STAR: ultrafast universal RNA-seq aligner. Bioinformatics *29*, 15–21.

Englund, C., Fink, A., Lau, C., Pham, D., Daza, R.A., Bulfone, A., Kowalczyk, T., and Hevner, R.F. (2005). Pax6, Tbr2, and Tbr1 are expressed sequentially by radial glia, intermediate progenitor cells, and postmitotic neurons in developing neocortex. J. Neurosci. *25*, 247–251.

Farkas, L.M., Haffner, C., Giger, T., Khaitovich, P., Nowick, K., Birchmeier, C., Pääbo, S., and Huttner, W.B. (2008). Insulinoma-associated 1 has a panneurogenic role and promotes the generation and expansion of basal progenitors in the developing mouse neocortex. Neuron *60*, 40–55.

Georges-Labouesse, E., Mark, M., Messaddeq, N., and Gansmüller, A. (1998). Essential role of alpha 6 integrins in cortical and retinal lamination. Curr. Biol. *8*, 983–986.

Goebbels, S., Bormuth, I., Bode, U., Hermanson, O., Schwab, M.H., and Nave, K.A. (2006). Genetic targeting of principal neurons in neocortex and hippocampus of NEX-Cre mice. Genesis *44*, 611–621.

Gorski, J.A., Talley, T., Qiu, M., Puelles, L., Rubenstein, J.L.R., and Jones, K.R. (2002). Cortical excitatory neurons and glia, but not GABAergic neurons, are produced in the Emx1-expressing lineage. J. Neurosci. *22*, 6309–6314.

Guillemot, F., and Hassan, B.A. (2017). Beyond proneural: emerging functions and regulations of proneural proteins. Curr. Opin. Neurobiol. *42*, 93–101.

Harms, M.J., Lim, H.W., Ho, Y., Shapira, S.N., Ishibashi, J., Rajakumari, S., Steger, D.J., Lazar, M.A., Won, K.J., and Seale, P. (2015). PRDM16 binds MED1 and controls chromatin architecture to determine a brown fat transcriptional program. Genes Dev. *29*, 298–307.

Heck, N., Kilb, W., Reiprich, P., Kubota, H., Furukawa, T., Fukuda, A., and Luhmann, H.J. (2007). GABA-A receptors regulate neocortical neuronal migration in vitro and in vivo. Cereb. Cortex *17*, 138–148.

Heintzman, N.D., Stuart, R.K., Hon, G., Fu, Y., Ching, C.W., Hawkins, R.D., Barrera, L.O., Van Calcar, S., Qu, C., Ching, K.A., et al. (2007). Distinct and predictive chromatin signatures of transcriptional promoters and enhancers in the human genome. Nat. Genet. *39*, 311–318.

Heinz, S., Benner, C., Spann, N., Bertolino, E., Lin, Y.C., Laslo, P., Cheng, J.X., Murre, C., Singh, H., and Glass, C.K. (2010). Simple combinations of lineage-determining transcription factors prime cis-regulatory elements required for macrophage and B cell identities. Mol. Cell *38*, 576–589.

Hirabayashi, Y., and Gotoh, Y. (2010). Epigenetic control of neural precursor cell fate during development. Nat. Rev. Neurosci. *11*, 377–388.

Hohenauer, T., and Moore, A.W. (2012). The Prdm family: expanding roles in stem cells and development. Development *139*, 2267–2282.

Honda, T., Yamamoto, H., Ishii, A., and Inui, M. (2010). PDZRN3 negatively regulates BMP-2-induced osteoblast differentiation through inhibition of Wnt signaling. Mol. Biol. Cell *21*, 3269–3277.

Hrvatin, S., Deng, F., O'Donnell, C.W., Gifford, D.K., and Melton, D.A. (2014). MARIS: method for analyzing RNA following intracellular sorting. PLoS ONE *9*, e89459.

Hsu, L.C.-L., Nam, S., Cui, Y., Chang, C.-P., Wang, C.-F., Kuo, H.-C., Touboul, J.D., and Chou, S.-J. (2015). Lhx2 regulates the timing of β-catenin-dependent cortical neurogenesis. Proc. Natl. Acad. Sci. USA *112*, 12199–12204.

Inoue, M., Iwai, R., Tabata, H., Konno, D., Komabayashi-Suzuki, M., Watanabe, C., Iwanari, H., Mochizuki, Y., Hamakubo, T., Matsuzaki, F., et al. (2017). Prdm16 is crucial for progression of the multipolar phase during neural differentiation of the developing neocortex. Development *144*, 385–399. Published online December 19, 2016.

Jordan, V.K., Zaveri, H.P., and Scott, D.A. (2015). 1p36 deletion syndrome: an update. Appl. Clin. Genet. *8*, 189–200.

Kajimura, S., Seale, P., Tomaru, T., Erdjument-Bromage, H., Cooper, M.P., Ruas, J.L., Chin, S., Tempst, P., Lazar, M.A., and Spiegelman, B.M. (2008). Regulation of the brown and white fat gene programs through a PRDM16/CtBP transcriptional complex. Genes Dev. *22*, 1397–1409.

Kowalczyk, T., Pontious, A., Englund, C., Daza, R.A.M., Bedogni, F., Hodge, R., Attardo, A., Bell, C., Huttner, W.B., and Hevner, R.F. (2009). Intermediate neuronal progenitors (basal progenitors) produce pyramidal-projection neurons for all layers of cerebral cortex. Cereb. Cortex *19*, 2439–2450.

Kwan, K.Y., Sestan, N., and Anton, E.S. (2012). Transcriptional co-regulation of neuronal migration and laminar identity in the neocortex. Development *139*, 1535–1546.

Langmead, B., Trapnell, C., Pop, M., and Salzberg, S.L. (2009). Ultrafast and memory-efficient alignment of short DNA sequences to the human genome. Genome Biol. *10*, R25.

Li, Q., Brown, J.B., Huang, H., and Bickel, P.J. (2011). Measuring reproducibility of high-throughput experiments. Ann. Appl. Stat. *5*, 1752–1779.

Liao, Y., Smyth, G.K., and Shi, W. (2014). featureCounts: an efficient general purpose program for assigning sequence reads to genomic features. Bioinformatics *30*, 923–930.

LoTurco, J.J., and Bai, J. (2006). The multipolar stage and disruptions in neuronal migration. Trends Neurosci. *29*, 407–413.

Love, M.I., Huber, W., and Anders, S. (2014). Moderated estimation of fold change and dispersion for RNA-seq data with DESeq2. Genome Biol. *15*, 550.

Lui, J.H., Hansen, D.V., and Kriegstein, A.R. (2011). Development and evolution of the human neocortex. Cell *146*, 18–36.

Lui, J.H., Nowakowski, T.J., Pollen, A.A., Javaherian, A., Kriegstein, A.R., and Oldham, M.C. (2014). Radial glia require PDGFD-PDGFRβ signalling in human but not mouse neocortex. Nature *515*, 264–268.

Martin, M. (2011). Cutadapt removes adapter sequences from high-throughput sequencing reads. EMBnet J. *17*, 10.

Mastrototaro, G., Zaghi, M., and Sessa, A. (2017). Epigenetic mistakes in neurodevelopmental disorders. J. Mol. Neurosci. *61*, 590–602.

Matsuda, T., and Cepko, C.L. (2004). Electroporation and RNA interference in the rodent retina in vivo and in vitro. Proc. Natl. Acad. Sci. USA *101*, 16–22.

Mihalas, A.B., Elsen, G.E., Bedogni, F., Daza, R.A.M., Ramos-Laguna, K.A., Arnold, S.J., and Hevner, R.F. (2016). Intermediate progenitor cohorts differentially generate cortical layers and require Tbr2 for timely acquisition of neuronal subtype identity. Cell Rep. *16*, 92–105.

Mizutani, K., Yoon, K., Dang, L., Tokunaga, A., and Gaiano, N. (2007). Differential Notch signalling distinguishes neural stem cells from intermediate progenitors. Nature *449*, 351–355.

Molyneaux, B.J., Arlotta, P., Menezes, J.R.L., and Macklis, J.D. (2007). Neuronal subtype specification in the cerebral cortex. Nat. Rev. Neurosci. *8*, 427–437.

Nashun, B., Hill, P.W.S., and Hajkova, P. (2015). Reprogramming of cell fate: epigenetic memory and the erasure of memories past. EMBO J. *34*, 1296–1308.

Nishimura, M., Isaka, F., Ishibashi, M., Tomita, K., Tsuda, H., Nakanishi, S., and Kageyama, R. (1998). Structure, chromosomal locus, and promoter of mouse Hes2 gene, a homologue of Drosophila hairy and Enhancer of split. Genomics *49*, 69–75.

Noctor, S.C., Flint, A.C., Weissman, T.A., Dammerman, R.S., and Kriegstein, A.R. (2001). Neurons derived from radial glial cells establish radial units in neocortex. Nature *409*, 714–720.

Noctor, S.C., Martínez-Cerdeño, V., Ivic, L., and Kriegstein, A.R. (2004). Cortical neurons arise in symmetric and asymmetric division zones and migrate through specific phases. Nat. Neurosci. *7*, 136–144.

Palmer, T.D., Markakis, E.A., Willhoite, A.R., Safar, F., and Gage, F.H. (1999). Fibroblast growth factor-2 activates a latent neurogenic program in neural stem cells from diverse regions of the adult CNS. J. Neurosci. *19*, 8487–8497.

Pinheiro, I., Margueron, R., Shukeir, N., Eisold, M., Fritzsch, C., Richter, F.M., Mittler, G., Genoud, C., Goyama, S., Kurokawa, M., et al. (2012). Prdm3 and Prdm16 are H3K9me1 methyltransferases required for mammalian heterochromatin integrity. Cell *150*, 948–960.

Rada-Iglesias, A., Bajpai, R., Swigut, T., Brugmann, S.A., Flynn, R.A., and Wysocka, J. (2011). A unique chromatin signature uncovers early developmental enhancers in humans. Nature *470*, 279–283.

Ramírez, F., Ryan, D.P., Grüning, B., Bhardwaj, V., Kilpert, F., Richter, A.S., Heyne, S., Dündar, F., and Manke, T. (2016). deepTools2: a next generation web server for deep-sequencing data analysis. Nucleic Acids Res. *44* (W1), W160–W165.

Reilly, S.K., Yin, J., Ayoub, A.E., Emera, D., Leng, J., Cotney, J., Sarro, R., Rakic, P., and Noonan, J.P. (2015). Evolutionary genomics. Evolutionary changes in promoter and enhancer activity during human corticogenesis. Science *347*, 1155–1159.

Reimand, J., Kull, M., Peterson, H., Hansen, J., and Vilo, J. (2007). g:Profiler–a web-based toolset for functional profiling of gene lists from large-scale experiments. Nucleic Acids Res. *35*, W193–W200.

Seale, P., Kajimura, S., Yang, W., Chin, S., Rohas, L.M., Uldry, M., Tavernier, G., Langin, D., and Spiegelman, B.M. (2007). Transcriptional control of brown fat determination by PRDM16. Cell Metab. *6*, 38–54.

Sessa, A., Mao, C.A., Hadjantonakis, A.K., Klein, W.H., and Broccoli, V. (2008). Tbr2 directs conversion of radial glia into basal precursors and guides neuronal amplification by indirect neurogenesis in the developing neocortex. Neuron *60*, 56–69.

Sewduth, R.N., Jaspard-Vinassa, B., Peghaire, C., Guillabert, A., Franzl, N., Larrieu-Lahargue, F., Moreau, C., Fruttiger, M., Dufourcq, P., Couffinhal, T., and Duplàa, C. (2014). The ubiquitin ligase PDZRN3 is required for vascular morphogenesis through Wnt/planar cell polarity signalling. Nat. Commun. *5*, 4832.

Shimada, I.S., Acar, M., Burgess, R.J., Zhao, Z., and Morrison, S.J. (2017). Prdm16 is required for the maintenance of neural stem cells in the postnatal forebrain and their differentiation into ependymal cells. Genes Dev. *31*, 1134–1146.

Stamatoyannopoulos, J.A., Snyder, M., Hardison, R., Ren, B., Gingeras, T., Gilbert, D.M., Groudine, M., Bender, M., Kaul, R., Canfield, T., et al.; Mouse ENCODE Consortium (2012). An encyclopedia of mouse DNA elements (Mouse ENCODE). Genome Biol. *13*, 418.

Stewart, S.A., Dykxhoorn, D.M., Palliser, D., Mizuno, H., Yu, E.Y., An, D.S., Sabatini, D.M., Chen, I.S.Y., Hahn, W.C., Sharp, P.A., et al. (2003). Lentivirus-delivered stable gene silencing by RNAi in primary cells. RNA *9*, 493–501.

Supek, F., Bošnjak, M., Škunca, N., and Šmuc, T. (2011). REVIGO summarizes and visualizes long lists of gene ontology terms. PLoS ONE *6*, e21800.

Trichas, G., Begbie, J., and Srinivas, S. (2008). Use of the viral 2A peptide for bicistronic expression in transgenic mice. BMC Biol. *6*, 40.

Tuoc, T.C., Boretius, S., Sansom, S.N., Pitulescu, M.E., Frahm, J., Livesey, F.J., and Stoykova, A. (2013). Chromatin regulation by BAF170 controls cerebral cortical size and thickness. Dev. Cell *25*, 256–269.

Visel, A., Taher, L., Girgis, H., May, D., Golonzhka, O., Hoch, R.V., McKinsey, G.L., Pattabiraman, K., Silberberg, S.N., Blow, M.J., et al. (2013). A high-resolution enhancer atlas of the developing telencephalon. Cell *152*, 895–908.

Wang, S., Sun, H., Ma, J., Zang, C., Wang, C., Wang, J., Tang, Q., Meyer, C.A., Zhang, Y., and Liu, X.S. (2013). Target analysis by integration of transcriptome and ChIP-seq data with BETA. Nat. Protoc. *8*, 2502–2515.

Zhang, Y., Liu, T., Meyer, C.A., Eeckhoute, J., Johnson, D.S., Bernstein, B.E., Nussbaum, C., Myers, R.M., Brown, M., Li, W., and Liu, X.S. (2008). Model-based analysis of ChIP-seq (MACS). Genome Biol. *9*, R137.

Zhao, C., Teng, E.M., Summers, R.G., Jr., Ming, G.L., and Gage, F.H. (2006). Distinct morphological stages of dentate granule neuron maturation in the adult mouse hippocampus. J. Neurosci. *26*, 3–11.

Zhou, B., Wang, J., Lee, S.Y., Xiong, J., Bhanu, N., Guo, Q., Ma, P., Sun, Y., Rao, R.C., Garcia, B.A., et al. (2016). PRDM16 suppresses MLL1r leukemia via intrinsic histone methyltransferase activity. Mol. Cell *62*, 222–236.

Zhu, J., Adli, M., Zou, J.Y., Verstappen, G., Coyne, M., Zhang, X., Durham, T., Miri, M., Deshpande, V., De Jager, P.L., et al. (2013). Genome-wide chromatin state transitions associated with developmental and environmental cues. Cell *152*, 642–654.

STAR★METHODS

KEY RESOURCES TABLE

REAGENT or RESOURCE	SOURCE	IDENTIFIER
Antibodies		
Rat monoclonal anti-CTIP2	Abcam	Cat #ab18465; RRID: AB_2064130
Mouse monoclonal anti-S100β	Abcam	Cat #ab11178; RRID: AB_297817
Rabbit polyclonal anti-TBR1	Abcam	Cat #ab31940; RRID: AB_2200219
Rat monoclonal anti-pH3	Abcam	Cat #ab10543; RRID: AB_2295065
Mouse monoclonal anti-NEUN	Millipore	Cat #MAB377; RRID: AB_2298772
Mouse monoclonal anti-VGLUT2	Millipore	Cat #MAB5504; RRID: AB_2187552
Chicken polyclonal anti-TBR2	Millipore	Cat #AB15894; RRID: AB_10615604
Mouse monoclonal anti-NESTIN	Millipore	Cat #MAB353; RRID: AB_94911
Mouse monoclonal anti-SATB2	Santa Cruz	Cat #sc-81376; RRID: AB_1129287
Rabbit polyclonal anti-CUX1	Santa Cruz	Cat #sc-13024
Mouse monoclonal anti-RORβ	R&D Systems	Cat #PP-H3925-00; RRID: AB_2254092
Chicken polyclonal anti-GFP	Aves Labs	Cat #GFP-1020; RRID: AB_10000240
Rabbit polyclonal anti-pH3	Sigma-Aldrich	Cat #H0412; RRID: AB_477043
Mouse monoclonal anti-KI67	BD PharMingen	Cat #550609; RRID: AB_393778
Rat monoclonal anti-KI67	Affymetrix	Cat #14-5698
Rabbit polyclonal anti-PAX6	BioLegend	Cat #901301; RRID: AB_2565003
Mouse monoclonal anti-PAX6	DSHB	RRID: AB_528427
Rabbit polyclonal anti-RFP	MBL International	Cat #PM005; RRID: AB_591279
Rabbit polyclonal anti-BRN2	GeneTex	Cat #GTX114650
Rabbit polyclonal anti-PDZRN3	Novus Biologicals	Cat #NBP2-55802
Rabbit polyclonal anti-PTX3	Barbara Bottazzi, Humanitas Research	N/A
Rabbit polyclonal anti-PRDM16	Patrick Seale, University of Pennsylvania	N/A
Rabbit polyclonal anti-H3K27ac	Abcam	Cat #ab4729; RRID: AB_2118291
Rabbit polyclonal anti-H3K4me	Abcam	Cat #ab8895; RRID: AB_306847
Goat polyclonal anti-Mouse Alexa 488	Thermo Fisher Scientific	Cat #A11001; RRID: AB_2534069
Goat polyclonal anti-Mouse Alexa 546	Thermo Fisher Scientific	Cat #A11003; RRID: AB_2534071
Goat polyclonal anti-Mouse Alexa 647	Thermo Fisher Scientific	Cat #A21235; RRID: AB_2535804
Goat polyclonal anti-Chicken Alexa 488	Thermo Fisher Scientific	Cat #A11039; RRID: AB_2534096
Goat polyclonal anti-Rabbit Alexa 488	Thermo Fisher Scientific	Cat #A11034; RRID: AB_2576217
Goat polyclonal anti-Rabbit Alexa 546	Thermo Fisher Scientific	Cat #A11010; RRID: AB_2534077
Goat polyclonal anti-Rabbit Alexa 647	Thermo Fisher Scientific	Cat #A21244; RRID: AB_2535812
Goat polyclonal anti-Rat Alexa 488	Thermo Fisher Scientific	Cat #A11006; RRID: AB_2534074
Bacterial and Virus Strains		
Replication-incompetent enhanced GFP-expressing retrovirus	Palmer et al., 1999	N/A
Chemicals, Peptides, and Recombinant Proteins		
EGS [ethylene glycolbis(succinimidylsuccinate)]	Thermo Scientific	Cat #21565
Blocking reagent for nucleic acid hybridization	Roche	Cat #11096176001
Critical Commercial Assays		
Ovation Ultralow System V2 1–16	NuGEN	Cat #0344
Ovation RNA-Seq System V2	NuGEN	Cat #7102

(*Continued on next page*)

Continued

REAGENT or RESOURCE	SOURCE	IDENTIFIER
RecoverAll Total Nucleic Acid Isolation	Ambion	Cat #AM1975
Click-iT EdU Imaging	Invitrogen	Cat #C10340
Deposited Data		
RNA-seq data	This paper	GEO: GSE111660
ChIP-seq data	This paper	GEO: GSE111657, GSE111658, GSE111659, GSE111661
Experimental Models: Cell Lines		
HEK293 retrovirus packaging cell line	Palmer et al., 1999	293 gp NIT-GFP
Experimental Models: Organisms/Strains		
Mouse: C57BL/6	Charles River Laboratories	Strain code: 027
Mouse: CD-1	Charles River Laboratories	Strain code: 022
Mouse: B6.129-Prdm16$^{tm1.1Brsp}$/J	The Jackson Laboratory	Stock #024992
Mouse: Emx1$^{tm1(cre)Krj}$/J	The Jackson Laboratory	Stock #005628
Mouse: B6.Cg-Gt(ROSA)26So$^{rtm14(CAG-tdTomato)Hze}$/J	The Jackson Laboratory	Stock #007914
Mouse: Neurod6$^{tm1(cre)Kan}$	Goebbels et al., 2006	MGI: 5308766
Oligonucleotides		
Prdm16 shRNA, exon 5 Forward: 5′-GTTGGTGCATGTGAAAGAATTCAAGA GATTCTTTCACATGCACCAAC-3′ Reverse: 5′-GTTGGTGCATGTGAAAGAATCTCTTG AATTCTTTCACATGCACCAAC-3′	Bjork et al., 2010b	N/A
Prdm16 scrambled control Forward: 5′-GCGGAGAAAGTGGATTTATTTCAAGA GAATAAATCCACTTTCTCCGC-3′ Reverse: 5′-GCGGAGAAAGTGGATTTATTCTCTTG AAATAAATCCACTTTCTCCGC-3′	Bjork et al., 2010b	N/A
Pdzrn3 shRNA, exon 10 Forward: 5′-GCTCAGAACAGGAGAATAACGTTCA AGAGACGTTATTCTCCTGTTCTGAGCCTTTTTG-3′ Reverse: 5′-AATTCAAAAAGGCTCAGAACAGGAGAA TAACGTCTCTTGAACGTTATTCTCCTGTTCTGAGC-3′	Honda et al., 2010	N/A
Pdzrn3 scrambled control Forward: 5′-GCAAGGACAGACACGGAATATTTCAAG AGAATATTCCGTGTCTGTCCTTGCCTTTTTG-3′ Reverse: 5′-AATTCAAAAAGGCAAGGACAGACACGG AATATTCTCTTGAAATATTCCGTGTCTGTCCTTGC-3′	Honda et al., 2010	N/A
PR domain deletion Forward: 5′-GAAGGTGCCTACTCCTTG-3′ Reverse: 5′-TGGGATTGGAATGTCTTC-3′	This paper	N/A
Real-Time PCR, *In situ* hybridization and RNA scope	This paper	Table S8
Recombinant DNA		
pCAG-TAG	Trichas et al., 2008	Addgene #26771
CAG-GFP-IRES-CRE	Zhao et al., 2006	Addgene #48201
pCAGIG	Matsuda and Cepko, 2004	Addgene #11159
pCMV-VSV-G	Stewart et al., 2003	Addgene #8454
Hes5-Luc	Nishimura et al., 1998	Addgene #41724
pcDNA3.1 *Prdm16*	Seale et al., 2007	Addgene #15503
pCAG-*Prdm16*-IRES-*GFP*	This paper	N/A
Hes5p-Prdm16-IRES-*GFP*	This paper	N/A
Hes5p-ΔPRdm16-IRES-*GFP*	This paper	N/A
pCAGIG *Pdzrn3*	This paper	N/A

(*Continued on next page*)

Continued

REAGENT or RESOURCE	SOURCE	IDENTIFIER
Software and Algorithms		
ImageJ/ Fiji 1.49S	Wayne Rasband, National Institutes of Health	https://imagej.net/Fiji
Imaris 7.0	Bitplane	http://www.bitplane.com/releasenotes/imaris700.aspx
Integrative Genomics Viewer (IGV) 2.3	Broad Institute MIT/Harvard	http://software.broadinstitute.org/software/igv/
MATLAB R2017b	MathWorks	https://www.mathworks.com/products/matlab.html
Cutadapt	Martin, 2011	https://cutadapt.readthedocs.io/en/stable/
STAR	Dobin et al., 2013	http://code.google.com/p/rna-star/
FeatureCounts	Liao et al., 2014	http://subread.sourceforge.net
DESeq2	Love et al., 2014	http://www.bioconductor.org/packages/release/bioc/html/DESeq2.html
gProfiler	Reimand et al., 2007	http://biit.cs.ut.ee/gprofiler/
REVIGO	Supek et al., 2011	http://revigo.irb.hr/
Bowtie2 2.2.8	Langmead et al., 2009	http://bowtie-bio.sourceforge.net/index.shtml
MACS2 2.1.1	Zhang et al., 2008	https://pypi.python.org/pypi/MACS2
IDR R package	Li et al., 2011	http://cran.r-project.org/web/packages/idr/index.html
HOMER v.4.6 suite	Heinz et al., 2010	http://homer.ucsd.edu/homer/
DeepTools2	Ramírez et al., 2016	deeptools.ie-freiburg. mpg.de
BETA v.1.0.7	Wang et al., 2013	http://cistrome.org/BETA/

CONTACT FOR REAGENT AND RESOURCE SHARING

Further information and requests for reagents may be directed to, and will be fulfilled by, the Lead Contact and corresponding author, Corey Harwell (corey_harwell@hms.harvard.edu).

EXPERIMENTAL MODEL AND SUBJECT DETAILS

All animal procedures conducted in this study were performed in accordance with the protocol approved by the Institutional Animal Care and Use Committee of Harvard Medical School. The mouse lines used in this study and their source are indicated in the Key Resources Table. Mouse housing and husbandry conditions followed the standards set by the Division of Comparative Medicine at Harvard Medical School. Embryonic (E) day 10-17 and postnatal (P) day 0-15 mice, P2 ferret kits, and gestational week (GW) 20 and 22 human embryonic tissue was used for this study. For all mouse studies the sex of embryos and postnatal pups was not determined. The sex of the ferret kits was not determined. Sex was not determined in GW20 human fetal tissue, and GW22 was identified as female.

Human Tissue Specimens and Processing

Research performed on samples of human origin was conducted according to protocols approved under expedited category 5 with waiver of consent (45 CFR 46.110) by the institutional review boards of Beth Israel Deaconess Medical Center and Boston Children's Hospital. Fetal brain tissue was received after release from clinical pathology, with a maximum post-mortem interval of 4 hr. Cases with known anomalies were excluded. Gestational ages were determined using fetal foot length. Tissue was transported in HBSS medium on ice to the laboratory for research processing.

METHOD DETAILS

In Situ Hybridization

Two digoxigenin-labeled RNA probes were generated to detect *Prdm16* transcripts. One probe hybridizes with exon 4-8 and the other hybridizes with exon 9 (Table S8). Both probes gave almost identical *Prdm16* expression patterns. To generate probe templates, exon 4-8 and exon 9 sequences were amplified by PCR from E14.5 mouse brain cDNA and cloned into pGEM-T easy vector (Promega). Antisense and sense probes were transcribed using T3 and T7 RNA polymerases and digoxigenin-labeled dNTPs

(Roche). Probes were purified in polyacrylamide micro Bio-Spin columns (Bio-Rad), recovered in 20 μL of RNase-free water and diluted in 1 mL of hybridization buffer (see below) to generate a 10X probe solution. We performed colorimetric *in situ* hybridization on RNase-free cryostat sections using standard protocols. Briefly, brain sections were hybridized overnight at 65°C with probe solution in hybridization buffer (50% formamide, 5X SSC pH 5.0, 50 μg/ml yeast RNA, 1% SDS and 50 μg/ml heparin). The following day, sections were washed, treated with RNase A (20 μg/ml), incubated for 2 hr in blocking buffer (100 mM maleic acid pH 7.5, 150 mM NaCl, 0.1% Tween 20, 20% goat serum and 2% Roche blocking reagent) and then incubated overnight at 4°C with anti-DIG antibody conjugated to alkaline phosphatase (Roche) diluted 1:2000 in blocking buffer. The following day, sections were washed and alkaline phosphatase was developed with BM purple (Roche). Sections were washed and mounted using Fluoromount-G (Southern Biotech).

Fluorescent *in situ* hybridization (FISH) was done by following the RNAscope protocol (Advanced Cell Diagnostics) on cryostat sections of PFA-fixed tissue according to the manufacturer's instructions. Double FISH was done by combining RNAscope probes against mouse *Pdzrn3*, *Itga6* or *Gabra2* with a probe against *Tubb3* (Table S8). For electroporation experiments, double FISH was followed by immunofluorescence to detect GFP on the same tissue sections.

Immunofluorescence and EdU Labeling

Immunostaining of cellular proteins was done according to standard protocols. Briefly, mice pups at postnatal day 5, 8, 10 and 15 were anesthetized by intraperitoneal injection of ketamine (100 mg/Kg) - xylazine (12.5 mg/Kg) mix and transcardially perfused with PBS 1X pH 7.4 followed by 4% PFA. Brains were dissected and fixed in 4% PFA overnight at 4°C with rocking. Next day, brains were washed with PBS and sectioned into 100 μm vibratome sections or cryoprotected overnight in 30% sucrose to generate 20 μm cryostat sections. We performed antigen retrieval in all our immunostainings in order to enhance antibody signal. Vibratome and cryostat sections were incubated in antigen retrieval solution (10 mM sodium citrate, 0.05% Tween 20, pH 6.0) for 1 hr at 70°C. After incubation, sections were allowed to cool down at room temperature (RT), washed 3 times in PBS, incubated in blocking buffer (10% goat serum, 0.1% Triton X-100, 0.01% sodium azide in PBS) for 1-2 hr and then incubated with primary antibodies in blocking buffer at 4°C overnight. The next day, sections were washed 3 times with PBS and incubated with Alexa Fluor-conjugated secondary antibodies in blocking buffer for 1-2 hr at RT. Sections were washed and nuclei stained with DAPI (4',6-diamidino-2-phenylindole) before mounting with Fluoromount-G (Southern Biotech). DNA synthesis in neural progenitors was detected by EdU (5-ethynyl-2′-deoxyuridine) injection (approximately 5-20 μg/g of body weight) into the peritoneal cavity of pregnant mice or newborn pups. EdU incorporation was detected with the Click-iT assay (Invitrogen) using Alexa Fluor 647 azide according to the manufacturer's instructions. Images were acquired with a Leica DM6000 FS epifluorescence microscope, a Leica SP8 confocal microscope and a Zeiss LSM 700 confocal microscope. Images were processed with Leica LAS X and Zen 2011 software or ImageJ.

In Utero Electroporation

Timed pregnant mice were anesthetized using an isoflurane vaporizer and placed on a warming pad. An abdominal incision of about 1 inch in length was made and the uterine horns were carefully exposed on top of a sterile gauze pad. Embryos were kept moist with pre-warmed PBS at 37°C during the entire procedure. Approximately, 0.5-1.0 μL of endotoxin-free DNA (1-3 μg/μl) diluted in PBS/0.025% Fast Green (SIGMA) was injected into the lateral ventricles of the forebrain using heat-pulled glass micropipettes (Drummond). Once all embryos were injected, 5 pulses of 30-40 V (50 ms duration and 950 ms intervals) were applied with 5 mm or 7 mm platinum electrodes (BTX) connected to an ECM 830 square wave electroporator (BTX). The abdominal cavity was then sutured and stapled before administering buprenorphine (0.05-0.1 mg/kg) and ketoprofen (5-10 mg/kg). Mice were allowed to recover in a 37°C chamber for 2 hr after surgery. Plasmids coding for *Prdm16* shRNA and scrambled control were electroporated at 1 μg/μl, whereas vectors coding for *Pdzrn3* shRNA and scrambled control were injected at 1.5 μg/μl. All shRNA and scrambled controls were combined with 0.5 μg/μl of pCAG-TAG (Addgene) to permanently label the nuclei of cortical neurons with GFP. Vectors coding for full-length *Prdm16* or Δ*Prdm16* were electroporated at 2.5 μg/μl in combination with 0.5 μg/μl of pCIG (Addgene). When needed, we used a neutral plasmid as 'filler DNA' in order to reach a final plasmid concentration of 3.0 μg/μl in all in utero electroporations.

Retrovirus Production

Human embryonic kidney 293 gp NIT-GFP retrovirus packaging cell line was grown to 90% confluency in DMEM (GIBCO) supplemented with 10% Fetal Bovine Serum and transfected with pCMV-VSV-G vector using lipofectamine 2000 (Invitrogen) and Optimem (GIBCO). Karyotyping suggests this cell line is derived from female tissue. Two days after transfection, cell supernatant was collected, filtered through 0.45 μm filter (VWR International) and centrifuged at 25000 rpm for 90 min at 4°C. After centrifugation, 100 μL of cold PBS plus Ca^{+2} were added to the pellet and incubated at 4°C over 12 hr. Viral particles were gently resuspended with a pipette and split into aliquots that were stored at - 80°C. Viral particles with a titer of 10^6-10^7 PFU/ml were used for in utero injections into the lateral ventricles of E14.5 mouse embryos.

Fluorescence Activated Cell Sorting Using Intracellular Antibodies

Sorting of immunostained cortical cells for transcriptional profiling was based on a previously described protocol (Hrvatin et al., 2014). Briefly, cortical tissue was dissected from E15.5 embryos and kept on ice in Hibernate-E (GIBCO) supplemented with B27 (GIBCO) during identification of WT and cKO genotypes among littermates. WT and cKO cortices were pooled by genotype and resuspended in digest solution containing 0.25% Trypsin (Invitrogen) and 0.01% DNase (SIGMA) in Hibernate-E minus Ca (BrainBits).

Tissues were incubated at 37°C for 10 min in digest solution, washed twice in fresh Hibernate-E/B27 plus 0.01% DNase and mechanically dissociated into a single cell suspension. Cells were fixed in 4% PFA plus 0.1% saponin for 30 min at 4°C, then washed twice in washing buffer (0.1% saponin, 0.2% BSA in PBS) and resuspended in antibody buffer (0.1% saponin, 1% BSA in PBS) containing anti-PAX6 and anti-TBR2 antibodies and incubated for 0.5-1 hr at 4°C with rocking. Cells were washed twice, then incubated with Alexa Fluor-conjugated secondary antibodies for 0.5 hr at 4°C with rocking, washed twice, and resuspended in 400 μL of recovery buffer (0.5% BSA in PBS). All steps from fixation onward were carried out with RNase-free reagents and solutions were treated with either 1:25 RNasin (fixing/antibody/recovery buffers) or 1:100 RNasin (washing buffer). Cells were sorted with a FACS Aria IIU sorter (BD Biosciences) using FACS Diva 8.0 software. Thresholds for 488 nm and 633 nm sorting gates were set using cells stained only with secondary antibodies as reference. Approximately 170,000-210,000 cells were collected for each population ($PAX6^+$, $TBR2^+$ and $PAX6^-$-$TBR2^-$) in every biological replicate.

RNA Sequencing

Sorted cells were centrifuged and resuspended in 100 μL of lysis solution of RecoverAll total nucleic acid isolation kit (Ambion) and incubated for 3 hr at 50°C. RNA was then purified according to manufacturer's instructions. The concentration and quality of purified RNA was determined using BioAnalyzer (Agilent). Normally, we recovered around 0.1 pg of RNA per cell and the total amount of RNA recovered was in the range of 5-40 ng for each sorted cell type. RNA integrity numbers (RIN) were in the range of 7.3 to 9.6. RNA was reverse-transcribed into cDNA and amplified by RNA-based single primer isothermal amplification (SPIA) using the Ovation RNA-seq system V2 (NuGEN). Synthesized cDNA was sonicated using a Covaris S2 ultrasonicator to reduce the fragment size range to 100-600 bp. The genotype of littermate embryos was further confirmed at this point by qPCR amplification of *Prdm16* exon 9. For library preparation, 100 ng of sheared cDNA was end repaired, ligated with barcoded adaptors, amplified for 9 PCR cycles and purified using the Ovation Ultralow System V2 (NuGEN). Libraries were sequenced in an Illumina HiSeq 2500 sequencer to a sequencing depth of 28-40 million reads per sample. Gene expression differences among RNA-seq samples were confirmed for a subset of genes by real-time PCR analysis using purified cDNA of sorted cells, custom primers (Table S8) and SYBR Green master mix (Bio-Rad). Normalization of gene expression levels was done using *Gapdh* as reference. Reactions were run in a CFX96 Real-Time PCR Thermal Cycler (Bio-Rad).

Chromatin Immunoprecipitation and Sequencing

Approximately 20-40 million E15.5 cortical cells were dual crosslinked by incubating in 1.5 mM EGS (ethylene glycol bis[succinimidyl succinate]) solution (Thermo Scientific) for 20 min at RT with rotation and then 1% PFA plus 1.5 mM EGS for an additional 10 min at RT. Crosslinking was quenched by adding glycine to a final concentration of 125 mM and rotating for 5 min at RT. Cells were then washed twice with cold PBS 1X plus EDTA-free protease inhibitor (Roche), centrifuged and stored at −80°C or freshly resuspended in lysis buffer (20 mM Tris-HCl pH 8.0, 85 mM KCl, 0.5% NP40) and incubated on ice for 30 min. Nuclei were pelleted by centrifugation at 1500 *g* for 5 min, resuspended in SDS buffer (0.2% SDS, 20 mM Tris-HCl pH 8.0, 1 mM EDTA) and incubated on ice for 10 min. Nuclei were then sonicated using a Covaris S2 ultrasonicator for shearing chromatin in the range of 100-500 bp fragments. After spinning chromatin at 18,000 *g* for 10 min, supernatant was transferred to a clean tube and one volume of 2X ChIP dilution buffer (0.1% sodium deoxycholate, 2% Triton X-100, 2 mM EDTA, 30 mM Tris-HCl pH 8.0, 300 mM NaCl) was added. At this step, a volume of supernatant containing around 0.5 million nuclei was set aside as input control and the remaining supernatant was incubated with 5 μg of anti-PRDM16 antibody overnight at 4°C with rotation. Next day, 50 μL of washed protein G beads (22.5 mg/ml; Novex) were added to the chromatin solution and incubated for 2 hr at 4°C. After incubation, beads were washed twice with low salt wash buffer (0.1% SDS, 1% Triton X-100, 2 mM EDTA, 20 mM Tris-HCl pH 8.0, 150 mM NaCl) followed by two washes with high salt wash buffer (0.1% SDS, 1% Triton X-100, 2 mM EDTA, 20 mM Tris-HCl pH 8.0, 500 mM NaCl) then two washes with LiCl wash buffer (0.25 M LiCl, 0.5% NP40, 0.5% sodium deoxycholate, 1 mM EDTA, 10 mM Tris-HCl pH 8.0) and finally two washes with TE pH 8.0 (10 mM Tris-HCl, 1 mM EDTA). Beads were then resuspended in 90 μL of freshly prepared ChIP elution buffer (1% SDS, 0.1 M NaHCO3) and incubated at 65°C for 30 min with rotation. The recovered supernatant was incubated in reverse crosslinking solution (250 mM Tris-HCl pH 6.5, 62.5 mM EDTA pH 8.0, 1.25 M NaCl, 5 mg/ml of Proteinase K) at 65°C overnight. DNA was then extracted with phenol/chloroform/isoamyl alcohol, precipitated with 3 M sodium acetate pH 5.0 and resuspended in TE pH 8.0 low EDTA (10 mM Tris-HCl, 0.1 mM EDTA). Finally, samples were treated with RNase A (100 μg/ml) for 30 min at 37°C.

For library preparation, genomic DNA was purified, end repaired, ligated with barcoded adaptors, amplified for 11 PCR cycles and purified using the Ovation Ultralow System V2 (NuGEN) according to manufacturer's instructions. Library fragments in the range of 100-800 bp were size-selected using agarose gel electrophoresis followed by DNA gel extraction (QIAGEN). Recovered DNA was further cleaned and concentrated using a column (Zymo Research). Libraries were sequenced in an Illumina HiSeq 2500 sequencer to a sequencing depth of 30-40 million reads per sample.

Native Chromatin Immunoprecipitation and Sequencing

Embryonic cortical tissue was dissected and ground on ice using 1.5 mL tubes and a plastic pestle. The tissue was resuspended in 100 μL of buffer 1 (0.3 M Sucrose, 60 mM KCl, 15 mM NaCl, 5 mM MgCl2, 0.1 mM EGTA, 15 mM Tris-HCl pH7.5, 0.5 mM DTT, 1 mM PMSF, 1X EDTA-free protease inhibitor) and lysed on ice for 7 min by adding 100 μL of buffer 2 (buffer 1 plus 0.4% Noniodet-40 substitute). Samples were centrifuged at 8500 rpm for 7 min and resuspended in 100 μL of micrococcal nuclease buffer (0.3 M Sucrose,

50 mM Tris-HCl pH 7.5, 4 mM MgCl2, 1 mM CaCl2, 0.1 mM PMSF and 1X EDTA-free protease inhibitor) before adding another 100 μL of micrococcal nuclease buffer containing 1 μL of micrococcal nuclease at 2X10^6 U/ml (New England Biolabs). Samples were incubated for 10 min at 37°C and the reaction was stopped with 10 μL of 0.5 M EDTA. Samples were centrifuged at 10000 rpm for 10 min, the supernatants (sup #1) were collected and the pellets incubated overnight in 200 μL of dialysis buffer (1 mM Tris-HCl pH 7.5, 0.2 mM EDTA, 1 mM PMSF, 1X EDTA-free protease inhibitor) with rocking at 4°C. The dialyzed samples were centrifuged and the recovered supernatants were combined with sup #1. The supernatants (400 μL total volume) were diluted to 4 mL with ChIP dilution buffer (0.01% SDS, 1.1% Triton X-100, 1.2 mM EDTA, 16.7 mM Tris-HCl pH 8.0, 167 mM NaCl, 1 mM PMSF, 1X EDTA-free protease inhibitor) and 40 μL of protein G Dyna Beads were added to pre-clear the chromatin for 1 hr. Up to this step, all solutions contained 50 mM Na Butyrate for subsequent immunoprecipitation of H3K27ac. Beads were removed and the chromatin samples were incubated overnight with 4 μg of anti-H3K27ac or anti-H3K4me antibody with rocking at 4°C. The following day, chromatin samples were incubated for 3 hr with 40 μL of protein G Dyna Beads that were previously blocked overnight with 2 mg/ml BSA and 3 mg/ml tRNA. Bead-bound chromatin samples were sequentially washed with low salt buffer, high salt buffer and LiCl buffer (one time each) and then twice with TE buffer. Bead-bound chromatin was eluted with ChIP elution buffer (1% SDS, 0.1% NaHCO3) for 40 min at 65°C and treated with 0.1 μg/μl of RNase A, followed by 0.05 μg/μl of Proteinase K. Genomic DNA was purified using the ChIP Clean and Concentrator kit (Zymo Research). Before proceeding to library preparation, immunoprecipitation of H3K27ac or H3K4me was confirmed by ChIP-qPCR using primers designed to amplify genomic regions with high H3K27ac or H3K4me enrichment, according to the ENCODE datasets. Additional sets of primers were designed to amplify genomic regions with low H3K27ac or H3K4me enrichment and used as negative controls. Library preparation and size selection were done as described above for transcription factor ChIP-seq.

Prdm16 and Pdzrn3 Knockdown

Oligonucleotides coding for shRNA directed against exon 5 of *Prdm16* or exon 10 of *Pdzrn3* and scrambled controls (Key Resources Table) were annealed, phosphorylated, and cloned downstream of the human U6 promoter of the pBluescript/U6 plasmid. The specificity of *Prdm16* shRNA was determined by in utero electroporation using an anti-PRDM16 antibody. The specificity of *Pdzrn3* KD was determined by transfection of HEK293 fibroblasts with vectors expressing either *Pdzrn3* shRNA or scrambled control (both at 1 μg/μl) in combination with a plasmid encoding full-length *Pdzrn3* under a CAG promoter (0.2 μg/μl). HEK293 cells were transfected for 2 hr at 37°C with Optimem solution (GIBCO) containing plasmid DNA and Lipofectamine 2000 (Invitrogen). After incubation, media was removed and cells were incubated for 2 days. Total RNA was isolated from transfected cells with TRIzol reagent (Invitrogen) and reverse transcribed. The relative expression of *Pdzrn3* in transfected cells was quantified by real-time PCR using custom primers.

Cloning and Site-Directed Mutagenesis

The full-length sequence of *Pdzrn3* was cloned into the EcoRI and NotI sites of pGAGIG (Addgene). To generate the *Hes5p-Prdm16* F.L.-IRES-GFP and *Hes5p-ΔPRdm16*-IRES-GFP vectors, the proximal promoter region of *Hes5* (−685 to +28 bp from TSS) was PCR-amplified from *Hes5p-Luc* plasmid (Addgene) and cloned into the SalI and EcoRI sites of pCAGIG (Addgene), resulting in replacement of the entire CAG promoter by the *Hes5* promoter (*Hes5p*-IRES-GFP control vector). The full-length coding sequence of *Prdm16* was obtained from the pcDNA3.1-*Prdm16* vector (Addgene). To optimize mRNA translation, we changed the sequence immediately upstream of the start codon (*GTAGTC*ATG) to a consensus Kozak sequence (*GCCACC*ATG) using QuikChange II site-directed mutagenesis (Agilent). Kozak-corrected *Prdm16* was cloned into the EcoRI site of the control vector to generate the *Hes5p-Prdm16* F.L.-IRES-GFP final vector. An in-frame deletion of the nucleotide sequence coding for the entire PR domain of PRDM16 (amino acids 82-211, based on UniProt) was done with the Q5 site-directed mutagenesis kit (New England Biolabs) to generate the *Hes5p-ΔPRdm16*-IRES-GFP vector. The sequence of all vectors was confirmed using custom primers. Antibody staining was necessary to detect GFP expression from these vectors. For simplicity, vectors are indicated as *Hes5p-Prdm16* F.L. and *Hes5p-ΔPRdm16* in the main text.

RNaseq Analysis

Read Mapping and Expression Level Estimation

All samples were processed using an RNA-seq pipeline implemented in the bcbio-nextgen project (https://bcbio-nextgen.readthedocs.io/en/latest/). Raw reads were examined for quality issues using FastQC (http://www.bioinformatics.babraham.ac.uk/projects/fastqc/) to ensure library generation and sequencing data were suitable for further analysis. If necessary, adaptor sequences, other contaminant sequences such as polyA tails and low quality sequences were trimmed from reads using Cutadapt. Trimmed reads were aligned to the UCSC build mm10 of the mouse genome using STAR, and counts of reads aligning to known genes were generated by featureCounts. Quality of alignments was assessed by checking for evenness of coverage, rRNA content, genomic context of alignments (for example, alignments in known transcripts and introns), complexity and other quality checks. Principal components analysis (PCA) and hierarchical clustering methods validated clustering of samples from the same library run across different sequencing lanes. Read counts were aggregated for each library by taking the sum across lanes for each gene.

Differential Gene Expression and Functional Enrichment Analysis

Differential expression was performed at the gene level using the R Bioconductor package DESeq2. For each cell type, significant genes were identified using an FDR threshold of 0.05. Lists of differentially expressed genes were separated by direction of

expression change and examined by gProfiler for statistical enrichment of information such as Gene Ontology (GO) terms, biological pathways and human disease annotations. Functional redundancy in over-represented GO terms identified by gProfiler was reduced with REVIGO for a visual representation of the most prominent processes.

ChIP-Seq Analysis

Read Mapping and Peak Calling

For all ChIP-seq datasets, sequence quality was evaluated using FASTQC (http://www.bioinformatics.babraham.ac.uk/projects/fastqc/), and if required, reads were trimmed with Cutadapt. High quality sequencing reads were mapped to the mouse genome UCSC build mm10 using Bowtie2 v2.2.8. Alignments were filtered to retain only reads with a unique mapping to the genome. ChIP-seq peaks were called with MACS2 v2.1.1 using default parameters and a narrow peak cutoff of $q < 0.05$ for PRDM16 WT and cKO samples. For histone modifications (i.e., H3K27ac and H3K4me) broad peak calling was used and a broad peak cutoff was set to $q < 0.05$. The reproducibility of peaks across replicates within each dataset was assessed by running samples through the IDR pipeline, in which peak consistency was validated by use of pooled pseudo-replicates. The pooled pseudo-replicates resulted in a number of peaks within a factor of 2 of the original results suggesting highly reproducible replicates. A consensus set of IDR-optimized peaks was identified for each dataset by merging peaks across replicates for regions with an IDR < 0.05. For comparison of PRDM16 binding sites with H3K27ac peaks, a less stringent consensus set of peaks without IDR filtering was used. This consensus set was comprised of peaks with a minimum of 1 bp overlap between replicates.

Peak Annotation

ChIP-seq peaks were annotated using the HOMER v4.6 suite of tools. Annotations were determined using nearest gene analysis which is based on distance of the peak to the nearest TSS and RefSeq annotations were used to determine associated genomic features.

Motif Analysis

Only the top 100 peaks, ranked by signal value (i.e., -log10 p value of the merged region), were used as input for motif analysis. HOMER conducts *de novo* motif analysis by parsing input sequences into unique 100 bp oligos from the peak center and read into a table. Each oligo is counted and the hypergeometric test is used to calculate the oligos significant enrichment across all target sequences. The q-value represents the FDR-corrected probability of that motif being over-represented among target sequences. Enrichment of known motifs is calculated similar to *de novo* analysis but screening against a database of previously determined high quality motifs.

Differential Enrichment Analysis

Comparisons of peak read density between WT and cKO samples was evaluated using the R Bioconductor package DiffBind. For each dataset, the full set of MACS2 peak calls from each sample was used as input rather than the IDR-optimized regions. Peaks were identified as differentially enriched if the DESeq2 analysis reported an FDR < 0.05. Differences in PRDM16 binding between WT and cKO samples were assessed by reducing the full set of cKO peak calls down to only those regions overlapping with the IDR-optimized WT peaks, and normalized read density values were plotted against each other to illustrate differential enrichment.

External Data Resources

For comparison of PRDM16 binding sites to other known histone marks, the ENCODE database was used to obtain ChIP-seq data from mouse E14.5 whole brains (https://www.encodeproject.org/reference-epigenomes/ENCSR205YGI/). For samples in which bigWig files existed, those files were downloaded directly from ENCODE, otherwise mm10 aligned BAM files were downloaded and converted to bigWig format using deepTools. ChIP-seq tracks were visualized using the Integrative Genomics Viewer 2.3 (Broad Institute, Harvard/MIT). For the assessment of PRDM16 binding overlap with developmental and adult enhancer regions, we used the IDR-optimized PRDM16 peaks and evaluated overlaps with H3K27ac ENCODE datasets using Bedtools v.2.26.0. Genomic regions bound by PRDM16 within 1 Kb upstream of the TSS were classified as promoters and removed from the analysis. Developmental enhancers were defined as PRDM16 peaks that overlap with H3K27ac peaks in E14.5 brains. Developmental and adult enhancers were defined as PRDM16 peaks that overlap with H3K27ac peaks in both E14.5 brains and 8 weeks old adult cortex. Analysis was carried out based on a minimal reciprocal fraction of peak overlap set at 20%.

Binding and Expression Target Analysis (BETA)

To identify significant associations between PRDM16 binding sites and differentially expressed genes from RNA-seq analysis, we used the BETA-plus sub-protocol from BETA v1.0.7 (Wang et al., 2013). Instead of assigning one-to-one mapping between binding sites and genes, BETA models the influence of a binding site on the expression of a gene. Two files are required as input: the IDR-optimized set of PRDM16 binding sites and RNA-seq analysis results containing statistics from differential expression analysis. BETA first calculates a Regulatory Potential Score for each gene, which is based on the number of sites within 200 kb of the TSS for that gene and the sum of distances between those sites and the gene's TSS. A rank product is then computed, by taking the differential expression statistic for each gene and the RP value, which reflects its significance as a potential target gene. The final target gene lists only include genes from the RNA-seq expression file that i) meets the defined threshold of FDR < 0.05 and ii) contains binding sites within the 200 kb region.

QUANTIFICATION AND STATISTICAL ANALYSIS

Cell counting was done either manually with ImageJ/Fiji cell counter (National Institute of Health, USA) or automatically with Imaris 7.0 software (Bitplane) using anatomically equivalent regions at the somatosensory cortex. Analysis of cell migration was done in ImageJ or Imaris by dividing the thickness of the cortex into four or five bins of equal size and the number of $CUX1^+$ or GFP^+ cells in each bin was counted and presented as the fraction of the total CUX^+ or GFP^+ neurons. Quantification of RG units only included those clones with a primary RG extending a basal process into the CP. Axonal quantifications were done using ImageJ/Fiji software. Briefly, the straighten tool was used to define a broad ipsilateral or contralateral area of interest in pCAG-TAG electroporated brains. A square (1500 X 600 pixels) was drawn at the region of interest and background was subtracted in that area using the rolling ball radius tool set at 2 pixels. After background subtraction, mean fluorescence intensity and integrated density were measured in the squared area. A region of the image with no axonal projections was selected and the mean fluorescence intensity was determined; this value was used as background intensity. The axonal projections were quantified using the following formula: corrected fluorescence intensity = integrated density - (area of square x background intensity).

Quantification of neuronal nuclei in whole hemisphere sections and quantification of RNA puncta per unit area or overlapping GFP signal was carried out automatically using a data processing pipeline in MATLAB R2017b guided by MatBots (https://hms-idac.github.io/MatBots). To count neuronal nuclei, we used nuclei fragmentation value of 0.9 and adjusted the threshold values (range 0.06 to 0.1) according to the signal intensity of CUX1, CTIP2 and SATB2. Quantification of RNA puncta was done using the SpotsInNucleiBot by selecting the Advanced Log function, sigma value of 2.0, and alpha values of 0.01 for *Pdzrn3* puncta and 0.001 for *Itga6* and *Gabra2* puncta. The total area of GFP^+ cells was quantified using the simple thresholding option with a fragmentation value in the range of 0.90 to 0.99, threshold value of 0.05 and sigma value of 1.0, whereas default settings were used for all other parameters. The number of RNA puncta in 10^4 μm^2 of VZ and SVZ, IZ or CP tissue is reported for WT and cKO cortex. RNA puncta on GFP^+ cells is reported as puncta number in 10^4 μm^2 of GFP^+ area. After automatic quantification of nuclei numbers, GFP^+ nuclear area and RNA puncta, a subset of the images was overlapped with the output masks to verify accuracy. Data outliers were verified and discarded if the generated mask did not represent the real data

Values represent mean ± SE or mean ± SD as indicated in figure legends. For each experiment, the number of replicates (n) is also indicated in figure legends. Significance was determined using the two-tailed unpaired Student's t test and reported as: $^*p < 0.05$, $^{**}p < 0.01$, $^{***}p < 0.001$.

Neuron, Volume *98*

Supplemental Information

The Epigenetic State of PRDM16-Regulated Enhancers in Radial Glia Controls Cortical Neuron Position

José-Manuel Baizabal, Meeta Mistry, Miguel Turrero García, Nicolás Gómez, Olubusola Olukoya, Diana Tran, Matthew B. Johnson, Christopher A. Walsh, and Corey C. Harwell

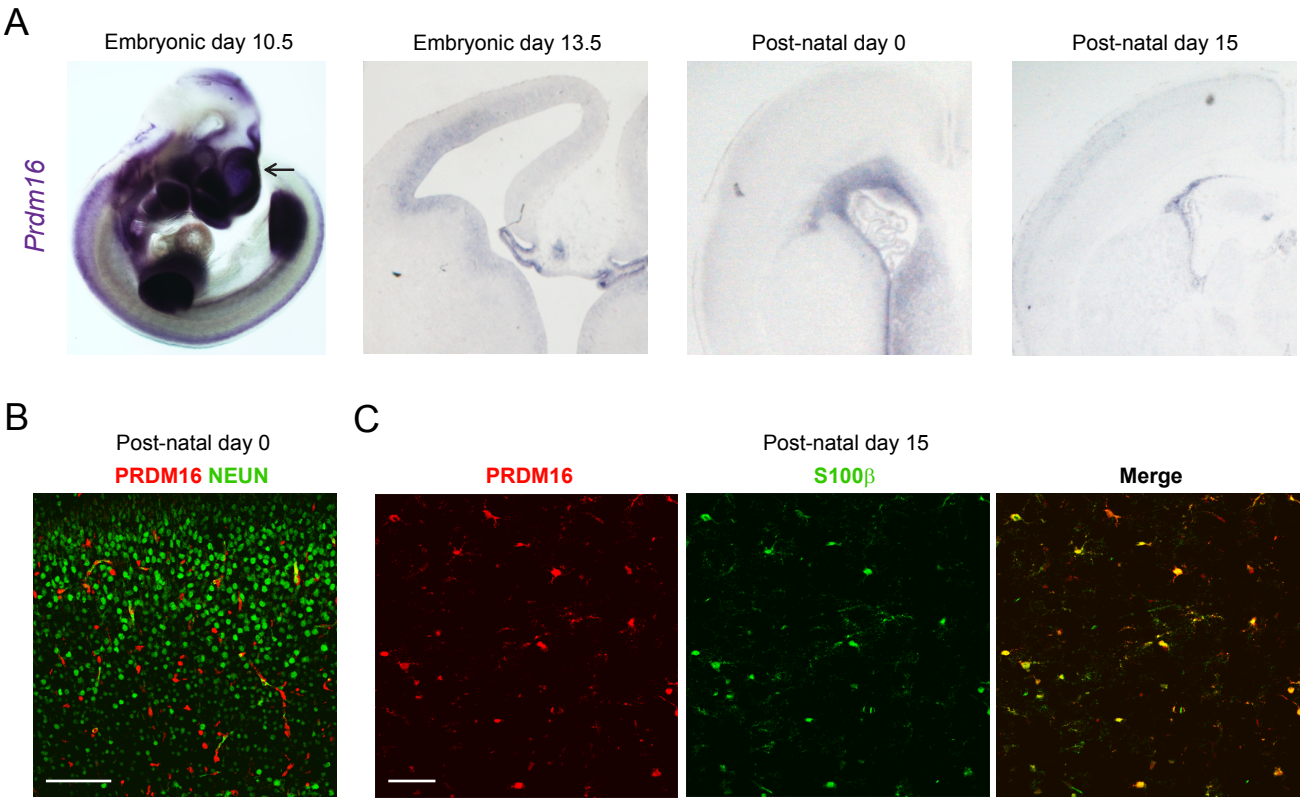

Figure S1. *Prdm16* expression during mouse cerebral cortex development. Related to Figure 1.

(A) *In situ* hybridization shows *Prdm16* expression in the ventricular zone during mouse embryonic and postnatal cortical development. Arrow indicates the dorsal telencephalon.

(B) Immunostaining for PRDM16 and NEUN in the cerebral cortex indicates that *Prdm16* is not expressed in cortical neurons.

(C) Immunostaining for PRDM16 and S100β indicates expression of *Prdm16* in cortical astrocytes.

Scale bars: 50 μm.

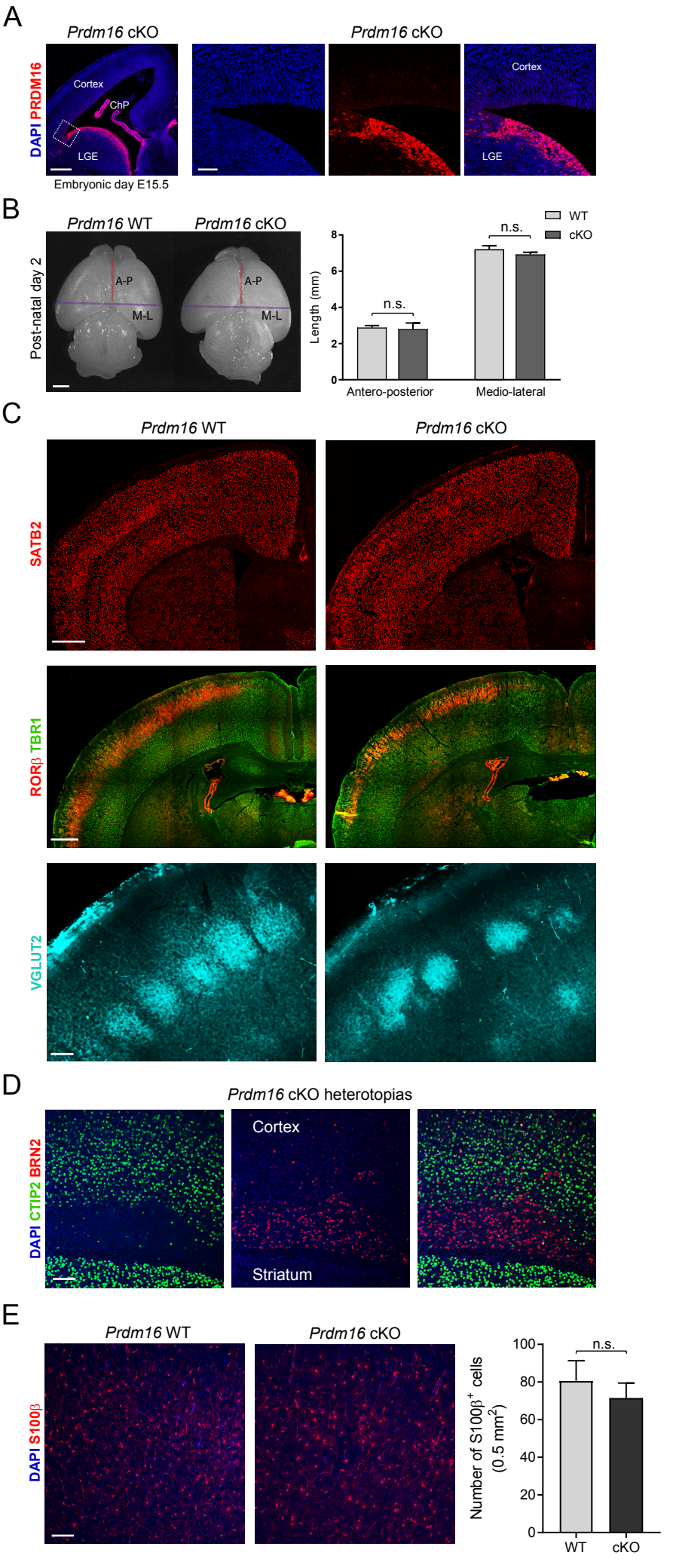
A
Prdm16 cKO
Prdm16 cKO
DAPI PRDM16
Cortex
ChP
LGE
Cortex
LGE
Embryonic day E15.5
B
Prdm16 WT
Prdm16 cKO
Post-natal day 2
A-P
M-L
A-P
M-L
WT
cKO
n.s.
n.s.
Length (mm)
8
6
4
2
0
Antero-posterior
Medio-lateral
C
Prdm16 WT
Prdm16 cKO
SATB2
RORβ TBR1
VGLUT2
D
Prdm16 cKO heterotopias
DAPI CTIP2 BRN2
Cortex
Striatum
E
Prdm16 WT
Prdm16 cKO
DAPI S100β
n.s.
Number of S100β+ cells (0.5 mm2)
100
80
60
40
20
0
WT
cKO

Figure S2. PRDM16 controls the laminar organization of the cerebral cortex. Related to Figure 2.

(A) PRDM16 Immunostaining of E15.5 cKO cortex. Inset indicates the region shown at higher magnification. Reduction of PRDM16 signal is specifically observed in the cortical ventricular zone. LGE: lateral ganglionic eminence; ChP: choroid plexus.

(B) The size of WT and *Prdm16* cKO cortex was compared by measuring the length of the antero-posterior (A-P) and medio-lateral (M-L) axes.

(C) Immunostaining for $SATB2^+$ callosal projection neurons in WT and cKO cortex at P15. Middle images show $ROR\beta^+$ layer IV neurons and $TBR1^+$ layer V-VI neurons in WT and cKO cortex at P15. Lower images show $VGLUT2^+$ barrels in layer IV of the somatosensory cortex of WT and cKO brains at P10.

(D) Most cells forming heterotopias in the cKO cortex are $BRN2^+/CTIP2^-$ upper layer-like neurons.

(E) Quantification of $S100\beta^+$ cells in WT and *Prdm16* cKO cortex at P15.

Data represent mean ± SD; statistical analysis is unpaired Student's t test (n.s., not significant). Scale bars: 250 μm (A, low magnification), 50 μm (A, high magnification), 1 mm (B), 500 μm (C, upper and middle images) and 100 μm (C, lower images and D, E).

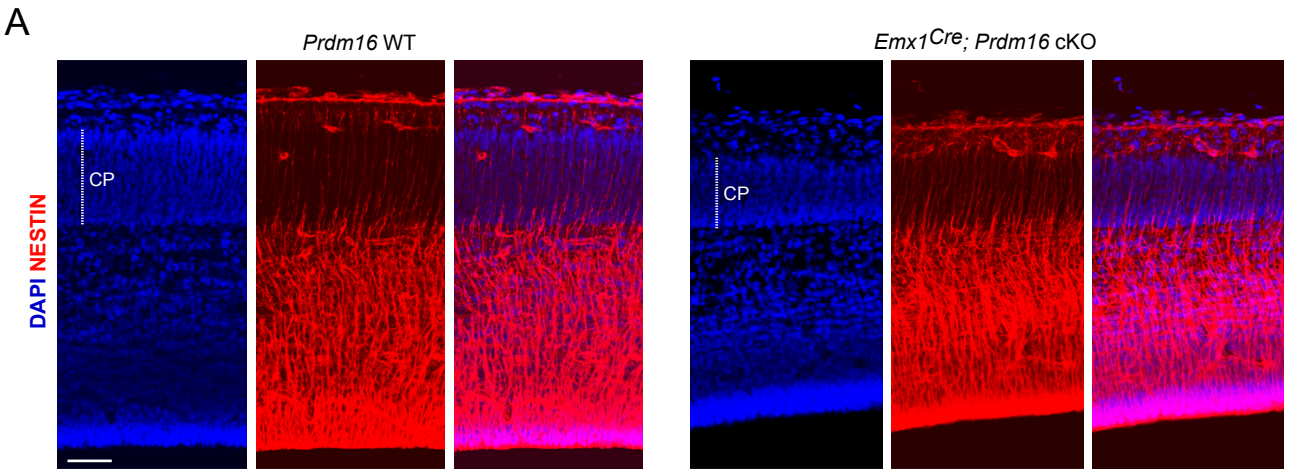
A
Prdm16 WT
Emx1Cre; Prdm16 cKO
DAPI NESTIN
CP
CP

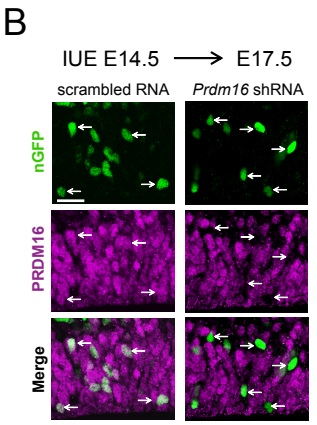
B
IUE E14.5 → E17.5
scrambled RNA
Prdm16 shRNA
nGFP
PRDM16
Merge

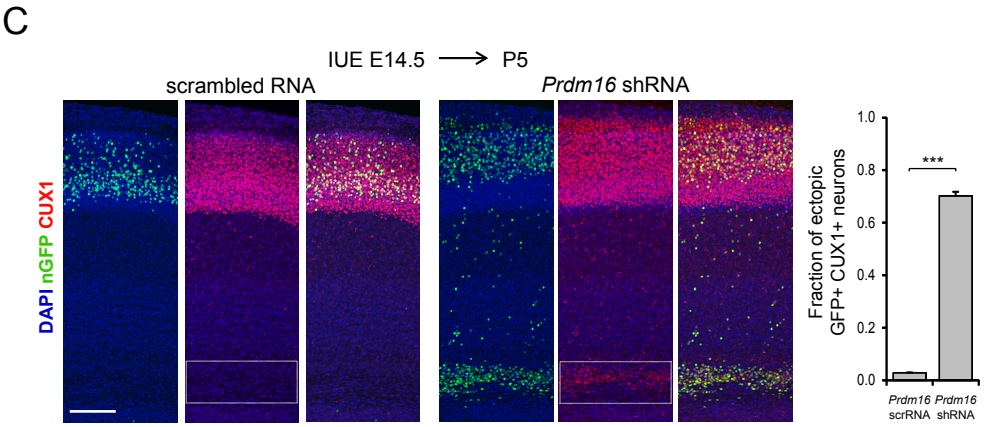
C
IUE E14.5 → P5
scrambled RNA
Prdm16 shRNA
DAPI nGFP CUX1
Fraction of ectopic GFP+ CUX1+ neurons
1.0
0.8
0.6
0.4
0.2
0.0
***
Prdm16 scrRNA
Prdm16 shRNA

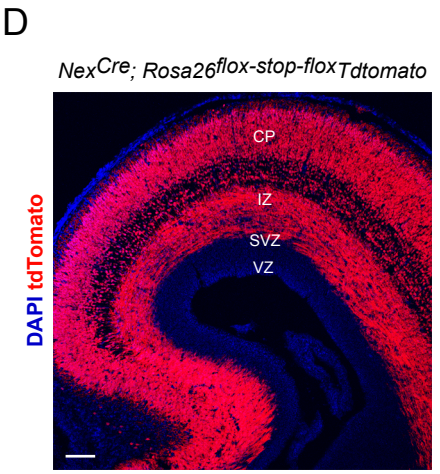
D
NexCre; Rosa26flox-stop-floxTdtomato
DAPI tdTomato
CP
IZ
SVZ
VZ

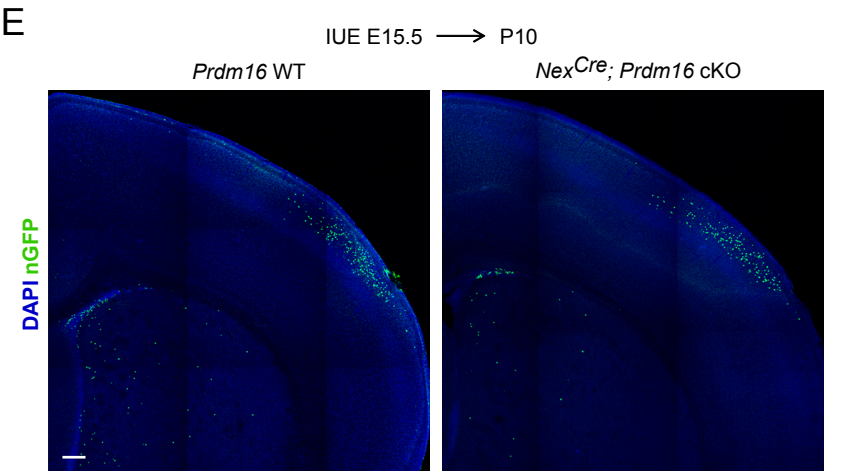
E
IUE E15.5 → P10
Prdm16 WT
NexCre; Prdm16 cKO
DAPI nGFP

Figure S3. Lineage-autonomous control of upper layer neuron position by PRDM16. Related to Figure 2.

(A) Representative images of radial glia basal processes visualized by NESTIN immunostaining of E16.5 WT and *Prdm16* cKO cortex. At this stage of development, the cortical plate (CP) in cKO brains is thinner than in WT brains (white line).

(B) *In utero* electroporation (IUE) of scrambled RNA and *Prdm16* shRNA into E14.5 WT brains. At E17.5, cells co-electroporated with *Prdm16* shRNA and nuclear *GFP* show reduced PRDM16 levels in the ventricular zone in comparison to cells electroporated with scrambled RNA (arrows).

(C) IUE of scrambled RNA and *Prdm16* shRNA into E14.5 WT brains and analysis of upper layer neuron migration at P5. A plasmid driving constitutive expression of nuclear *GFP* was co-electroporated to label the progeny of radial glia. White boxes indicate the presence of ectopic $CUX1^+$ neurons in the white matter after *Prdm16* knockdown. Quantification is shown for *Prdm16* shRNA (n=4) and scrambled RNA (n=3).

(D) Nex^{Cre} mice were crossed with a reporter mouse line carrying the $Rosa26^{flox\text{-}stop\text{-}flox\text{-}tdTomato}$ allele to confirm Cre-mediated recombination in cortical neurons in the intermediate zone (IZ) and cortical plate (CP). Recombination was not observed in the ventricular zone (VZ) and subventricular zone (SVZ).

(E) Electroporation of a plasmid encoding nuclear GFP (nGFP) into E15.5 WT and Nex^{Cre}; *Prdm16* cKO cortex and analysis of migration at P10. Representative images of WT cortex (n=3) and Nex^{Cre}; *Prdm16* cKO cortex (n=5) show normal migration of electroporated neurons into upper cortical layers.

Data represent mean ± SD; statistical analysis is unpaired Student's t test (*** $p < 0.001$). Scale bars: 50 μm (A), 20 μm (B), 100 μm (C, D), 200 μm (E).

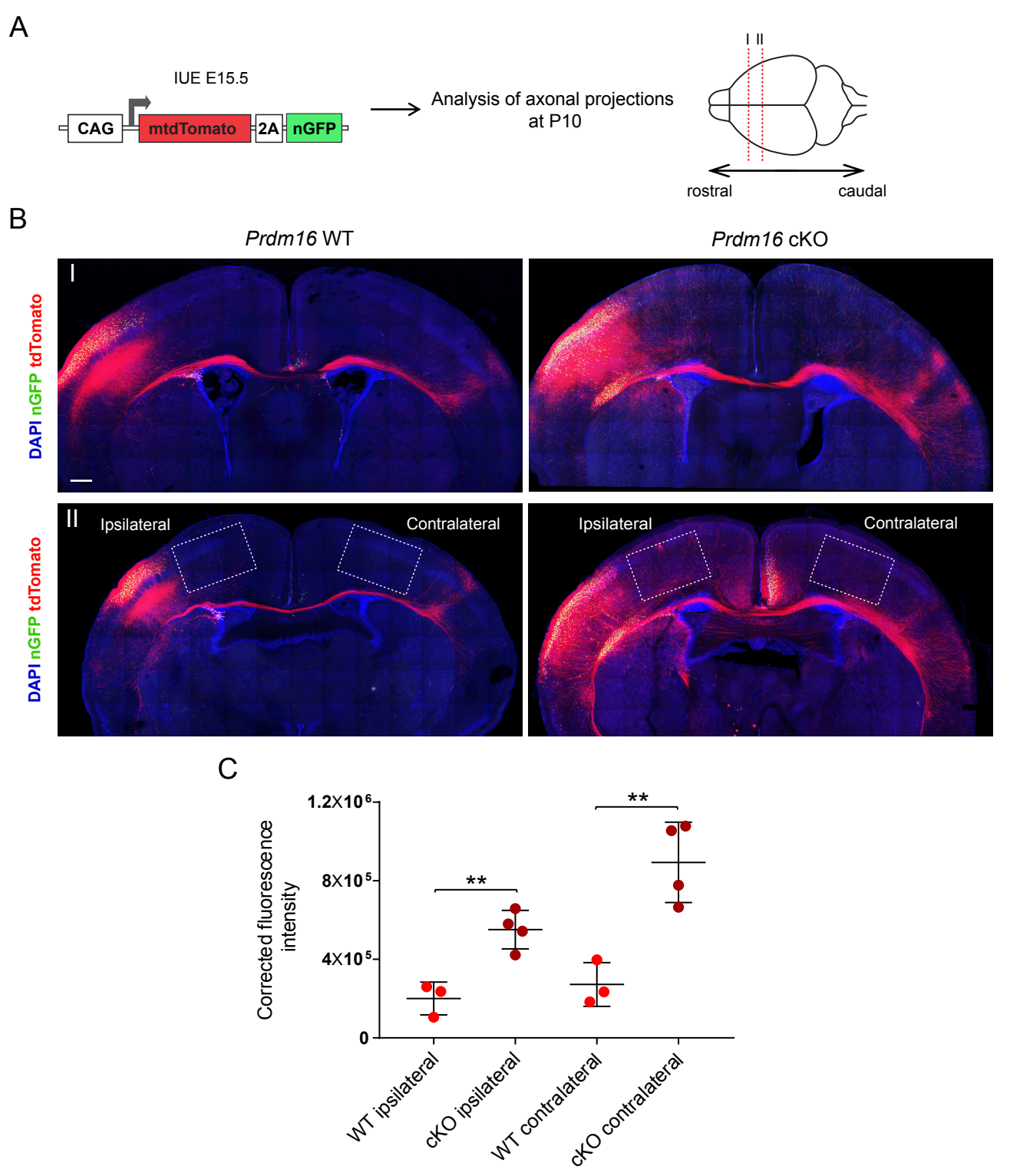

Figure S4. Abnormal axonal projections in *Prdm16* cKO cortex. Related to Figure 2.

(A) A plasmid encoding membrane tdTomato and nuclear GFP was electroporated into E15.5 WT and cKO cortex and axonal projections were analyzed at P10.

(B) Coronal sections of electroporated WT and cKO cortex at the rostro-caudal levels indicated with red lines (I and II) in panel (A).

(C) Quantification of ipsilateral and contralateral axonal projections in WT (n=3 brains) and cKO cortex (n=4) at rostro-caudal level II. The corrected fluorescent intensity of axonal projections was quantified in the areas indicated on panel (B).

Data represent mean ± SE; statistical analysis is unpaired Student's t test (**p < 0.01). Scale bar: 400 μm.

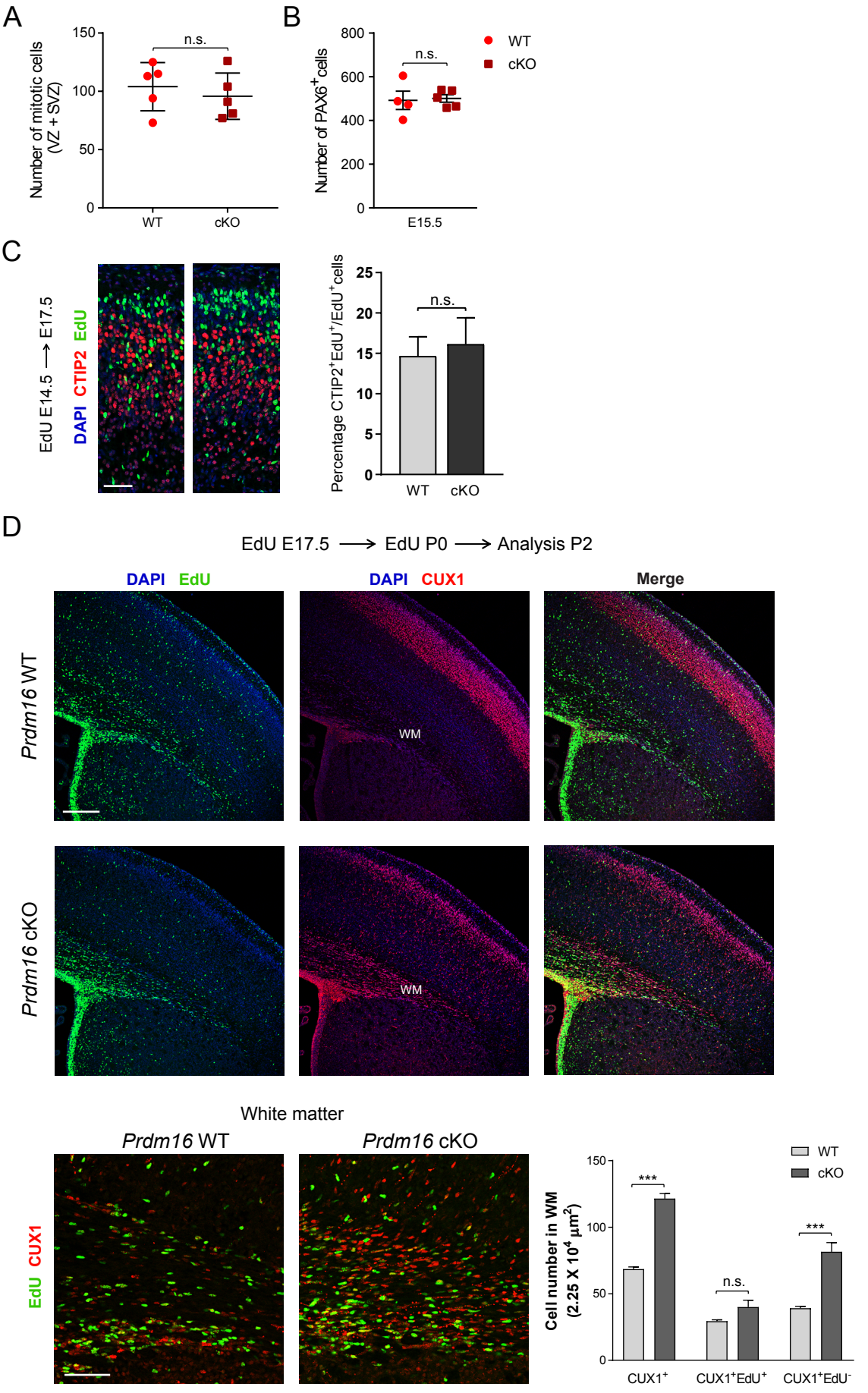
A
Number of mitotic cells (VZ + SVZ)
150
100
50
0
n.s.
WT
cKO
B
Number of PAX6+ cells
800
600
400
200
0
n.s.
WT
cKO
E15.5
C
EdU E14.5 ⟶ E17.5
DAPI CTIP2 EdU
Percentage CTIP2+EdU+/EdU+ cells
25
20
15
10
5
0
n.s.
WT
cKO
D
EdU E17.5 ⟶ EdU P0 ⟶ Analysis P2
DAPI EdU
DAPI CUX1
Merge
Prdm16 WT
Prdm16 cKO
WM
WM
White matter
Prdm16 WT
Prdm16 cKO
EdU CUX1
Cell number in WM (2.25 X 10^4 µm^2)
150
100
50
0
***
n.s.
***
WT
cKO
CUX1+
CUX1+EdU+
CUX1+EdU-

Figure S5. Analysis of radial glia number and timing of neurogenesis. Related to Figure 3.

(A) Number of $pH3^+$ mitotic cells in the ventricular zone (VZ) and subventricular zone (SVZ) of E15.5 WT and *Prdm16* cKO cortex.

(B) Number of $PAX6^+$ radial glia in E15.5 WT and *Prdm16* cKO cortex.

(C) Analysis of the timing of deep layer neurogenesis. EdU was injected at E14.5 and the percentage of $CTIP2^+/EdU^+$ cells relative to EdU^+ cells was quantified at E17.5 in WT and cKO cortex.

(D) Analysis of the timing of upper layer neurogenesis. EdU was injected at E17.5 followed by a second injection at P0 and the number of $CUX1^+$, $CUX1^+/EdU^+$ and $CUX1^+/EdU^-$ cells was quantified at P2 in the white matter (WM) of WT and cKO cortex.

Quantification of $pH3^+$, $PAX6^+$ and $CTIP2^+/EdU^+$ cells was done in 150 μm-width columns of the embryonic cortex (n=5). Data represent mean ± SE; statistical analysis is unpaired Student's t test (***$p < 0.001$; n.s., not significant). Scale bars: 50 μm (C), 250 μm (D, low magnification) and 30 μm (D, high magnification).

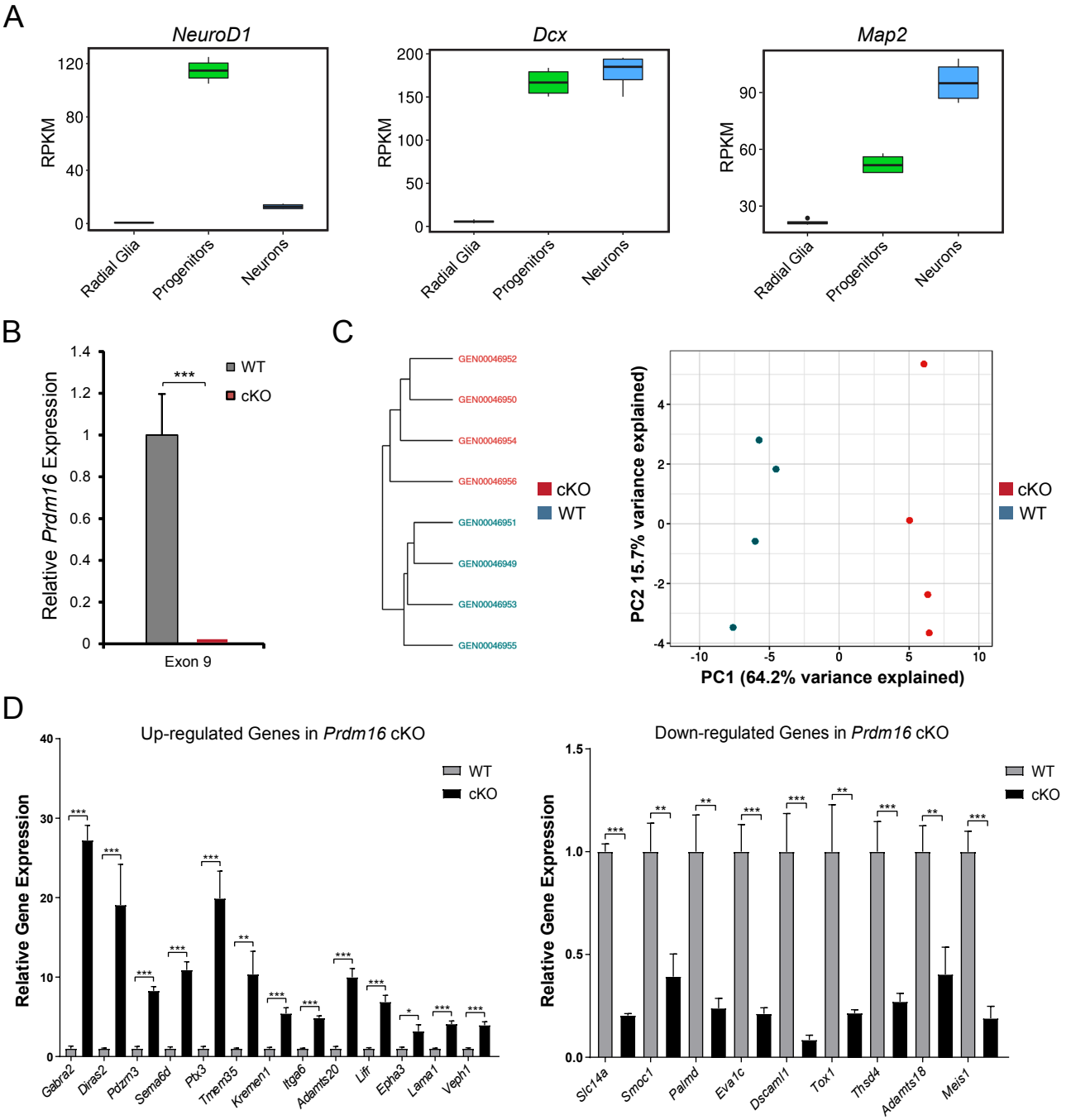

Figure S6. Transcriptional profiling of sorted cortical cells. Related to Figure 4.

(A) Expression of *NeuroD1, Dcx* and *Map2* in sorted radial glia, intermediate progenitors and neurons from E15.5 WT cortex.

(B) Relative expression of *Prdm16* (exon 9) in sorted E15.5 WT and *Prdm16* cKO radial glia.

(C) Hierarchical clustering and principal component (PC) analysis of RNA sequencing data from four biological replicates sorted from E15.5 WT and *Prdm16* cKO cortex.

(D) Real-time PCR analysis of 22 genes showing differential expression in RNA sequencing data from E15.5 WT and cKO radial glia. The relative gene expression was normalized using *Gapdh* as reference. Data represent mean ± SE; statistical analysis is unpaired Student's t test (*p < 0.05, **p < 0.01, ***p < 0.001). RPKM: Reads Per Kilobase of transcript per Million mapped reads.

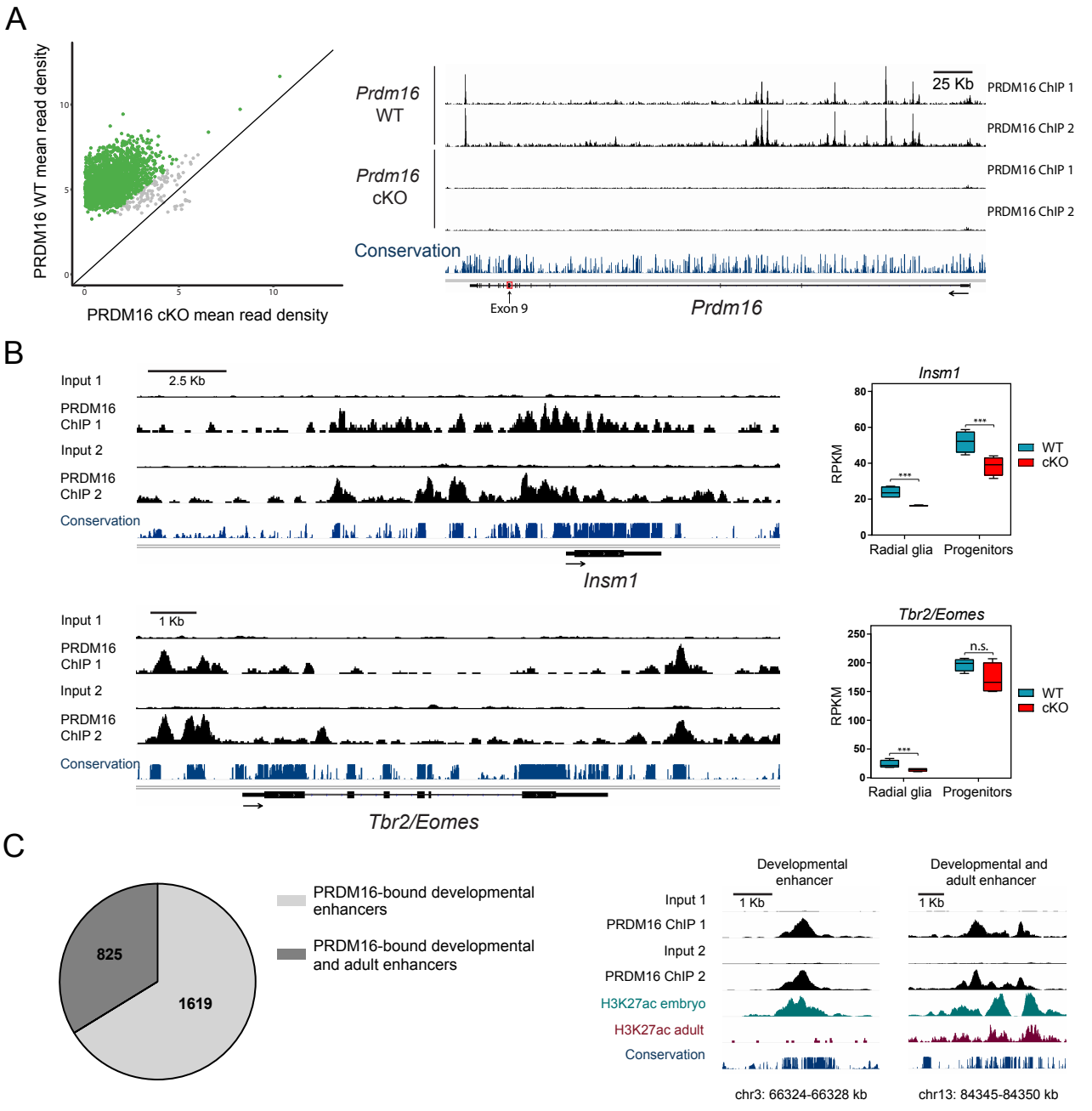

Figure S7. Identification of PRDM16 binding sites, transcriptional targets and enhancer regulation. Related to Figures 5 and 6.

(A) Comparison of the mean read density between PRDM16 ChIP-seq peaks in WT and *Prdm16* cKO cortex. The green dots represent differentially enriched binding sites (FDR < 0.05). The genome tracks show multiple PRDM16 binding sites at its own gene, whereas those peaks are absent in the cKO cortex. Exon 9 of *Prdm16*, which is mutated in cKO brains, is indicated.

(B) Genome tracks showing PRDM16 binding sites in proximity to *Insm1* and *Tbr2*/*Eomes*. The box plots indicate RNA-seq expression of *Insm1* and *Tbr2*/*Eomes* in E15.5 WT and cKO radial glia and intermediate progenitors (*** p < 0.001, n.s., not significant). RPKM: Reads Per Kilobase of transcript per Million mapped reads.

(C) Classification of PRDM16 binding sites into “developmental” or “developmental and adult” enhancers. The pie chart shows the number of each type of enhancer and the genome tracks show an example of H3K27ac enrichment within each type of enhancer.

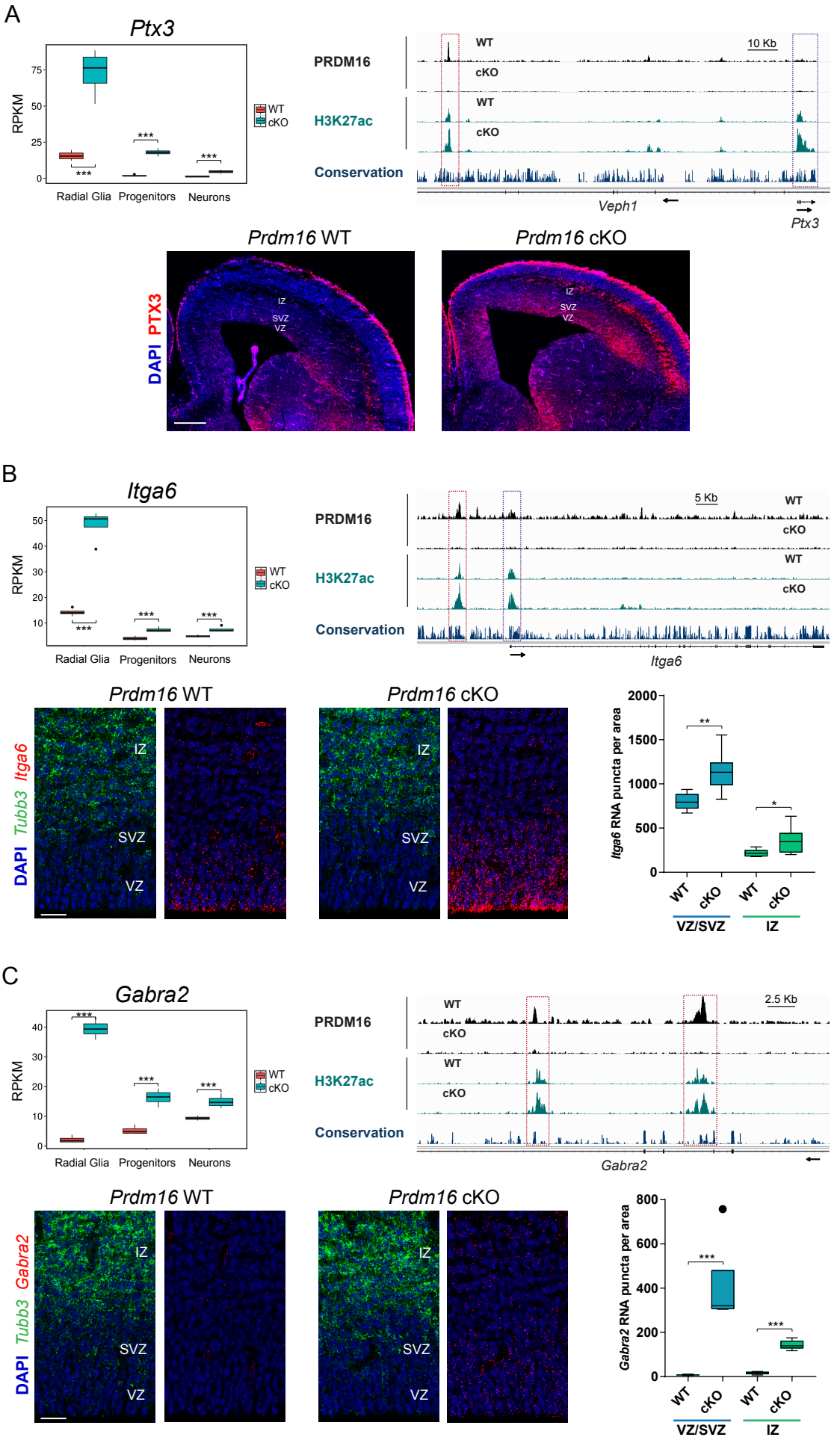
A
Ptx3
RPKM
75
50
25
0
***
***
***
Radial Glia
Progenitors
Neurons
WT
cKO
PRDM16
H3K27ac
Conservation
WT
cKO
WT
cKO
10 Kb
Veph1
Ptx3
Prdm16 WT
Prdm16 cKO
DAPI PTX3
IZ
SVZ
VZ
B
Itga6
RPKM
50
40
30
20
10
***
***
***
Radial Glia
Progenitors
Neurons
WT
cKO
PRDM16
H3K27ac
Conservation
5 Kb
WT
cKO
WT
cKO
Itga6
Prdm16 WT
Prdm16 cKO
DAPI Tubb3 Itga6
IZ
SVZ
VZ
Itga6 RNA puncta per area
2000
1500
1000
500
0
**
*
WT
cKO
WT
cKO
VZ/SVZ
IZ
C
Gabra2
RPKM
40
30
20
10
0
***
***
***
Radial Glia
Progenitors
Neurons
WT
cKO
PRDM16
H3K27ac
Conservation
WT
cKO
WT
cKO
2.5 Kb
Gabra2
Prdm16 WT
Prdm16 cKO
DAPI Tubb3 Gabra2
IZ
SVZ
VZ
Gabra2 RNA puncta per area
800
600
400
200
0
***
***
WT
cKO
WT
cKO
VZ/SVZ
IZ

Figure S8. Upregulated genes in *Prdm16* cKO cortex are associated with increased H3K27ac. Related to Figure 6.

(A) *Ptx3* expression in radial glia, intermediate progenitors and neurons was determined by RNA-seq in WT and *Prdm16* cKO cortex. Genome tracks show that *Ptx3* is the nearest gene to a PRDM16-bound enhancer showing increased H3K27ac in the cKO cortex (red box). The promoter region and gene body of *Ptx3* also show increased H3K27ac in the mutant cortex (purple box). *Prdm16* cKO cortex displays increased levels of PTX3 in the ventricular zone (VZ), subventricular zone (SVZ) and intermediate zone (IZ).

(B) *Itga6* expression in radial glia, intermediate progenitors and neurons was determined by RNA-seq in WT and *Prdm16* cKO cortex. Genome tracks indicate that *Itga6* is the nearest gene to an upstream PRDM16-bound enhancer that shows increased H3K27ac in the cKO cortex (red box). The promoter region of *Itga6* also shows increased H3K27ac in the mutant cortex (purple box). Detection of *Itga6* transcripts by fluorescent *in situ* hybridization (FISH) shows up-regulated gene expression in the VZ, SVZ and IZ of E15.5 cKO cortex.

(C) *Gabra2* expression in radial glia, intermediate progenitors and neurons was determined by RNA-seq in WT and *Prdm16* cKO cortex. Genome tracks show an intronic region of *Gabra2* that is associated with two PRDM16-bound enhancers displaying an increase of H3K27ac in the cKO cortex (red boxes). Detection of *Gabra2* transcripts by FISH indicates up-regulated gene expression in the VZ, SVZ and IZ of E15.5 cKO cortex.

Quantification of FISH results is presented as the number of puncta (mean ± SE) in 10^4 μm^2 (n=3). To identify cortical neurons in the IZ, *Tubb3* expression was detected by FISH on the same tissue sections. The statistical analysis is unpaired Student's t test (*$p < 0.05$, **$p < 0.01$, ***$p < 0.001$). Scale bars: 200 μm (A), 25 μm (B, C).

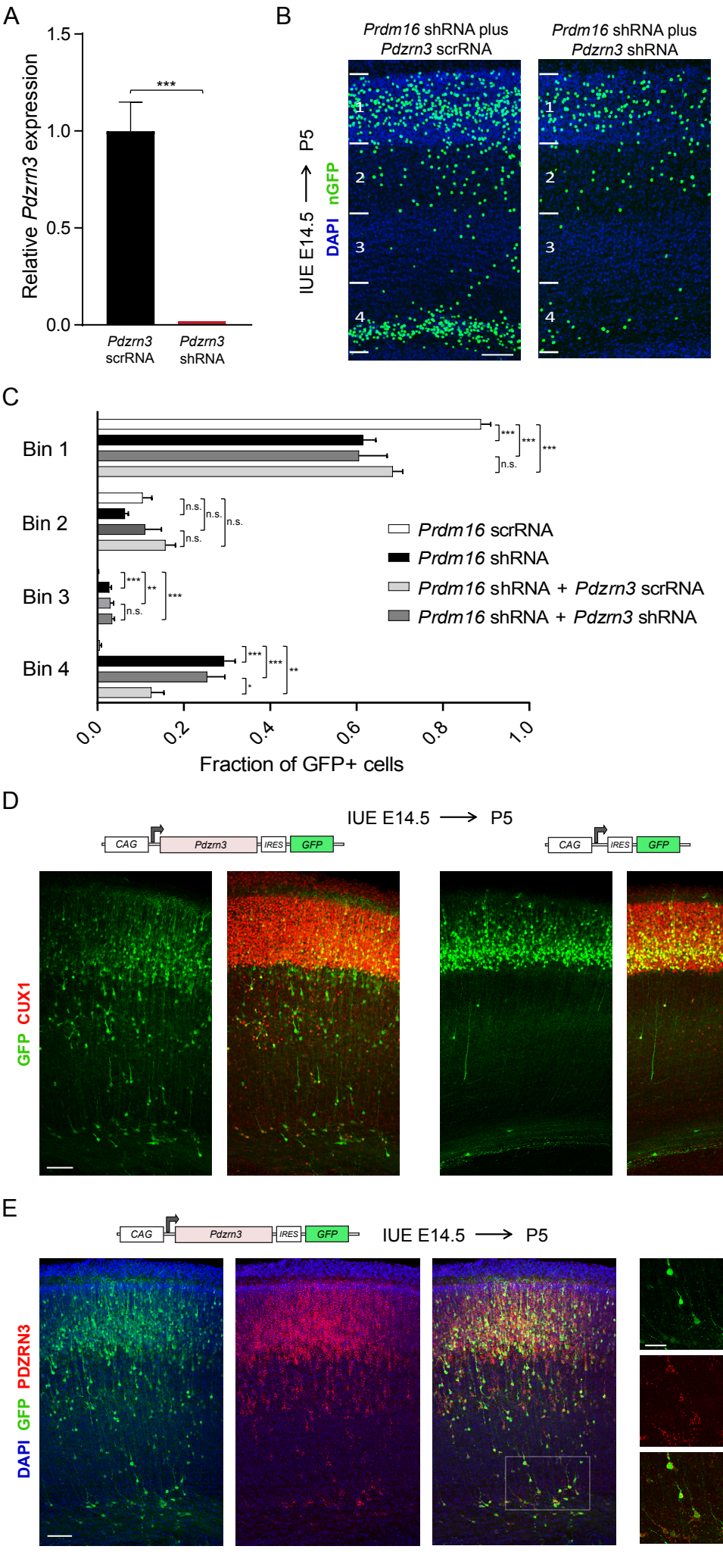
A
Relative Pdzrn3 expression
1.5
1.0
0.5
0.0
***
Pdzrn3 scrRNA
Pdzrn3 shRNA
B
Prdm16 shRNA plus Pdzrn3 scrRNA
Prdm16 shRNA plus Pdzrn3 shRNA
IUE E14.5 → P5
DAPI nGFP
1
2
3
4
C
Bin 1
Bin 2
Bin 3
Bin 4
Prdm16 scrRNA
Prdm16 shRNA
Prdm16 shRNA + Pdzrn3 scrRNA
Prdm16 shRNA + Pdzrn3 shRNA
***
**
*
n.s.
0.0
0.2
0.4
0.6
0.8
1.0
Fraction of GFP+ cells
D
IUE E14.5 → P5
CAG
Pdzrn3
IRES
GFP
GFP CUX1
E
CAG
Pdzrn3
IRES
GFP
IUE E14.5 → P5
DAPI GFP PDZRN3

Figure S9. *Pdzrn3* silencing by PRDM16 activity promotes cell migration. Related to Figure 7.

(A) *In vitro* knock-down (KD) of *Pdzrn3* expression by co-transfection of HEK293 cells with a plasmid encoding *Pdzrn3* in combination with scrambled RNA control (*Pdzrn3* scrRNA) or *Pdzrn3* short hairpin RNA (*Pdzrn3* shRNA). Two days after transfection, the relative expression of *Pdzrn3* was determined by real-time PCR analysis.

(B, C) Analysis of cell migration after single KD of *Prdm16* or double KD of *Prdm16* and *Pdzrn3*. Vectors coding for shRNA or scrRNA were co-electroporated with a vector encoding nuclear *GFP*. *In utero* electroporations were done at E14.5 and the fraction of GFP^+ cells was quantified in four bins comprising the cerebral cortex and white matter at P5 (n=3, *Prdm16* scrRNA; n=4, *Prdm16* shRNA; n=5, *Prdm16* shRNA and *Pdzrn3* scrRNA; n=7, *Prdm16* shRNA and *Pdzrn3* shRNA).

(D) A plasmid encoding *Pdzrn3* upstream *GFP* or control *GFP*-only vector were electroporated into E14.5 brains followed by analysis of neuronal migration at P5. Over-expression of *Pdzrn3* resulted in many ectopic $CUX1^+$ neurons in 4 out of 8 brains, whereas 0 out of 5 electroporated brains with the control vector resulted in ectopic cortical neurons (n=4 independent experiments).

(E) PDZRN3 immunostaining of cells electroporated with the vector encoding *Pdzrn3*. Inset images show higher magnification of $PDZRN3^+$ neurons near the white matter.

Data represent mean ± SE; statistical analysis is unpaired Student's t test (*$p < 0.05$, **$p < 0.01$, ***$p < 0.001$; n.s. not significant). Scale bars: 100 μm (B, D and E), and 50 μm (E, inset images).

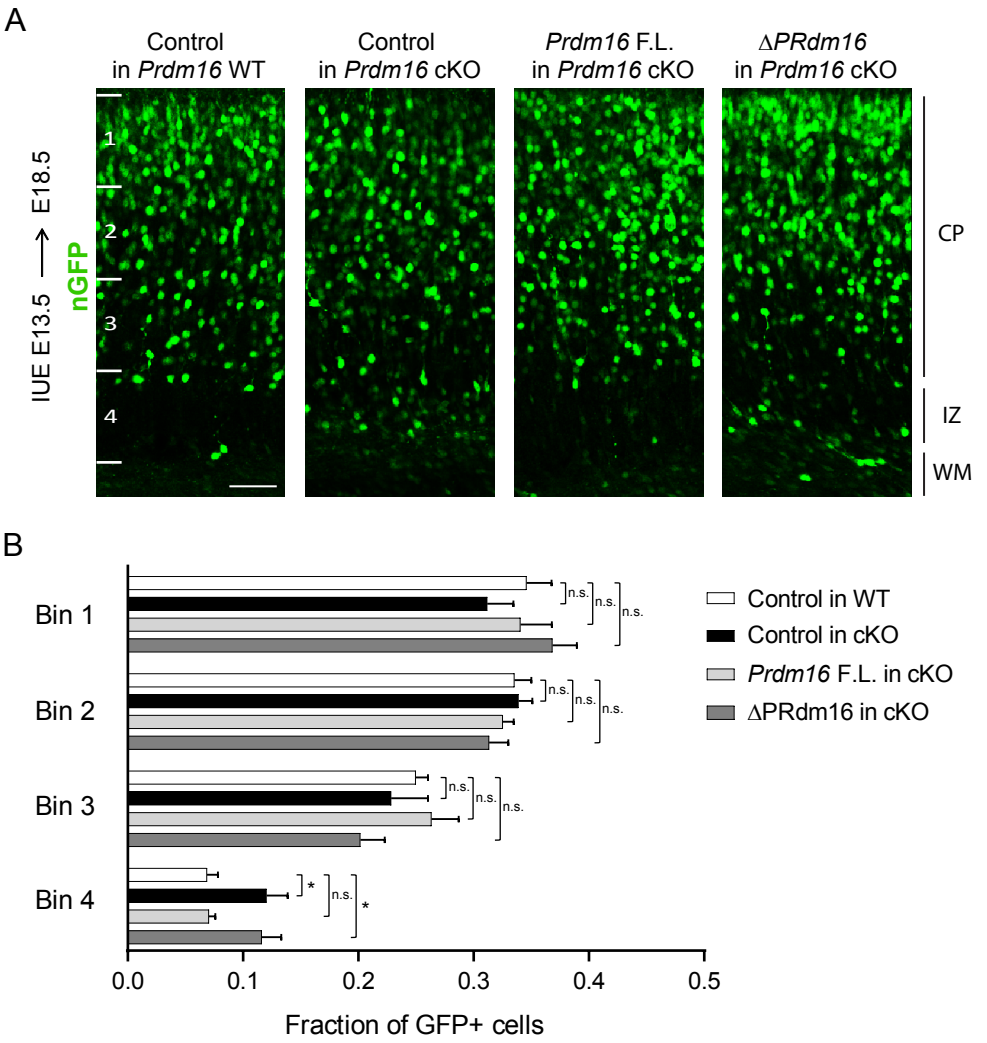

Figure S10. The histone methyl-transferase domain of PRDM16 promotes cell migration. Related to Figure 8.

(A, B) *In utero* electroporations (IUE) of control vector, *Hes5p-Prdm16* F.L and *Hes5p-ΔPRdm16* into E13.5 WT or *Prdm16* cKO cortex. Experimental vectors were co-electroporated with a plasmid encoding nuclear *GFP*. The fraction of GFP^+ nuclei was quantified in four bins comprising the cortical plate (CP), intermediate zone (IZ) and white matter (WM) in E18.5 cortex (n=6, control vector in *Prdm16* WT; n=3, control vector in *Prdm16* cKO; n=3, *Prdm16* F.L in *Prdm16* cKO; n=5, *ΔPRdm16* in *Prdm16* cKO).

Data represent mean ± SE; statistical analysis is unpaired Student's t test (*$p < 0.05$; n.s. not significant). Scale bar: 50 μm.

Top up-regulated genes in radial glia			
Gene symbol	**Gene name**	**Fold change**	**padj***
Shisa9	Shisa Family Member 9	6.488	4.82×10^{-72}
Gabra2	Gamma-Aminobutyric Acid Type A Receptor Alpha2 Subunit	4.726	1.30×10^{-24}
Diras2	DIRAS Family GTPase 2	4.662	1.39×10^{-48}
Pdzrn3	PDZ Domain Containing Ring Finger 3	4.391	1.40×10^{-59}
Sema6d	Semaphorin 6D	4.088	1.19×10^{-33}
Ptx3	Pentraxin 3	3.812	1.41×10^{-38}
Tmem35	Transmembrane Protein 35A	3.283	1.61×10^{-20}
Gm26911	Predicted gene 26911	3.250	1.14×10^{-19}
Kremen1	Kringle Containing Transmembrane Protein 1	3.216	3.51×10^{-35}
Itga6	Integrin Subunit Alpha 6	3.148	1.95×10^{-53}
Tmeff2	Transmembrane Protein With EGF-Like And Follistatin-Like Domains 2	3.135	3.24×10^{-27}
Adamts20	ADAM Metallopeptidase With Thrombospondin Type 1 Motif 20	2.939	1.96×10^{-29}
Lifr	LIF Receptor Alpha	2.821	8.01×10^{-32}
Fosl2	FOS Like 2, AP-1 Transcription Factor Subunit	2.708	1.73×10^{-17}
Fam78b	Family With Sequence Similarity 78 Member B	2.625	3.70×10^{-15}
Dab2	DAB2, Clathrin Adaptor Protein	2.611	2.69×10^{-25}
Epha3	EPH Receptor A3	2.601	1.65×10^{-15}
Cdh20	Cadherin 20	2.581	4.98×10^{-27}
Filip1	Filamin A Interacting Protein 1	2.579	1.08×10^{-14}
Tox2	TOX High Mobility Group Box Family Member 2	2.521	6.56×10^{-12}

Table S1. Related to Figure 4. RNA-seq data from 4 biological replicates. All genes included in this list have WT values > 1.5 RPKM. The full list of up-regulated genes is provided in the supplementary material. *Adjusted p-value.

Top down-regulated genes in radial glia			
Gene symbol	**Gene name**	**Fold change**	**padj***
Col12a1	Collagen Type XII Alpha 1 Chain	0.217	1.24×10^{-39}
Slc14a2	Solute Carrier Family 14 Member 2	0.239	5.37×10^{-35}
Smoc1	SPARC Related Modular Calcium Binding 1	0.270	9.76×10^{-20}
Palmd	Palmdelphin	0.296	6.13×10^{-21}
Eva1c	Eva-1 Homolog C	0.301	1.07×10^{-22}
Dscaml1	Down Syndrome Cell Adhesion Molecule Like 1	0.327	1.35×10^{-15}
Tox	Thymocyte Selection Associated High Mobility Group Box	0.330	1.64×10^{-19}
Thsd4	Thrombospondin Type 1 Domain Containing 4	0.332	2.14×10^{-28}
Mme	Membrane Metalloendopeptidase	0.334	8.13×10^{-20}
Vit	Vitrin	0.354	2.96×10^{-16}
Ankfn1	Ankyrin Repeat And Fibronectin Type III Domain Containing 1	0.359	2.00×10^{-10}
Adamts18	ADAM Metallopeptidase With Thrombospondin Type 1 Motif 18	0.368	9.76×10^{-20}
Meis1	Meis Homeobox 1	0.383	3.18×10^{-11}
AF529169	AF529169 predicted gene	0.399	2.65×10^{-08}
Htra1	HtrA Serine Peptidase 1	0.426	3.06×10^{-13}
Dapp1	Dual Adaptor Of Phosphotyrosine And 3-Phosphoinositides 1	0.430	2.00×10^{-13}
1500015O10Rik	RIKEN 1500015O10 predicted gene	0.434	2.92×10^{-07}
Jag1	Jagged 1	0.438	5.38×10^{-09}
Alk	ALK Receptor Tyrosine Kinase	0.453	6.74×10^{-08}
Tmem108	Transmembrane Protein 108	0.453	3.70×10^{-06}

Table S2 Related to Figure 4. RNA-seq data from 4 biological replicates. All genes included in this list have WT values > 1.5 RPKM. The full list of down-regulated genes is provided in the supplementary material. *Adjusted p-value.

Top up-regulated genes in intermediate progenitors			
Gene symbol	**Gene name**	**Fold change**	**padj***
Ptx3	Pentraxin 3	7.174	4.56×10^{-76}
Fosl2	FOS Like 2, AP-1 Transcription Factor Subunit	3.935	4.61×10^{-31}
Pdzrn3	PDZ Domain Containing Ring Finger 3	3.862	2.82×10^{-80}
Rcan2	Regulator Of Calcineurin 2	3.202	5.55×10^{-19}
Thrb	Thyroid Hormone Receptor Beta	3.039	2.91×10^{-32}
Gabra2	Gamma-Aminobutyric Acid Type A Receptor Alpha2 Subunit	2.751	1.99×10^{-18}
Gm26911	Predicted gene 26911	2.713	1.60×10^{-16}
Acpl2	Acid Phosphatase-Like Protein 2	2.625	4.44×10^{-24}
Slc35f1	Solute Carrier Family 35 Member F1	2.392	1.22×10^{-34}
3110035E14Rik	RIKEN 3110035E14Rik predicted gene	2.265	2.68×10^{-13}
Abcc8	ATP Binding Cassette Subfamily C Member 8	2.112	2.63×10^{-08}
Jam2	Junctional Adhesion Molecule 2	1.934	1.77×10^{-07}
Igsf11	Immunoglobulin Superfamily Member 11	1.903	6.81×10^{-06}
Lmo3	LIM Domain Only 3	1.902	4.30×10^{-04}
Gm16701	Predicted gene 16701	1.893	1.26×10^{-04}
Sez6l	Seizure Related 6 Homolog Like	1.891	1.72×10^{-09}
Fam196a	Family With Sequence Similarity 196 Member A	1.872	2.23×10^{-04}
Itga6	Integrin Subunit Alpha 6	1.867	2.52×10^{-12}
Chrna3	Cholinergic Receptor Nicotinic Alpha 3 Subunit	1.851	4.64×10^{-05}
Sypl2	Synaptophysin Like 2	1.847	5.14×10^{-08}

Table S3. Related to Figure 4. RNA-seq data from 4 biological replicates. All genes included in this list have WT values > 1.5 RPKM. The full list of up-regulated genes is provided in the supplementary material. *Adjusted p-value.

Top down-regulated genes in intermediate progenitors			
Gene symbol	**Gene name**	**Fold change**	**padj***
Smoc1	SPARC Related Modular Calcium Binding 1	0.283	4.69×10^{-16}
Dscaml1	Down Syndrome Cell Adhesion Molecule Like 1	0.305	4.46×10^{-35}
Pbx3	PBX Homeobox 3	0.307	4.97×10^{-19}
Tgfa	Transforming Growth Factor Alpha	0.390	9.66×10^{-10}
Arfgef 3	Arfgef Family Member 3	0.408	9.94×10^{-22}
Akap12	A-Kinase Anchoring Protein 12	0.433	1.19×10^{-21}
Pou3f1	POU Class 3 Homeobox 1	0.434	4.21×10^{-10}
Gm13404	Predicted gene 13404	0.477	2.50×10^{-07}
Dusp26	Dual Specificity Phosphatase 26	0.480	1.27×10^{-05}
Ube2ql1	Ubiquitin Conjugating Enzyme E2 Q Family Like 1	0.490	2.07×10^{-10}
Nrarp	NOTCH Regulated Ankyrin Repeat Protein	0.504	3.55×10^{-09}
Plch2	Phospholipase C Eta 2	0.504	1.06×10^{-12}
Lama5	Laminin Subunit Alpha 5	0.507	1.90×10^{-08}
Trim9	Tripartite Motif Containing 9	0.519	3.20×10^{-07}
Gm12968	Predicted gene 12968	0.524	3.73×10^{-04}
Kif26b	Kinesin Family Member 26B	0.534	3.00×10^{-11}
Loxl1	Lysyl Oxidase Like 1	0.535	2.30×10^{-05}
Sorl1	Sortilin Related Receptor 1	0.536	5.69×10^{-08}
C79798	Expressed sequence C79798	0.537	1.47×10^{-03}
Rasa3	RAS P21 Protein Activator 3	0.542	6.58×10^{-07}

Table S4. Related to Figure 4. RNA-seq data from 4 biological replicates. All genes included in this list have WT values > 1.5 RPKM. The full list of down-regulated genes is provided in the supplementary material. *Adjusted p-value.

REAGENT or RESOURCE	SOURCE	IDENTIFIER
Oligonucleotides		
Real-time PCR *Prdm16*, exons 9 and10. Forward: 5'-TGCTAAGCCTTCACCGTTCT-3' Reverse: 5'-TCTTTCAGGACTCCCACAGG-3' *Gabra2*, exons 5 and 6. Forward: 5'-ATGCCCACTGAAATTTGGAA-3' Reverse: 5'-AGCAACCTGAACGGAGTCAG-3' *Diras2*, single exon. Forward: 5'-CAGGAACTCCTCAACCTGGA-3' Reverse: 5'-CCCTTGAGCTTCTCCTTCCT-3' *Pdzrn3*, exons 5 and 6. Forward: 5'-GAGAAGAGCTGGAGCTGGAA-3' Reverse: 5'-TCCCAATGTCATCTTCGTCA-3' *Sema6d*, exons 13 and 14. Forward: 5'-CCTTCTCTAGCTGCGTGGTC-3' Reverse: 5'-ACCAACCACAGTACGGGTCA-3' *Ptx3*, exons 1 and 2. Forward: 5'-TGGACAACGAAATAGACAATGG-3' Reverse: 5'-TCTCCAGCATGATGAACAGC-3' *Tmem35*, exons 1 and 2. Forward: 5'-CAGCAAGGATGCCTACAGTG-3' Reverse: 5'-GATGGAATTGATGCCCATTT-3' *Kremen1*, exons 2 and 3. Forward: 5'-GCGAGCACAATTATTGCAGA-3' Reverse: 5'-GCAGGCAGGAATTTCACAGT-3' *Itga6*, exons 20 and 21. Forward: 5'-CCAAAGGTTTGGAGCAGATT-3' Reverse: 5'-TTTCAGGAAGTTCCCGTTTC-3' *Adamts20*, exons 6-9. Forward: 5'-GTCAGAATGTCCCGGATGAT-3' Reverse: 5'-AAGCCTAACGTGTCGCATTT-3' *Lifr*, exons 10-12. Forward: 5'-ACCACAGAAGCCACTCCTTC-3' Reverse: 5'-GGTAAAGGCTTCCAGTAGACGA-3'	This paper	N/A

Epha3, exons 8 and 9. Forward: 5'-TCCTCACGGTGGTCACCTAT-3' Reverse: 5'-TTAAGTGGCCATTCCCAAAG-3' *Lama1*, exons 14 and 15. Forward: 5'-TTCTGCTAAAATGGCGCTCT-3' Reverse: 5'-GGGACATTCACAGTGTTCCA-3' *Veph1*, exons 10 and 11. Forward: 5'-TTGAAGTCGCCATGACAGAG-3' Reverse: 5'-TTTCACTGAAGCCAAACACG-3' *Slc14a2*, exons 8 and 9. Forward: 5'-CTGTGCATACATGGGAGCTG-3' Reverse: 5'-GGTGAGGGTGGAGAGACAGA-3' *Smoc1*, exons 5 and 6. Forward: 5'-TTGAGCCAGGGTAATTCAGG-3' Reverse: 5'-ACACAGGTTGGGTCTCCATC-3' *Palmd*, exons 3 and 4. Forward: 5'-CAAAATCAGCAAGACCAGCA-3' Reverse: 5'-TTTGCAGTTCAGCCTTTTCA-3' *Eva1c*, exons 5-7. Forward: 5'-TACGCATGTGTTCCCAAGAA-3' Reverse: 5'-CCGCTTGGGTTGAATGTTAT-3' *Dscaml1*, exons 12 and 13. Forward: 5'-AATGGCGATGAAGTGGTCTC-3' Reverse: 5'-ATCAAACCTCGGTCCTCTCC-3' *Tox1*, exons 1-3. Forward: 5'-TGCCTGGACCCCTACTATTG-3' Reverse: 5'-CTTGGTCCAGGGTAGGACTG-3' *Thsd4*, exons 4 and 5. Forward: 5'-GGCCTATCGGCAGTACAAAC-3' Reverse: 5'-CCATGAATGGCTTGTTGTTG-3' *Adamts18*, exons 6 and 7. Forward: 5'-CAAAGATGGGACCATTGGAA-3' Reverse: 5'-TGGTCTGCATGGTGATTGAT-3' *Meis1*, exons 9 and 10. Forward: 5'-AAAAAGCAGTTGGCACAAGA-3' Reverse: 5'-GGTCTATCATGGGCTGCACT-3'	This paper	N/A
In situ hybridization, exon 4-8 probe. Forward: 5'-CTGGCTCAAGTACATCCGTGT-3' Reverse: 5'-CGTGCTGTGGATATGCTTGT-3'	(Bjork et al., 2010a)	N/A
In situ hybridization, exon 9 probe. Forward: 5'-CTGTACCCACGACCACCTCT-3' Reverse: 5'-GACTTTGGCTCAGCCTTGAC-3'	This paper	N/A
RNAscope probe Mm *Pdzrn3*	Advanced Cell Diagnostics	Cat #517061

RNAscope probe Mm *Itga6*	Advanced Cell Diagnostics	Cat #441701
RNAscope probe Mm *Gabra2*	Advanced Cell Diagnostics	Cat #435011
RNAscope probe Mm *Tubb3*	Advanced Cell Diagnostics	Cat #423391

Table S8. Related to Key Resources Table.